High Fidelity Simulations of Rotating Detonation Combustion

Large Eddy Simulation for Non-Premixed Annular Rotating Detonation Combustors

Lim, Yuxiang

2026

Document Version:
Publisher's PDF, also known as Version of record

High Fidelity Simulations of Rotating Detonation Combustion

Large Eddy Simulation for Non-Premixed Annular Rotating Detonation Combustors

YUXIANG LIM
DEPARTMENT OF ENERGY SCIENCES | FACULTY OF ENGINEERING | LUND UNIVERSITY

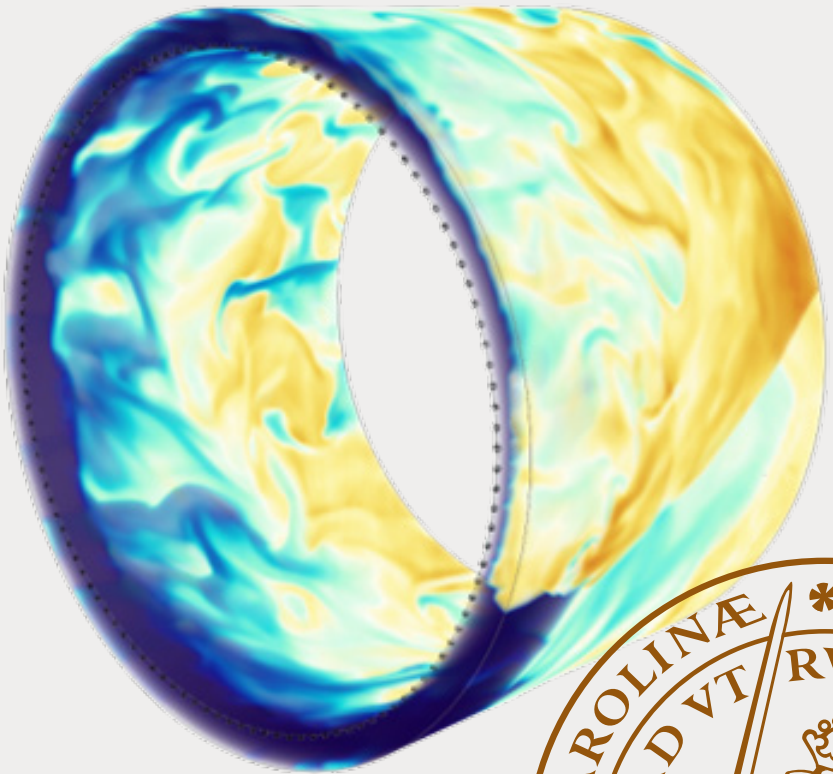

High Fidelity Simulations of Rotating Detonation Combustion

Large Eddy Simulation for Non-Premixed Annular Rotating Detonation Combustors

High Fidelity Simulations of Rotating Detonation Combustion

Large Eddy Simulation for Non-Premixed Annular Rotating Detonation Combustors

Yuxiang Lim

LUND
UNIVERSITY

DOCTORAL DISSERTATION
Thesis for the degree of Doctor of Philosophy
Thesis supervisors: Prof. Christer Fureby, Asst. Prof. Thommie Nilsson

Faculty opponent:
Prof. Myles Bohon
Technische Universität Berlin, Germany.

To be presented, with the permission of the Faculty of Engineering (LTH) of Lund University, for public criticism on Friday, the 5th of June 2026 at 10:15 AM in Room M:B, LTH, Lund University, Lund, Sweden.

Organization
LUND UNIVERSITY

Department of Energy Sciences
Box 118
SE–221 00 LUND
Sweden

Document name
DOCTORAL DISSERTATION

Date of disputation
2026-06-05

Sponsoring organization

Author(s)
Yuxiang Lim

Title and subtitle
High Fidelity Simulations of Rotating Detonation Combustion: Large Eddy Simulation for Non-Premixed Annular Rotating Detonation Combustors

Abstract

Rotating Detonation Combustors (RDCs) offer a promising alternative to conventional gas turbines by utilising continuous supersonic detonation waves for theoretical pressure-gain combustion, boosting thermal efficiencies significantly. However, developing reliable designs is exceptionally challenging because the extreme combustor environments restrict experimental sensors from capturing sub-microsecond wave mechanics fully. To bridge this gap, this thesis investigates transient flow fields within non-premixed hydrogen-air annular RDCs using a three-dimensional Implicit Large Eddy Simulation (ILES) framework in OpenFOAM. A finite-rate chemistry approach with a 22-step mechanism captures stiff chemical kinetics. Models are validated against US Air Force Research Laboratory and University of Cincinnati hardware; both utilise jets-in-crossflow schemes with roughly axial fuel injection, differing primarily in radial-outwards versus radial-inward air injections.

The ILES framework successfully replicates complex macroscopic wave topologies, including the primary detonation wavefront, oblique shocks, and slip lines. Simulations affirm that the wave acts as a highly rapid valve with the extreme pressures momentarily suppressing reactant injection, creating a highly stratified "refill zone" that continuously interacts with the propagating wave. Furthermore, a distinct thermochemical bifurcation separates high-pressure shock-induced detonation from lower-pressure deflagration. Statistical analyses confirm significant chemical energy is consumed via non-pressure-gain parasitic and commensal deflagration, undermining overall thermodynamic efficiency. While accurately predicting single-wave modes under baseline conditions, the framework over-predicts wave multiplicity (predicting an additional wave) under high-mass-flow or oxygen-enriched environments. This suggests the idealised inflow boundary conditions miss crucial acoustic dampening from the physical feed plenums. Finally, to overcome the analytical bottleneck of massive datasets, this work utilises statistical means including an automated data-driven methodology. The application of k-means clustering and directed network analysis autonomously anatomises flow fields into functional thermodynamic zones, establishing a foundation for an objective "Detonation Quality" metric.

Key words
Computational fluid dynamics; Large eddy simulation; Rotating detonation; Non-premixed; Hydrogen-air

Classification system and/or index terms (if any)

Supplementary bibliographical information

Language
English

ISSN and key title
ISSN: 0282-1990
ISRN: LUTMDN/TMHP-26/1186-SE

ISBN
978-91-8104-997-8 (print)
978-91-8104-996-1 (pdf)

Recipient's notes

Number of pages
220

Price

Security classification

Signature _____ Date 2026-04-27

High Fidelity Simulations of Rotating Detonation Combustion

Large Eddy Simulation for Non-Premixed Annular Rotating Detonation Combustors

Yuxiang Lim

LUND
UNIVERSITY

A doctoral thesis at a university in Sweden takes either the form of a single, cohesive research study (monograph) or a summary of research papers (compilation thesis), which the doctoral student has written alone or together with one or several other author(s).

In the latter case the thesis consists of two parts. An introductory text puts the research work into context and summarises the main points of the papers. Then, the research publications themselves are reproduced, together with a description of the individual contributions of the authors. The research papers may have already been published or are manuscripts at various stages (in press, submitted, or in draft).

Cover illustration: The front cover shows the front isometric view of instantaneous temperatures in a simulated rotating detonation combustor. The back cover shows the back view.

Funding information: Computer time for this research was partly provided by the Swedish National Infrastructure for Computing (SNIC) and its successor, the National Academic Infrastructure for Supercomputing in Sweden (NAISS). This support was provided through funding from the Swedish Research Council under grant agreement no. 2022-06725. Additional computational resources were provided by the Centre for Scientific and Technical Computing at Lund University (LUNARC), through reference no. LU 2025/2-40, supported by Lund University.

Division of Heat Transfer
Department of Energy Sciences
Faculty of Engineering (LTH)
Box 118
SE–221 00 LUND
Sweden

ISBN: 978-91-8104-997-8 (print)
ISBN: 978-91-8104-996-1 (pdf)
ISSN: 0282-1990
ISRN: LUTMDN/TMHP-26/1186-SE

Printed in Sweden by Media-Tryck, Lund University, Lund 2026

Yes, (almost) nobody said it was easy.
But no one ever said it would be so darn hard.
– modified lyrics.

Contents

List of publications

This thesis is based on the following publications, referred to by their Roman numerals:

I **Three-Dimensional Large-Eddy Simulation of Non-Premixed H2-Air Annular Rotating Detonation Combustor**
Y. Lim, T. Nilsson, C. Fureby
In proceedings of *AIAA SciTech 2024 Forum*, Orlando, USA, 2024. AIAA-2024-2434

II **Investigation of Detonation Wave Phenomena in Non-Premixed H2-Air Annular Rotating Detonation Combustor using Large-Eddy Simulation**
Y. Lim, T. Nilsson, C. Fureby
In proceedings of *3rd International Conference on High-Speed Vehicle Science Technology*, Busan, Korea, 2024. HiSST-2024-0174

III **Large Eddy Simulations of Rotating Detonations in Non-Premixed H2-Air Annular Combustor**
Y. Lim, T. Nilsson, C. Fureby
Combustion Science and Technology, 1-24, 2025.

IV **Investigating Detonation Wave Characteristics in Non-Premixed Hydrogen-Air Annular Rotating Detonation Combustor using Large-Eddy Simulations**
Y. Lim, T. Nilsson, C. Fureby
Manuscript prepared for *Flow, Turbulence and Combustion*

V **Large Eddy Simulations and Data Analytics of Rotating Detonation Combustion**
Y. Lim, T. Nilsson, C. Fureby
Accepted for presentation at *41st International Symposium on Combustion.*

Publications not included in this thesis:

I **Wave Phenomena Analysis of a Non-Premixed Rotating Detonation Combustor via Three-Dimensional Large Eddy Simulations**
Y. Lim, T. Nilsson, C. Fureby
In proceedings of *26th International Society for Air Breathing Engines Conference*, Toulouse, France, 2024. ISABE-2024-067

Acknowledgements

Due to constraints, I will keep this short and sweet; I look forward to sharing more during my thank-you speech.

First and foremost, I wish to express my most sincere appreciation and gratitude to my dear supervisors, Professor Christer Fureby and Assistant Professor Thommie Nilsson. What I have achieved in this doctoral research is a direct result of your expertise, dedication and patient guidance, which remained steady even through the final days of my PhD studies.

Next, I would like to thank everyone at the Department of Energy Sciences, past and present, especially those who have helped me in one way or another throughout these years. I also want to express my deepest gratitude to my closest friends in Lund and Europe for their care and company. A special mention goes to the Department itself, which provided a roof over my head for probably more hours than my actual home in Lund :P

This work would not have been possible without the support and faith of DSO National Laboratories; thanks for recognising the potential in me. I would also like to extend my gratitude to my close friends and colleagues back home, for constantly keeping in touch and offering their encouragement. Special thanks to V.N. for providing such valuable advice during this period.

Finally, but most importantly, to my loved ones back home. Words cannot express enough appreciation to my family, who have been my unwavering source of strength. Heartfelt thanks also go to my relatives, who are always so ready to welcome me back. To my partner: thank you for your patience and endless affection. And to my beloved late grandma, who left us during my studies: you will always be fondly remembered.

Popular science summary

Since the dawn of the Jet Age, humanity has relied on the gas turbine engine, which operates on a traditional, subsonic combustion principle known as "deflagration". Despite being engineering marvels, these engines are approaching a developmental plateau because they are fundamentally limited by the thermodynamics of their cycle. Consequently, squeezing out even a single percentage point of extra efficiency now requires astronomical investment. With the aviation and electricity sectors each responsible for a significant portion of global warming contributions, there is urgent pressure to drastically reduce fuel consumption. To meet global power demands sustainably, a paradigm shift is required. This thesis explores a highly promising candidate: the Rotating Detonation Combustor (RDC). Unlike conventional engines that burn fuel relatively slowly and lose pressure, an RDC utilises continuous, controlled detonations that travel faster than the speed of sound. This process compresses the fuel mixture, offering a distinct advantage known as pressure gain, which could theoretically boost engine efficiency by tens of percentage points. In a typical RDC, a detonation wave races around an annular gap between two nested cylinders at speeds exceeding 1,000 metres per second, consuming fresh reactants and leaving pressurised exhaust gas to produce thrust or spin a turbine.

While the concept is simple, the interior of an RDC is a chaotic and harsh environment where experimental sensors often fail to capture the sub-microsecond events occurring. This creates a "black box" problem where researchers struggle to understand engine instabilities and inefficiencies, preventing the design of reliable engines. To solve this, the research utilises high-fidelity Computational Fluid Dynamics, specifically Large Eddy Simulation, which acts as a "numerical microscope" powered by supercomputers. By dividing the combustor into millions of tiny cells, researchers can freeze time to see exactly what is happening inside the three-dimensional chamber. The research applied this method to replicate two real-world engines from the US Air Force Research Laboratory (AFRL) and the University of Cincinnati. Simulations of the AFRL design revealed that the detonation wave acts like a fast-acting valve, momentarily blocking fuel injection and creating a fresh air "refill zone" that dictates how the next wave will burn. The study also highlighted critical weaknesses, such as "parasitic" burning where fuel burns slowly (like a conventional flame) before the wave arrives, thereby wasting the pressure and efficiency gain potential.

A broader question emerged regarding the number of detonation waves spinning within the combustors, as predicted by the simulations. Under standard conditions, the computational results perfectly matched laboratory observations,

predicting a single, stable revolving wave for both the AFRL and Cincinnati designs. However, when the virtual engines were pushed harder, such as doubling the mass flow or enriching the air with oxygen, the models predicted an additional co-rotating wave compared to both experiments. Extensive sensitivity studies could not eliminate this extra wave, leading to the hypothesis that the simulation may be missing the dynamic 'breath' of a real engine. In reality, the combustors are connected to reactant supply reservoirs (known as plenums) that act like a dynamic buffer pool of fluid, whereas the computational model treated the reactant supplies as direct streams of inflow. Simplifying this inflow condition might have artificially stabilised the virtual combustor, allowing an extra detonation wave to survive. Further research is needed to couple these supply systems into the simulations to test this deduction. Ultimately, by validating these high-fidelity models and identifying where they succeed and struggle, this thesis aims to move the field from simple observation to predictive design, empowering engineers to confidently develop the next generation of sustainable and high-performance aero-engines.

Chapter 1

Introduction

The global push for sustainable energy and advanced propulsion has placed an unusual form of pressure on traditional combustion technologies. As of 2019, the aviation sector was responsible for approximately 2.5% of global carbon dioxide (CO_2) emissions [1]. On the other hand, the industry's total contribution to global warming is estimated to be closer to 4% [2]. This environmental imperative is coupled with an escalating demand for performance: a modern "thirst for thrust" that spans both the aviation and space sectors. However, conventional gas turbine engines operating on the subsonic and deflagration-based Brayton cycle have reached a developmental plateau. As these systems approach their theoretical efficiency limits, achieving further substantial improvements in fuel economy requires a fundamental paradigm shift. Over the last two decades, detonation-based combustion has been extensively explored as a promising alternative to overcome these limitations. Unlike conventional systems that suffer a stagnation pressure loss typically ranging from 2% to 5% in high-performance combustors [3], detonation-based combustion leverages a pressure-gain process. By utilising a supersonic detonation wave coupled to a leading shock, detonative processes approximate a constant-volume heat addition process, often modelled via the Fickett-Jacobs or Humphrey cycles. The thermodynamic advantages of the different cycle natures are significant. Whereas a standard gas turbine may achieve a thermal efficiency of approximately 35% based on the Brayton cycle, theoretical analyses of corresponding detonation-based engines suggest potential efficiencies reaching upwards of 60% to 65% under ideal conditions [4, 5]. This inherent pressure gain translates into increased exergy and higher work potential for downstream components, such as turbines or nozzles, thereby contributing to reduced emissions and increased power-to-volume ratios. This increased efficiency translates directly into operational flexibility: better fuel

economy can be leveraged to extend flight endurance, reduce carbon emissions or increase payload capacity, which are critical factors for both commercial and defence applications.

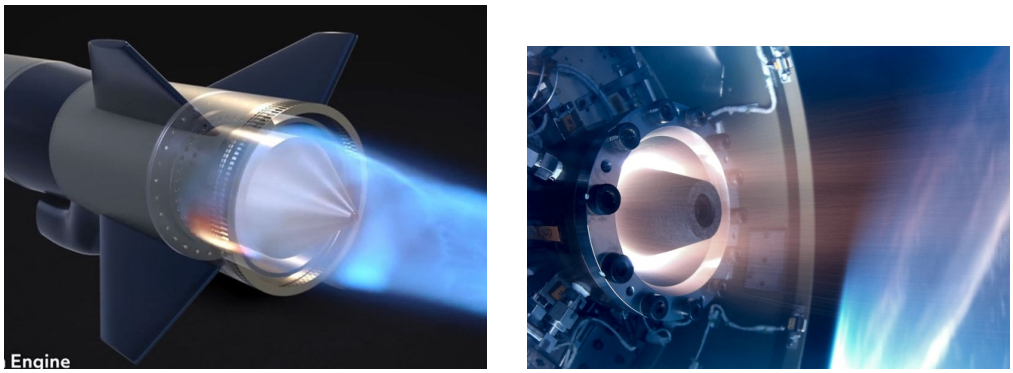

Figure 1.1: Computer-aided design drawing of RDE mounted in an aeronautical system [6] (left); first RDE successfully test-fired in space [7] (right).

A previously popular research type is the Pulse Detonation Engine (PDE) which is inherently intermittent, requires high-frequency valves and re-ignition, and as a result needing extremely precise synchronisation. On the other hand, the slightly-later-popularised Rotating Detonation Engine (RDE) operates continuously through one or more detonation waves constantly propagating around an annular or cylindrical channel, following a single ignition event. Beyond the control simplicity, the RDE stands out as a versatile and bridging technology capable of spanning the flight spectrum from subsonic to hypersonic speeds, on top of offering a more compact and mechanically simpler design compared to other detonative concepts. In a simple form of RDE, fuel and oxidiser are injected at one end of a thin annular chamber, where one or more detonation waves propagate azimuthally. This continuous flow and power generation make it a versatile candidate for a wide range of applications, including aero-propulsion ranging from jet engines to scramjets, land-based power generation, and even rocket engines for future launch and in-space transportation systems [8]. Despite the potential of RDEs to serve as a breakthrough technology for hypersonic flight and high-efficiency engine cores, the transition from proof-of-concept to practical application remains a sizeable challenge. Modern research into this phenomenon traces back over six decades to the signature experiments of Voitsekhovskii in 1959 [9]. While global interest has surged in the last 20 years, a comprehensive understanding of the complex wave physics, e.g. as mode stability, wave-injector coupling and parasitic deflagration, remains elusive. The practical relevance of RDEs depends on the ability to initiate and maintain stable detonations over

long durations, a task that necessitates high-fidelity modelling. This thesis addresses these gaps by employing Large Eddy Simulations (LES) to explore the unsteady flow fields within rotating detonation combustors (RDCs), aiming to provide the robust predictive capabilities required to bridge the gap between theoretical potential and reliable engineering design.

1.1 Motivation

Despite the clear theoretical advantages of pressure-gain combustion, the development of RDEs is currently impeded by an incomplete understanding of the sophisticated internal wave mechanisms, the absence of which obstructs the efficient design and effective control of operational RDE systems. The primary motivation for this research stems from the inherent difficulty in observing and predicting the high-speed, non-steady-state interactions within the combustion chamber. In practical non-premixed systems, the detonation wave does not propagate through a uniform medium, but rather interacts with a highly stratified mixture of fuel and oxidiser. This creates a "knowledge gap" where the coupling between reactant mixing, injector back-pressure, and wave stability remains poorly characterised.

Experimental diagnostics, while providing invaluable surface-level data, are often operating at their limits under the extreme conditions and yet unable to resolve for instance the three-dimensional, sub-microsecond structures of the detonation front or the specific contributions of detonative and deflagrative heat releases. As a result, there is an urgent need for high-fidelity computational models that can act as a "numerical microscope", providing the spatial and temporal resolution required to dissect these phenomena.

The difficulty in observing these high-speed interactions is amplified by the sheer scale range of the physics involved, spanning four orders of magnitude in spatial measurements. This factor is further complicated in non-premixed systems where the detonation wave causes localised "blockage" at the inlets, creating a highly unsteady cycle of injection and mixing. There is, therefore, a critical motivation to move beyond the highly simplified CFD models that have historically dominated the field, such as those neglecting molecular diffusion or utilising global one-step reaction mechanisms, which are inherently "blind" to the radical pool development and turbulent mixing scales that dictate wave stability.

Furthermore, as industrial applications begin to explore varying hardware designs,

the demand for a "design-agnostic" predictive tool has become critical. Most studies focus on a single combustor design, leaving it unclear whether the predictive capabilities of a given model are robust or merely tuned to a specific case. There is also a distinct lack of automated analytical tools to deconstruct the massive datasets generated by LES into functional combustion zones. Bridging these gaps is essential for moving from "observation" to "predictive design" in RDC technology.

1.2 Research Questions and Objectives

A defining challenge in current RDC research is that much of the numerical modelling applied today was originally developed for conventional deflagration-based systems. There is a significant knowledge gap regarding the direct applicability of these sub-grid models and numerical parameters to the supersonic, high-pressure environment of a rotating detonation. This thesis aims to address these uncertainties by centring its investigation on the following research questions:

1. **Fundamental Physics and Stability:** To what extent can high-fidelity LES accurately capture wave-mode transitions and co-rotating wave multiplicity in annular RDCs? Can the LES framework be reliably applied, such that the wave phenomena are consistently captured across varying geometries?

2. **Numerical Parameter Sensitivity:** To what extent do choices in chemical reaction mechanisms, turbulence-chemistry interaction (TCI) models, and heat transfer conditions influence the accuracy of the predicted detonation wave speed and pressure gain?

3. **Mixing and Efficiency:** How does the passage of a detonation wave affect reactant mixing, and how much does "parasitic" deflagration affect the RDC system? Could intermediate radicals (e.g. HO_2 and OH) shed insights on the combustion/wave characteristics?

4. **Data Deconstruction:** Can advanced data-driven methodologies provide a clearer deconstruction of RDC flow physics than conventional time-averaged analyses?

To answer these questions, the scope of this work is defined by the following primary objectives:

- **Framework Validation:** Perform a systematic sensitivity study of key modelling components in Finite-Rate Chemistry (FRC) LES to quantify their impact on flow-field predictions, validated against US Air Force Research Laboratory (AFRL) experimental data.
- **Geometric Robustness Study:** Conduct a comparative analysis of two combustor designs (Design A and Design B) across different flow conditions to evaluate the model's ability to predict wave counts and mode transitions.
- **Zone Identification:** Utilise a variety of analytical tools, from conventional combustion evaluation methods, to statistical approaches, to atypical ones like k-means clustering to anatomise complex RDC datasets into distinct functional zones, such as mixing, pre-heat, and detonation, to better quantify "detonation quality" in non-premixed systems.
- **Detonation Wave Characterisation:** Document and examine effects that influence wave propagation including fuel suppression, volumetric expansion and deflagration. This in turn could provide leads to conditions of combusted products, providing a more realistic basis for the integration of RDCs with downstream components e.g. turbines.

By fulfilling these objectives, this research contributes a high-fidelity predictive strategy to the global effort of maturing detonation-based propulsion, moving the industry closer to a new era of high-efficiency energy transformation.

1.3 Aim and Scope

The scope of this thesis is centred on the application and evaluation of an FRC-LES framework, aimed at deepening the understanding of wave physics within an RDC. While lower-fidelity models like Reynolds-Averaged Navier-Stokes (RANS) or two-dimensional (2D) simulations have historically been used to save computational costs, they often fail to capture the critical three-dimensional (3D) instabilities and turbulent mixing scales that dictate wave behaviour. By employing a high-fidelity 3D LES framework, this research seeks to provide an in-depth understanding of how detonation waves propagate, specifically in non-premixed environments, where reactant stratification and unsteady back-pressures create a far more complex environment than that assumed in premixed theories. Building upon the established foundation of LES for RDC, the sensitivities of the computational model to varying chemical mechanisms, TCI models

and heat transfer conditions, are investigated. By employing a detailed 22-step hydrogen-air reaction mechanism, the simulations aim to replicate the physical realities within the concerned combustor designs, focusing on the transition from initiation to stable wave propagation. From the resulting simulations, 3D structures such as oblique shocks, slip lines, and the "injector-wave" coupling are characterised, while attention is also paid to the radial variation of the mixture fraction and its role in fuel suppression. Beyond these macroscopic wave dynamics, this research leverages the FRC framework to track the spatial and thermodynamic evolution of intermediate radical species (e.g. HO_2 and OH). In doing so, it seeks to map the thermochemical bifurcation that fundamentally separates genuine shock-induced detonation from diffusion-limited deflagration.

A significant portion of this research is dedicated to investigating the robustness of the LES framework across different hardware configurations and operating conditions. To this end, two distinct combustor geometries (designated as Design A and Design B) are analysed under varying operating conditions. A key focus is placed on the "multiplicity" of detonation waves; across both designs, the LES model demonstrates a notable predictive capability, accurately capturing the expected wave counts for primary flow conditions, while also identifying the transition to additional co-rotating wave(s) at different flow conditions. This phenomenon of wave-mode switching could be a factor for engine stability, and this thesis seeks to evaluate the factors (such as reactant fill-height and ignition history) that relate to the different wave modes. On the other hand, CFD for RDC is in a relatively early stage and, just like any other forms of research, has its limitations and sources of uncertainties. Understanding whether an unexpected simulation result represents a physically possible alternative mode or a numerical artifact is a cornerstone of this work, aimed at establishing the level of trust necessary for LES to lead the engineering design cycle of future detonation engines.

Furthermore, the scope extends beyond traditional flow-field analysis by introducing advanced data-analytic and statistical techniques to handle the high-dimensional datasets produced by LES. Conventional Eulerian or time-averaged analyses often obscure the transient features of RDC physics. Therefore, this work incorporates statistical methodologies, including conditional averaging and k-means clustering, to deconstruct the flow field to reveal trends unobvious to visual interpretation. Intriguingly, the latter technique is part of on-going work, and has been discovered to be able to deconstruct the flow field into distinct functional zones, e.g. mixing, induction, detonation, and deflagration. Consequentially, this thesis provides a framework for evaluating the "detonation quality" of a given design. Ultimately, the objective of this work is to provide

a validated, high-fidelity modelling strategy that can support the transition of RDC technology from laboratory-scale experiments to practical, long-duration aerospace propulsion and power generation systems.

1.4 Thesis Structure Outline

This thesis is structured to follow this logical progression from methodology to physical discovery. Chapter 2 provides a summarised background of rotating detonation combustion, and identifies some knowledge gaps. Chapter 3 discusses generic concepts on CFD for reactive high-speed flows. Chapter 4 details the numerical methodology and FRC-LES framework adopted in this work. Chapter 5 describes the two experimental cases used for investigation and validation. Chapter 6 synthesises the findings from the five attached publications, focusing on the physics of mixing, wave stability, and the robustness of the computational approach. Finally, Chapter 7 offers conclusions and outlooks for future RDC development.

Chapter 2

Rotating Detonation Technical Background and Research Overview

In this section, a review of the existing literature regarding the physics and modelling of rotating detonation combustion is provided. The discussion begins with an analysis of the fundamental wave physics and the current gaps in understanding that hinder the development of predictive models. This is followed by a comparison of reactant-injection strategies, specifically contrasting premixed and non-premixed regimes. Finally, an extensive overview of the CFD landscape is presented, highlighting the historical simplifications that have characterised previous studies and identifying the specific numerical uncertainties that the current research seeks to address.

2.1 Detonative Combustion and RDC Theories

2.1.1 Deflagration vs Detonation

The fundamental principles of detonation combustion rely on the coupling of a high-pressure shock wave with a subsequent heat release zone. Unlike deflagration, which is a transport-limited process driven by molecular diffusion, detonation is a wave-dominated process where a leading shock compressively heats the reactant mixture to its auto-ignition temperature. Deflagrations are generally treated as nearly-isobaric processes. Any pressure waves generated by

gas expansion propagate at the local speed of sound, outrunning the flame front which advances via diffusion at strictly subsonic velocities. In contrast, a detonation wave consists of these two fronts coupled together, travelling typically at supersonic speeds.

Classically, this is described by Chapman-Jouguet (CJ) theory, which assumes a self-sustained shock wave followed by a no-thickness reaction zone reaching sonic speed in the shock's reference frame, giving a baseline description for ideal-scenario wave speeds (in a straight channel) and pressure ratios. The Zeldovich-von Neumann-Döring (ZND) model provides a more detailed description, characterising the wave as a set involving a leading shock, an induction zone, and a reaction zone. Upon the passage of the shock, there is a marked rise in reactant temperature, pressure, and density known as the "von Neumann spike" [10]. This is followed by the induction zone that is a region of near-constant properties where chemical decomposition and radical formation occur, and finally the reaction zone, where rapid exothermic reactions cause a surge in temperature alongside a fall in pressure and density due to volumetric expansion [11, 12].

Crucially, a detonation wave produces a significant static pressure rise across its front, enabling an overall effective total pressure gain for the thermodynamic cycle. In contrast, steady deflagration leads to a slight static pressure drop and, in practical high-performance combustors, results in a total pressure loss typically ranging from 2% to 5% [3]. This inherent pressure gain in detonation-based combustion provides higher work availability and theoretical efficiency. Analytical cycle models, such as those developed by Heiser and Pratt [3], demonstrate a fundamental thermodynamic advantage of detonation-based engines: owing to the self-compressing nature of the detonation wave, these cycles can extract useful work and achieve positive thermal efficiency even in the absence of mechanical pre-compression, whereas a standard Brayton cycle would theoretically yield 0% efficiency in the same case (no mechanical pre-compression).

Beyond these macroscopic thermodynamic advantages, the fundamental chemical-kinetic distinction between the two discussed combustion modes in hydrogen-fuelled systems is heavily dictated by the behaviour of intermediate radicals, particularly hydroperoxyl (HO_2). In standard lower-pressure deflagration flames, HO_2 is typically consumed almost instantly or exists only within thin low-temperature boundary layers, especially in the case of non-premixed combustion. Conversely, the thermodynamic state within a ZND detonation structure alters the reaction pathways. The initial high-pressure shock compression creates a state that heavily favours the third-body recombination reaction ($H + O_2 + M \rightarrow HO_2 + M$) over standard chain-branching reactions [13–15]. As

such, HO_2 acts as a critical precursor for mid-temperature auto-ignition, accumulating in non-equilibrium abundance to form a distinct measurable induction zone prior to thermal runaway and its subsequent decomposition into OH [13], which can act as a unique identification for detonative combustion. Understanding this kinetic divergence is vital, as the spatial and thermodynamic presence of HO_2 serves as a distinct chemical footprint of shock-induced combustion, particularly in H_2-detonation-based processes.

2.1.2 Rotating Detonation Fundamentals

While the macroscopic operation of an RDC is conceptually straightforward, the microscopic wave physics involve complex and highly-intertwined fluid dynamic phenomena. In a typical RDC, fuel and oxidiser are injected at the head-wall (lower edge in Figure 2.1) and ignited via a chosen initiation method. Once initiated within the annulus, one or more detonation waves travel circumferentially, continuously consuming fresh reactants via compression and combustion, while simultaneously expanding the combusted products through the chamber exit.

The rotating detonation wave is not a simple one-dimensional front but a multi-dimensional structure composed of a transverse detonation wave, an attached oblique shock, and slip lines. The distribution of the heat release within this structure is critical, influencing the main wave's strength and in turn the detonation stability.

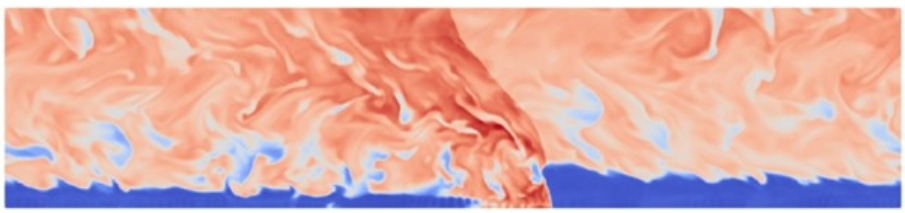

Figure 2.1: Unwrapped illustration of mid-channel slice of a simulated annular RDC, showing instantaneous temperature field. In this form of presentation, the domain could be imagined as periodic with left and right edges connected.

For the purpose of illustration, Fig. 2.1 shows the instantaneous temperature field adapted from a mid-channel cylindrical slice extracted from a simulation for one of the annular RDCs investigated in this study. The slice has been 'unwrapped', to give a '2D' view. In other words, even though this has been extracted from a 3D annular domain, the image could be imagined as periodic with left and right edges connected.

A defining feature of the RDC flow field is the wedge-shaped 'fill zone' of fresh reactants formed upstream of the wave. This geometry is a direct consequence of the expansion characteristics of the combustion products [16]. Following the detonation front, high-pressure products expand both axially toward the exhaust (upwards in Fig. 2.1) and radially (in the z-direction of Fig. 2.1, i.e. in and out of plane). Because the pressure downstream of the detonation front is significantly higher than that of the injected reactants, a pressure-gradient induced swirl is generated throughout the combustor [16]. This multi-dimensional expansion creates a substantial back-pressure that momentarily 'halts' the injectors in the immediate vicinity of the wave. As the wave moves azimuthally, the local pressure drops, allowing the injectors to recover and begin supplying fresh reactants again. This cyclic recovery process creates the characteristic triangular-shaped refill profile that the subsequent wave consumes.

Beyond the detonation front, the rapid expansion drives the hot fluids, which may further pass through additional oblique shocks formed above and attached to the primary wave. The products flow subsequently straightens and speeds toward the outlet.

Because of the exceptionally high operating frequency of these waves, the RDC produces a nearly continuous flow at the exhaust. This facilitates a more direct integration with existing turbomachinery compared to the synchronisation challenges inherent in other intermittent detonation concepts. Nevertheless, true "plug and play" operation is hindered by the severe thermo-aerodynamic environment at the combustor-turbine interface (e.g. in the context of a jet engine). Existing turbine guide vanes and blades are not designed to withstand the RDC's extreme local unsteadiness, which includes impinging oblique shocks and rapid, high-temperature thermal peaks.

2.1.3 Combustor Configurations

The physical manifestation of these waves is heavily influenced by the combustor's geometric constraints. Three common RDC geometries are briefly described below.

Annular RDCs: This most widely tested configuration consists of a constant-width channel between an inner and outer wall. The primary geometric drivers are the annulus width, overall diameter, and axial length. In these systems, increasing the channel width while maintaining a constant inner diameter can introduce significant curvature to the detonation front and trigger additional reflected shocks from the outer wall.

Hollow RDCs: Removing the inner body introduces even more pronounced three-dimensionality [17, 18] that renders standard 'unwrapped' 2D simulations insufficient. In a hollow configuration, radial curvature of the detonation front is unavoidable [19]; the outermost section of the wave typically propagates significantly faster than the inner tail due to the confinement of the concave outer wall. This geometry is gradually gaining research attention due to the belief that the inner wall's absence might reduce wave efficiency losses, as well as the need to cool one less surface during operation.

While hollow RDCs may help mitigate the velocity deficits seen in annular designs by allowing for more even radial dispersion of the mixture, they introduce new efficiency uncertainties. Because the detonation is strongest near the outer wall, an even radial fill height [20] may lead to less efficient reactant consumption compared to annular designs, where reactants are concentrated near the outer wall. However, the removal of the channel-width constraint also allows hollow RDCs to support detonation in mixtures that might otherwise fall outside the detonability limits of a narrow annulus [21, 22].

Disc (Radial) RDCs: In contrast to the axial bulk flow of annular and hollow configurations, disc RDCs typically inject reactants near the outer periphery or centre axis, forcing the flow radially between two parallel plates. The detonation wave propagates azimuthally through this radial flow field. This geometry is particularly attractive for compact power generation and direct integration with centrifugal compressors or radial turbines [23]. However, the continuous radial change in the cross-sectional area stretches the detonation front, introducing distinct wave stability challenges and velocity deficits not present in constant-area annular channels [24].

For the purpose of isolating and understanding the fundamental particulars of rotating detonation wave structures, the annular configuration remains the most effective research platform [16]. Additionally, the wealth of information and data presents the annular RDC as a stronger candidate to be used for testing and tuning the newly-developed LES framework for simulating rotating detonations.

2.1.4 Incomplete Understanding in RDC Mechanisms

While the macroscopic operation of an RDC is conceptually straightforward, the microscopic wave physics remains a "black box" of sophisticatedly-coupled phenomena. The standard elementary detonation theories, unfortunately, are typically insufficient for describing the 3D non-steady environment of a practical RDC [5]. In an RDC, this process is continuous and confined within a

circular channel, the simplest of which would be an annular one. One or more detonation waves propagates azimuthally, consuming a fresh "fill-zone" of reactants that are continuously injected from the head end. However, real-world RDC physics deviates significantly from 1D idealisations. For instance, the incomplete mixing and spatial inhomogeneity of the reactants, which is a defining feature of non-premixed injection, cannot be captured in 1D and are poorly resolved in 2D frameworks. Additionally, the transverse waves that drive multi-dimensional detonation instability are not properly represented in 1D models. Consequently, the real wave front is highly curved, and the 3D flow field is characterised by complex features such as slip-lines, contact discontinuities, and secondary shocks.

A primary area of uncertainty in RDC development lies in wave mode competition and stability, which governs the quantity, direction and regularity of the detonation fronts. It is well-documented that RDCs can exhibit multiple co-rotating waves, counter-rotating waves, or unstable "galloping" modes depending on the mass flow rate, back-pressure conditions and chamber geometry [8], as well as likely the state of reactant mixing ahead of the wave. The triggers for "mode switching", where the number of waves changes spontaneously, remain a subject of intense investigation. These transitions are driven by a highly non-linear feedback loop between the azimuthal wave speed and the axial "fill height" (or recovery time) of fresh reactants.

As noted in recent literature, the spontaneous appearance of an "extra" wave at higher mass flow rates suggests that the system is exquisitely sensitive to the recovery time of the injectors, which has been a parameter that is notoriously difficult to isolate experimentally. Because the interaction between the wave and the injection system creates a coupled dynamic, the precise thresholds for these transitions remain far from fully understood.

Furthermore, the existence of undesired deflagration represents a significant loss mechanism that undermines the theoretical efficiency of the cycle. This subsonic combustion generally manifests in two forms:

- **Parasitic Deflagration**: Occurs in the fresh reactants during and following the injection recovery period prior to the arrival of the detonation wave. This is related to the contact between fresh reactants from the new cycle and hot products from the previous.
- **Commensal Deflagration**: Occurs in the wake of the detonation wave where secondary heat release takes place at lower pressures. This is due to incomplete reactant mixing ahead of the wave, and subsequent incomplete

combustion across the detonation front.

Any portion of the reactants that burns in a subsonic, constant-pressure mode before the shock front arrives degrades the overall pressure-gain potential of the engine. Quantifying the fraction of heat release that occurs via detonation versus deflagration is a critical but largely unresolved challenge [25]. Assessing this ratio is vital for determining the true thermodynamic efficiency of the device, yet it requires a level of spatio-temporal resolution that most current experimental diagnostics cannot provide. This gap in measurement capability further underscores the necessity for high-fidelity numerical approaches.

2.2 Premixed vs. Non-Premixed Injections Schemes

Unsurprisingly, the manner in which fuel and oxidiser are introduced into the combustor has an effect on the resulting wave structure and stability. The bulk of early RDC research utilised premixed reactants, where the reactants are mixed upstream before injection into the combustion chamber, ensuring stable detonation and requiring simpler diagnostic tools. In a premixed configuration, the detonation wave encounters a uniform equivalence ratio, resulting in wave speeds that often more closely approach the ideal values (the CJ speed). However, practical implementation for operation, particularly in systems involving high-energy fuels like hydrogen, justifies a non-premixed approach to avoid the risk of premature ignition or "flashback" into the intake manifold, as well as thermal challenges. Consequently, more recent research has shifted towards non-premixed RDCs, where fuel and air are injected through separate discrete inlets.

Despite the above-mentioned practical advantage, non-premixed RDCs operate at the expense of a significant added layer of complexity of mixture stratification. As the fuel and oxidiser are injected through isolated ports, the detonation wave must propagate through a mixture that is spatially and temporally inhomogeneous. Furthermore, the high-pressure detonation wave causes localised 'blockage' at inlets, which has been a common RDC phenomenon, temporarily disrupting the inflow of reactants in the wave's vicinity. This creates a cycle of injection, mixing, and detonation that is highly sensitive to the local turbulent mixing scales, further intensifying the existing challenges due to the extremely short durations ($\sim \mu$s) available for reactant mixing presented by the high wave sweeping frequency. These are hypothesised to contribute to a "wave speed deficit", where the observed velocity is typically 15–30% lower than the theoretical

CJ speed [25, 26], underscoring that mixing is not merely a peripheral issue but a vital driver of RDC wave dynamics.

In a bid to improve mixing, many recent RDE designs inject reactants in an impinging cross-flow configuration [27–31], with fuel injected axially and oxidiser radially, or vice versa. Understanding the degree to which this mixing occurs during this short "injector recovery window" before the wave arrival is vital, as any unmixed reactants will burn as commensal deflagration, a subsonic combustion mode that contributes to heat release but does not provide the pressure-gain benefits of detonation. This process is deduced to be one of the primary determinants of the combustion efficiency and the overall pressure-gain performance of RDCs [26].

2.3 Experimental Studies and Limitations

Despite significant progress in the hardware demonstration of RDCs, experimental investigations remain constrained by the extreme environment inherent to high-frequency, supersonic combustion. The primary limitation is the disparity between sensor capabilities and the physical scales of the detonation process. High-repetition-rate pressure transducers often lack the bandwidth to fully resolve the steep von Neumann spike, leading to measured pressure peaks that are significantly lower than theoretical ZND predictions [32, 33]. Furthermore, the survival of intrusive probes is severely limited by the high thermal loads and mechanical stresses, often leading to probe degradation or flow blockage that distorts the local flow field [32]. Additionally, Capillary Tube Attenuated Pressure (CTAP) sensors that are commonly used in RDC experiments, have been known to filter and attenuate dynamic pressure changes, which can appear as a lower measured pressure relative to the actual instantaneous pressure, especially in dynamic or fast-changing environments [34].

Non-intrusive optical diagnostics, while powerful, face their own unique challenges in RDC geometries. The annular curvature and the narrow width of the combustion channel make high-speed imaging (e.g. chemiluminescence or PLIF) difficult, on top of "line-of-sight" integration errors where 3D wave structures are collapsed into 2D projections [35]. Additionally, the presence of soot in hydrocarbon-fuelled RDCs or the high-intensity light emission from the detonation front can saturate sensors or obscure the induction zone structure. These experimental gaps, specifically the inability to capture real-time 3D internal wave dynamics and reactant mixing gradients, necessitate the use of high-fidelity CFD to provide a complete 'volumetric' understanding of the combustor's phys-

ics [36, 37].

2.4 Simplifications in RDC CFD Studies

CFD has emerged as a promising tool for exploring RDCs' internal dynamics, yet the field has conventionally relied on significant simplifications to pragmatically manage the extreme computational costs. This challenge is largely driven by the massive disparity in spatial and temporal scales inherent to detonative flows (e.g. the detonation induction zone [$\sim \mu$m] and combustor geometry [$\sim$ cm]).

To accurately capture the features of a detonation wave, grid cells on the order of 10 to 100 μm are often required [38], which makes high-dimensional and fidelity numerical simulations of the entire engine core exceptionally expensive. Furthermore, the extreme difference in timescales between the resolving of the macroscopic flow field and the microsecond-level chemical reactions involved in the combustion process adds a layer of stiffness to the governing equations. These simplifications, while historically necessary for computational feasibility, often limit the ability of models to replicate the true stochastic and 3D nature of the hardware and phenomena. Understanding these common constraints, and the corresponding simplifications adopted to bypass them, is essential for optimising the contributions of high-fidelity modelling.

2.4.1 Dimensional and Physical Reductions, and Frame-of-Reference Simplification

A prevalent simplification in early literature is the use of two-dimensional (2D) "unwrapped" simulations to minimise computational costs [39]. While 2D models can effectively capture the azimuthal propagation of the wave, they entirely neglect the radial pressure and concentration gradients and centrifugal effects intrinsic to the annular geometry. Such radial variations are critical, as they influence the curvature of the detonation front and the stability of the "triple points" that characterise 3D detonation structures [40]. Furthermore, researchers have frequently utilised simplified geometries, such as ignoring the specific injector orifice details or treating the inlet as a uniform boundary, which fails to capture the local mixing micro-physics [39]. To further reduce computational costs, some studies have employed Euler equations, effectively neglecting molecular diffusion and viscosity [41]. Although these inviscid models can successfully capture the primary shock dynamics and wave speeds, they are likely

unable to resolve boundary layer effects, molecular mixing, or the turbulent shear layers that play significant roles in detonation combustion dynamics.

Another common approach to reduce computational complexity involves the use of steady-state or relative reference frame models. By transforming the governing equations into a frame of reference that rotates at the expected wave speed, researchers can theoretically treat the unsteady detonation as a steady-state problem [42]. While this allows for faster convergence and lower resource requirements, it inherently precludes the study of wave-mode transitions, "galloping" instabilities, or any transient behaviour that deviates from the assumed rotation speed. These models are essentially 'blind' to the most critical stability questions facing modern RDC design.

2.4.2 The Simplified Premixed Assumption

A significant portion of early RDC literature relies on the assumption of premixed reactant injection. This is often employed as an intentional and accepted simplification to bypass the high computational costs and multi-scale complexities of reactant mixing, allowing researchers to focus exclusively on fundamental detonation wave physics [43]. By assuming a perfectly-homogeneous mixture at the head end, studies can isolate the effects of chamber geometry or wave-number selection without the confounding variables of mixture stratification [20].

As will be highlighted in this thesis, this simplification bypasses, but does not solve, the challenging field of reactant mixing which has been one of the key bottlenecks in recent years. Reactant mixing in a non-premixed RDC is one primary driver of wave-speed deficits and mode instability. This aspect is particularly pertinent especially since there is the shifting trend towards more practical operational systems. In practical hardware, the detonation wave does not propagate through a uniform medium; it interacts with an evolving mixing layer that is frequently interrupted by the wave's own back-pressure. Resultantly, while premixed studies provide an upper bound for theoretical performance, they often fail to predict the failure limits or the high-frequency mode switching observed in non-premixed experimental rigs.

2.4.3 Chemical Kinetics and Turbulence Modelling

Due to the stiffness of the governing equations for chemical reactions, a common simplification is the use of global one-step or two-step reaction mechan-

isms. While these models can be tuned to match CJ velocities, they do not accurately resolve the induction time (as will be illustrated in Section 4.3) or the radical pool development (e.g. OH, H, and O species) necessary to predict wave extinction or re-ignition [44], on top of already inferior performance in the numerical calculation of conventional combustive processes (elaborated in Section 4.3). Additionally, tailoring to CJ speed would inevitably mean sacrificing the matching of corresponding deflagrative processes.

Similarly, the use of Unsteady RANS (URANS) is widespread for mapping operational envelopes. However, URANS models rely on ensemble-averaging assumptions that cannot adequately resolve highly transient, shock-turbulence-chemistry interactions. This is particularly problematic in RDCs, where the physics are highly sensitive to time-varying flow fields, especially during the transient phases before the wave settles into a stable mode. By introducing excessive artificial turbulent viscosity, URANS typically "smears" the detonation front and overlooks the fine-scale unsteady nature of the wave dynamics. Consequently, these models can lead to misleading conclusions regarding reactant mixing efficiency and wave stability, necessitating the use of higher-fidelity methods like LES [45].

2.5 High-Fidelity Modelling: Large Eddy Simulation and Numerical Models

LES often provides a significant increase in predictive capability compared with RANS, by resolving the large-scale turbulent structures while modelling the sub-grid scales (SGS). In the context of RDCs, LES is uniquely suited to capturing the complex interaction between the detonation wave and the turbulent mixing zone. However, even within the LES framework, there are notable unknowns. The suitability of standard SGS models, such as the Smagorinsky [46] or WALE [47] models, is still being evaluated for supersonic, shock-containing flows. Moreover, the sensitivity of the results to the numerical scheme's artificial viscosity, which is often used to maintain stability near shocks, can lead to "numerical diffusion" that artificially stabilises the wave or alters the predicted wave count [48]. The lack of systematic sensitivity studies complicates the quantification of how these modelling choices affect macroscopic observables like wave count and pressure gain.

Beyond SGS, there are many other numerical models and parameters that could be included to make the simulations more realistic and, if applied suitably, more accurate. These include TCI models, which account for how sub-grid

turbulence fluctuations affect reaction rates, and sophisticated heat transfer models, including Conjugate Heat Transfer (CHT) and radiation, as well as real-gas effects and thermal non-equilibrium. These additions are crucial because the extreme temperatures and pressures in RDCs lead to intense wall heat flux and thermal stratification, which in turn affect the reactant fill-height and wave speed predictions.

However, there is currently a significant gap in the literature, with a shortage of systematic studies with conclusive findings on the individual effects of each of these parameters for CFD simulations of RDCs. Moreover, there is little published findings on how they should be applied appropriately, both individually and collectively, in order to ensure numerical stability and physical accuracy. This is especially true for computationally expensive LES, where the interaction between higher-order physics and fine grid resolution can introduce unforeseen sensitivities [48], and whose development in terms of rotating detonation computation is in relatively early stages.

2.6 The Need for Advanced Data Analytics

Finally, the sheer volume of data produced by high-fidelity LES (often reaching terabytes per case) has created a "bottleneck" in analysis. Conventional Eulerian averaging "washes out" the transient features that are most critical to understanding RDC physics. As identified in the research objectives, there is a distinct lack of work in applying data analytics (e.g. k-means clustering or network theory) to deconstruct these flow fields. This area remains largely unexplored in the broader literature, making the development of such analytical frameworks a key contribution of this thesis to the field of RDC research.

2.7 Summary of Current Knowledge Gaps in Modelling

Despite the progress in LES, several critical gaps remain to be addressed by this work:

1. **The Predictive Uncertainty Gap:** It remains unclear how much the choice of a specific chemical mechanism or a TCI model dictates the macroscopic wave behaviour.

2. **Geometric Generalisation:** There is a lack of research evaluating whether a specific numerical setup can consistently predict behaviour across different hardware designs, such as the transitions observed between Design A and Design B (to be introduced later).

3. **The Artefact Identification Problem:** Discrepancies between simulations and experiments, such as the prediction of an "extra" wave, are often unresolved. It is currently difficult to distinguish whether such findings are physical latent modes or merely numerical artefacts resulting from the aforementioned simplifications.

4. **The Analytical Bottleneck:** High-fidelity LES generates vast amounts of data that conventional Eulerian or time-averaged analyses cannot fully exploit. There is a clear need for advanced, data-driven frameworks to deconstruct the flow field and identify the true "detonation quality" of a system [49].

Chapter 3

Theoretical Background for High-Speed Reactive Computational Fluid Mechanics

Reactive fluid dynamics in high-speed propulsion systems, such as RDCs, are fundamentally modelled using systems of non-linear partial differential equations. The selection of these governing equations is dictated by the specific physical phenomena of the problem. For RDC applications, the flow is characterised as a reacting, single-phase, multi-component mixture operating at high Mach numbers, where compressibility effects are dominant.

3.1 Generic Transport and Conservation Principles

The fundamental principle of conservation in fluid dynamics dictates how properties such as mass, momentum, energy, and species concentrations evolve over time and space. For a multi-component compressible fluid, the fully-coupled governing equations (i.e. the Navier-Stokes equations) can be compactly represented using a system of conservation laws in vector notation.

For clarity of illustration and simplicity, the flow parameters are bundled into a single conservative state vector, $\mathbf{U}$, which can be defined as:

$$\mathbf{U} = \begin{bmatrix} \rho \\ \rho\mathbf{u} \\ \rho E \\ \rho Y_i \end{bmatrix}, \tag{3.1}$$

based on the fundamental conservative variables for mass (ρ), momentum ($\rho\mathbf{u}$), sensible total energy (ρE), and species mass fractions (ρY_i). Correspondingly, the generic transport equation for the continuous fluid system takes the general form:

$$\frac{\partial \mathbf{U}}{\partial t} + \nabla \cdot \mathbf{F}_c(\mathbf{U}) = \nabla \cdot \mathbf{F}_v(\mathbf{U}) + \mathbf{S}(\mathbf{U}) \tag{3.2}$$

where the terms from left to right represent the transient rate of change, the convective flux vector ($\mathbf{F}_c$), the viscous and diffusive flux vector ($\mathbf{F}_v$), and the sum of source vector ($\mathbf{S}$) representing e.g. inter-phase reactions, body forces or chemical reactions.

While the convective fluxes ($\mathbf{F}_c$) simply describe the transport of the state variables with the bulk fluid velocity, the diffusive flux vector ($\mathbf{F}_v$) and the source vector ($\mathbf{S}$) contain the highly specific physical modelling required for RDCs. Because RDCs rely on supersonic shock waves to drive the combustion cycle, the fluid experiences massive density gradients, making kinetic energy a dominant component of the total fluid energy. Consequently, the energy component is formulated using sensible total energy (E) rather than internal energy.

3.2 Turbulence Modelling in CFD: The Resolution-Modelling Spectrum

To simulate the detonation structure in an RDC, the fluid flow equations must be coupled with a detailed description of the chemical kinetics. The selection of a CFD approach involves a fundamental trade-off between the extent of resolved flow structures and the degree of turbulence modelling. In modern reactive flow research, three common primary methodologies exist: Direct Numerical Simulation (DNS), LES and Reynolds-Averaged Navier-Stokes (RANS).

At the highest level of fidelity, DNS aims to resolve the entire range of scales. However, the computational requirement scales with at least Re^3 for even the

simplest cases, making it exorbitant for practical RDC geometries. At the opposite end, RANS modelling solves for the mean flow variables. As mentioned, while URANS allows the mean flow to evolve temporally, standard turbulence closures tend to produce massive, unphysical spikes in artificial turbulent viscosity when subjected to strong shock waves, smearing the sharp detonation front [50].

LES offers a balanced compromise. In LES, a spatial filter is applied to the governing equations to explicitly resolve the energy-containing large-scale structures, while only the smaller subgrid scales are modelled. A common rule-of-thumb for a high-quality LES mesh is that it must resolve at least 80% of the turbulent kinetic energy [51]. The capability of LES to efficiently capture inherently unsteady processes [52] provides a significant advantage over RANS for high-speed reactive mixtures.

3.3 Filtered Equations for Standard (Explicit) Large Eddy Simulation

In LES, the separation of the resolved large scales from the unresolved subgrid scales is mathematically achieved by applying a spatial low-pass filter to the continuous governing equations. This filtering operation is defined by the convolution integral of a flow variable $\phi(\mathbf{x}, t)$ with a filter kernel G:

$$\overline{\phi}(\mathbf{x}, t) = \int_D \phi(\mathbf{x}', t) G(\mathbf{x} - \mathbf{x}', \Delta) d\mathbf{x}' \tag{3.3}$$

where D is the fluid domain and Δ represents the characteristic filter width. To avoid more unclosed subgrid terms and further mathematical complexity due to the highly compressible nature of the detonation flow (highly varying density), density-weighted Favre-filtering is employed. Mathematically, Favre-filtering (density-weighting) is defined as $\tilde{\phi} = \overline{\rho\phi}/\overline{\rho}$, and a tilde is used to represent it.

Applying this operator results in the following filtered system of equations [53], for mass conservation (Equation 3.4), balances of momentum (Equation 3.5) and total energy (Equation 3.6), and species transport (Equation 3.7) respectively.

$$\frac{\partial \bar{\rho}}{\partial t} + \nabla \cdot (\bar{\rho}\tilde{\mathbf{u}}) = 0 \tag{3.4}$$

$$\frac{\partial(\bar{\rho}\tilde{\mathbf{u}})}{\partial t} + \nabla \cdot (\bar{\rho}\tilde{\mathbf{u}} \otimes \tilde{\mathbf{u}}) = -\nabla \bar{p} + \nabla \cdot (\tilde{\boldsymbol{\tau}} - \mathbf{B}) + \overline{\mathbf{S}}_u \tag{3.5}$$

$$\frac{\partial(\bar{\rho}\tilde{E})}{\partial t} + \nabla \cdot (\bar{\rho}\tilde{\mathbf{u}}\tilde{E}) = \nabla \cdot \left(-\bar{p}\tilde{\mathbf{u}} + \tilde{\boldsymbol{\tau}} \cdot \tilde{\mathbf{u}} + \tilde{\mathbf{h}} + \sum_{i=1}^{N} \left(\bar{\rho}\tilde{D}_i h_{i,f}^{\theta} \nabla \tilde{Y}_i \right) - \mathbf{b}_E \right) + \sum_{i=1}^{N} (\overline{\dot{\omega}}_i h_{i,f}^{\theta}) \tag{3.6}$$

$$\frac{\partial(\bar{\rho}\tilde{Y}_i)}{\partial t} + \nabla \cdot (\bar{\rho}\tilde{\mathbf{u}}\tilde{Y}_i) = \nabla \cdot (\bar{\rho}\tilde{D}_i \nabla \tilde{Y}_i - \mathbf{b}_i) + \overline{\dot{\omega}}_i \tag{3.7}$$

where:

- $\tilde{D}_i$ is the resolved molecular diffusivity of species i in the mixture.
- $\tilde{\boldsymbol{\tau}} \approx 2\tilde{\mu}\tilde{\mathbf{D}}_D$ is the resolved viscous stress tensor, with $\tilde{\mu}$ being the dynamic viscosity.
- $\tilde{\mathbf{D}}_D = \frac{1}{2}(\nabla\tilde{\mathbf{u}} + (\nabla\tilde{\mathbf{u}})^T) - \frac{1}{3}(\nabla \cdot \tilde{\mathbf{u}})\mathbf{I}$ is the deviatoric part of the resolved rate of strain tensor, assuming Stokes' hypothesis ($\mathbf{I}$ being the identity tensor).
- $\tilde{E} = \sum_{i=1}^{N} \left(\tilde{Y}_i \int_{T_0}^{\tilde{T}} C_{p,i} dT \right) - \bar{p}/\bar{\rho} + |\tilde{\mathbf{u}}|^2/2$ is the resolved sensible total energy, comprising sensible internal energy and kinetic energy.
- $\bar{p}\tilde{\mathbf{u}}$ is the resolved pressure work and $\tilde{\boldsymbol{\tau}} \cdot \tilde{\mathbf{u}}$ is the resolved viscous work. Unlike in low-speed combustion scenarios, these terms are essential drivers of the shock-induced heating that sustains detonation.
- $\tilde{\mathbf{h}} \approx \tilde{\kappa}\nabla\tilde{T}$ is the resolved heat flux vector (where $\tilde{\kappa}$ is the thermal diffusivity), and $\sum_{i=1}^{N}(\bar{\rho}\tilde{D}_i h_{i,f}^{\theta} \nabla \tilde{Y}_i)$ represents the energy transported by species diffusion.
- $\overline{\mathbf{S}}_u$ is a generic momentum source term (such as body forces like gravity, $\bar{\rho}\mathbf{g}$). In the specific context of high-speed reacting flows and detonations, body forces are typically orders of magnitude smaller than the extreme inertial and pressure forces, and are therefore subsequently neglected in this work.
- $\sum_{i=1}^{N}(\overline{\dot{\omega}}_i h_{i,f}^{\theta})$ represents the filtered chemical heat release.

To close the transport equations, the molecular properties $\tilde{D}_i$ and $\tilde{\kappa}$ are derived from the dynamic viscosity, $\tilde{\mu}$, via the Schmidt (Sc_i) and Prandtl (Pr) numbers, respectively. These filtered equations form a set of $N + 5$ equations, where N is the total number of species. Due to the mass conservation constraint $\sum_{i=1}^{N} \tilde{Y}_i = 1$, one species equation (typically Y_{N_2} in air-breathing systems) can be dropped [54].

3.3.1 Unclosed Subgrid Terms

The filtering process introduces unclosed terms that represent the interaction between the unresolved scales and the large-scale resolved flow. In standard explicit LES, these terms must be approximated using specific mathematical subgrid-scale (SGS) models to close the equations. In the context of high-speed reactive flows like those in an RDC, these terms carry specific physical significance:

- **Subgrid Stress Tensor (B):** This term represents the unresolved momentum transport, defined as $\mathbf{B} = \bar{\rho}(\widetilde{\mathbf{u} \otimes \mathbf{u}} - \tilde{\mathbf{u}} \otimes \tilde{\mathbf{u}})$. Physically, it accounts for the turbulent energy cascade i.e. the transfer of kinetic energy from the large, resolved turbulent eddies down to the smaller, unresolved dissipative scales.

- **Subgrid Energy Flux ($\mathbf{b}_E$):** This vector captures the unresolved transport of sensible total energy. While often simplified in low-speed combustion, it cannot be ignored in RDCs. The extreme compressibility and shock waves present in detonations mean that the filtered pressure-velocity and viscous-work correlations within this term ($\mathbf{b}_E = \bar{\rho}(\widetilde{\mathbf{u}E} - \tilde{\mathbf{u}}\tilde{E}) + (\overline{p\mathbf{u}} - \bar{p}\tilde{\mathbf{u}}) - (\overline{\boldsymbol{\tau} \cdot \mathbf{u}} - \tilde{\boldsymbol{\tau}} \cdot \tilde{\mathbf{u}})$) play a critical role in accurately predicting the shock-induced heating that sustains the detonation.

- **Subgrid Species Flux ($\mathbf{b}_i$):** Defined as $\mathbf{b}_i = \bar{\rho}(\widetilde{\mathbf{u}Y_i} - \tilde{\mathbf{u}}\tilde{Y}_i)$, this term accounts for the transport and micro-mixing of species by subgrid-scale turbulent motion. In a non-premixed RDC, capturing this accurately is vital because it dictates the reactant mixing quality ahead of the wave.

- **Filtered Chemical Source Term ($\overline{\dot{\omega}}_i$):** This term represents the filtered chemical heat release and species production. Because chemical reaction rates are highly non-linear functions of temperature and composition governed by Arrhenius kinetics, the reaction rate of an averaged temperature is distinctly not equal to the average of the true reaction rates. This poses

one of the primary modelling challenges in reactive LES, the treatment of which is elaborated upon in Section 3.8.

To mathematically close the momentum equation, standard explicit LES typically relies on the Boussinesq hypothesis [55]. This approach assumes that the momentum transfer caused by unresolved turbulent eddies behaves analogously to molecular viscous diffusion. Mathematically, the deviatoric part of the subgrid stress is modelled using a subgrid-scale dynamic viscosity, μ_{sgs}:

$$\mathbf{B} - \frac{1}{3}\mathrm{tr}(\mathbf{B})\mathbf{I} = -2\mu_{sgs}\tilde{\mathbf{D}}_D, \tag{3.8}$$

from which we could derive an expression to model, for $\mathbf{B}$. SGS models such as the classic Smagorinsky model [46], the Localised Dynamic K-equation Model [56], or the WALE model [47], are typically introduced to compute μ_{sgs} based on the resolved flow field. Analogous to the Boussinesq hypothesis, the unclosed subgrid energy and species fluxes ($\mathbf{b}_E$ and $\mathbf{b}_i$) are traditionally closed using a gradient-diffusion assumption, using subgrid turbulent Prandtl and Schmidt numbers.

While this explicit modelling framework forms the foundation of classical LES, the highly compressible, shock-dominated nature of rotating detonation combustors presents severe challenges for explicit subgrid models, which are predominantly calibrated for incompressible and non-reacting turbulence. Consequently, this thesis employs the Implicit Large Eddy Simulation (ILES) framework. As will be detailed in Section 3.6, following the introduction of the numerical discretisation scheme, ILES inherently circumvents the need to explicitly calculate these subgrid modelling terms.

3.4 Thermodynamic Closure

To mathematically close the system of transport equations, the ideal gas law is applied in its filtered form. For a compressible multi-component mixture, the filtered pressure $\bar{p}$ is related to the filtered density and temperature as:

$$\bar{p} = \bar{\rho}\widetilde{RT} \approx \bar{\rho}\tilde{R}\tilde{T} \tag{3.9}$$

In this formulation, the exact subgrid correlation between the specific gas constant and temperature ($\widetilde{RT}$) is mathematically approximated as the product of

their resolved values ($\tilde{R}\tilde{T}$). Explicitly modelling these unclosed sub-filter scalar interactions for a multi-component reactive flow is computationally prohibitive, making this assumption a standard and well-validated practice in compressible LES.

The resolved specific gas constant, $\tilde{R}$, is composition-dependent and is calculated based on the resolved species mass fractions $\tilde{Y}_i$ as:

$$\tilde{R} = R_u \sum_{i=1}^{N} \frac{\tilde{Y}_i}{W_i} \tag{3.10}$$

where R_u is the universal gas constant and W_i is the molecular weight of species i.

3.5 Numerical Methodology: The Finite Volume Method

Once the filtered system of equations and appropriate closures are established, they must be solved numerically across a defined spatial domain. This domain is discretised into a mesh consisting of a finite number of sub-volumes, or cells. To compute the flow field within this mesh, the Finite Volume Method (FVM) is employed. FVM is the predominant discretisation strategy in CFD, in both industry and academia, including for high-speed reactive flows. One of its greatest strengths is that it is inherently conservative, in other words, the numerical flux leaving a cell face is identical to the flux entering the adjacent cell. This characteristic is critical for RDC research, where the rigorous conservation of mass, momentum and energy across shocks and detonation fronts is the central governing principle [55].

In the FVM framework, the continuous partial differential equations are integrated over each control volume (V). For a general transport variable $\tilde{\phi}$, following the generic continuous transport equation, the integration over a control volume yields:

$$\int_V \frac{\partial(\bar{\rho}\tilde{\phi})}{\partial t} dV + \int_V \nabla \cdot (\bar{\rho}\tilde{\mathbf{u}}\tilde{\phi}) dV = \int_V \nabla \cdot \mathbf{J}\phi dV + \int V\overline{\dot{\omega}}_\phi dV \tag{3.11}$$

By applying Gauss's Divergence Theorem ($\int_V \nabla \cdot \mathbf{f} dV = \oint_{\partial V} \mathbf{f} \cdot d\mathbf{A} \approx \sum_f (\mathbf{f} \cdot \mathbf{A})_f$) to convert the volumetric convective and diffusive terms into surface integrals

across the cell boundaries, we obtain:

$$\int_V \frac{\partial(\bar{\rho}\tilde{\phi})}{\partial t} dV + \oint_{\partial V} (\bar{\rho}\tilde{\mathbf{u}}\tilde{\phi}) \cdot d\mathbf{A} = \oint_{\partial V} \mathbf{J}\phi \cdot d\mathbf{A} + \int V\overline{\omega}_\phi dV \tag{3.12}$$

Finally, applying the Mean Value Theorem to the transient and source terms ($\tilde{\phi}_P = \frac{1}{V}\int_V \tilde{\phi}\, dV$) and discretising the surface integrals over the individual cell faces, f, yields the discretised governing equation:

$$\frac{\partial(\bar{\rho}\tilde{\phi})_P}{\partial t} + \frac{1}{V}\sum_f (\bar{\rho}\tilde{\mathbf{u}}\tilde{\phi} \cdot \mathbf{A}) f = \frac{1}{V}\sum_f (\mathbf{J}\phi \cdot \mathbf{A}) f + \overline{\omega}_{\phi,P} \tag{3.13}$$

where:

- $\tilde{\phi}$ is the general resolved transport variable (such as velocity $\tilde{\mathbf{u}}$, species mass fraction $\tilde{Y}_i$, or sensible total energy $\tilde{E}$).
- P as a subscript denotes the volume-averaged value evaluated at the centre of the control cell.
- V is the volume of the respective control cell.
- f as a subscript signifies that the term is evaluated at the discrete cell faces.
- $\mathbf{A}$ represents the outward-pointing face area vector (whose magnitude is the area of the face and direction is the face normal).
- $\bar{\rho}$ and $\tilde{\mathbf{u}}$ are the filtered density and resolved velocity vector, respectively.
- $\mathbf{J}_\phi$ is the general diffusive flux vector evaluated at the cell interfaces. As established in Section 3.3, this term expands based on the conserved variable to encompass molecular diffusion, viscous stresses, and the implicitly modelled subgrid-scale fluxes ($\mathbf{B}$, $\mathbf{b}_i$, $\mathbf{b}_E$):
  - **For Momentum ($\tilde{\phi} = \tilde{\mathbf{u}}$): $\mathbf{J_u} = \tilde{\boldsymbol{\tau}} - \mathbf{B}$** (the resolved viscous stress tensor minus the subgrid stress tensor). Note that the pressure gradient, $-\nabla\bar{p}$, is typically kept separate or lumped into the source term depending on the specific solver architecture.
  - **For Species ($\tilde{\phi} = \tilde{Y}_i$): $\mathbf{J}_{Y_i} = \bar{\rho}\tilde{D}_i\nabla\tilde{Y}_i - \mathbf{b}_i$** (the resolved molecular species diffusion minus the subgrid species flux).

– **For Total Energy ($\tilde{\phi} = \tilde{E}$): $\mathbf{J}_E = -\bar{p}\tilde{\mathbf{u}} + \tilde{\boldsymbol{\tau}} \cdot \tilde{\mathbf{u}} + \tilde{\mathbf{h}} + \sum_{i=1}^{N} \left(\bar{\rho} \tilde{D}_i h_{i,f}^{\theta} \nabla \tilde{Y}_i \right) - \mathbf{b}_E$** (comprising pressure work, viscous work, heat conduction, species diffusion enthalpy, and the subgrid energy flux).

- $\overline{\dot{\omega}}_{\phi,P}$ represents the filtered source term (such as the chemical heat release or species production rate) integrated over the cell volume.

This integral approach transforms the transport equations into a system of linear equations with dimensions determined by the total cell count. Consequently, the variables solved are the fluxes across these interfaces rather than simple cell-centred values. This characteristic is crucial, even more so for RDC. The physics of a detonation wave are dictated by the sharp jump in conditions, which fundamentally rely on the absolute conservation of mass, momentum, and energy across the shock front. If the numerical scheme were not perfectly conservative, the simulation would inherently 'leak' energy or mass, leading to incorrect predictions of detonation wave speeds and thermodynamic pressure gains.

In the specific context of RDC simulations, the numerical scheme must be robust enough to resolve the steep gradients of detonation waves without generating unphysical oscillations. Evaluating fluxes at the cell interfaces facilitates this, by allowing the implementation of Riemann solvers (such as high-order Godunov-type schemes) or Total Variation Diminishing methods to maintain stability near discontinuities. While standard LES often utilises central differencing to maximise accuracy in smooth regions, high Mach number reactive flows typically require a hybrid approach [55]. In such cases, dissipative numerical schemes are selectively applied near shocks to stabilise the solution and effectively eliminate sub-filter scales that cannot be resolved by the mesh.

3.6 Implicit Large Eddy Simulations

An alternative to explicit LES is the Implicit Large Eddy Simulation (ILES) approach. While standard explicit LES applies FVM's volume averaging to equations that have already been mathematically pre-filtered (requiring the manual addition of explicit subgrid models), ILES skips the explicit pre-filtering step entirely.

Instead, ILES fundamentally relies on the mathematical equivalence between volume integration and spatial filtering. By once again, applying the Mean Value Theorem ($\tilde{\phi}_P = \frac{1}{V} \int_V \tilde{\phi} \, dV$; introduced in Section 3.5) to the FVM discretisation,

the cell-centred value (ϕ_P) inherently becomes a volume-averaged quantity. This discrete volume integration acts as the sole implicit spatial top-hat filter over the fluid domain.

Consequently, the explicit subgrid fluxes ($\mathbf{B}$, $\mathbf{b}_E$, $\mathbf{b}_i$) do not formally arise in the governing equations. Instead, ILES implicitly captures subgrid-scale stresses and fluxes through specific features of the leading-order truncation errors inherent in the chosen numerical scheme.

The theoretical basis of ILES relies on Modified Equation Analysis. By transforming the discretised equations that are actually solved back into partial differential equations, the difference between the original continuous equations and the computed equations reveals that the leading-order truncation error acts mathematically as a dissipative diffusion term. For a generic resolved transport variable $\tilde{\phi}$, the effective continuous equation solved by the ILES framework introduces an implicit tensor-valued subgrid-scale viscosity, $\mathbf{B}_\phi^{ILES}$:

$$\frac{\partial(\bar{\rho}\tilde{\phi})}{\partial t} + \nabla \cdot (\bar{\rho}\tilde{\mathbf{u}}\tilde{\phi}) = \nabla \cdot \left(\kappa_\phi \nabla\tilde{\phi} + \mathbf{B}_\phi^{ILES} \cdot \nabla\tilde{\phi}\right) + \overline{\dot{\omega}}_\phi \tag{3.14}$$

where κ_ϕ represents the molecular diffusivity associated with the specific transported variable.

Depending on the conserved variable being solved, this generic implicit dissipation mathematically manifests in the exact physical forms of the unclosed terms introduced in Section 3.3.1. Specifically, it yields the implicit subgrid stress tensor (B_{ij}) for the momentum equations, and the subgrid flux vector (b_E or b_i) for scalar quantities like energy and species mass fractions. Built upon the concept of modified equations, these specific implicit subgrid terms generated by the numerical scheme are expressed as:

$$B_{ij} = \bar{\rho} C_{ijkl} \tilde{D}_{kl} \tag{3.15}$$

$$b_i = \bar{\rho} C^*_{ij} \nabla_j \tilde{\phi} \tag{3.16}$$

where $\tilde{D}_{kl} = \frac{1}{2}(\nabla_i \tilde{u}_j + \nabla_j \tilde{u}_i)$ is the resolved rate of strain tensor. The implicit subgrid viscosity tensor is defined as:

$$C_{ijkl} = (\delta_{ik} C^*_{jl} + \delta_{jl} C^*_{ik}) \tag{3.17}$$

with the tensor components given by:

$$C^*_{jl} = \chi \tilde{u}_j d_l \tag{3.18}$$

In this formulation, d_l is the geometrical vector connecting neighbouring cell centres, and crucially, $\chi = \chi(\Gamma)$ is a scalar-valued function of the flux limiter, Γ, which is defined by the chosen flux reconstruction scheme.

This mathematical relationship proves that the explicit subgrid fluxes do not need to be manually modelled via Boussinesq approximations. Instead, ILES shapes the scheme's truncation errors using the flux limiter (Γ) to form a self-adapting, gradient-driven numerical dissipation that effectively mimics the turbulent energy cascade at the subgrid level.

The reliance on the flux limiter is what makes ILES particularly advantageous for high-speed reactive flows. While explicit SGS models are well-established for subsonic applications, their use in supersonic and shock-dominated regimes carries certain risks. There is a potential for explicit models to inject excessive SGS viscosity across severe discontinuities, which could unphysically smear the sharp detonation front. More importantly, there is currently a significant lack of conclusive research regarding universally-applicable explicit SGS closures for RDCs. It remains largely unknown exactly how conventional SGS models behave under extreme detonation conditions, which specific model is most appropriate, or how their empirical constants should be tuned to avoid over-dissipation without sacrificing stability.

ILES circumvents these uncertainties via the monotonicity-preserving scheme (such as the Tadmor scheme used in this work). Near severe discontinuities like a detonation wave, the flux limiter automatically adapts to introduce the necessary non-linear numerical dissipation to prevent spurious unphysical oscillations. Conversely, in smooth regions of the flow, the dissipation scales back automatically to preserve the energy-containing large turbulent eddies.

Hence, while its performance is fundamentally tied to the chosen flux reconstruction method, ILES effectively handles concurrent flow features and mesh irregularities without the need for empirical damping functions or uncertain SGS constants. This self-adapting capability makes it exceptionally suited for resolving the complex shock wave multiplicity, contact surfaces, and highly anisotropic shear layers inherent to rotating detonation combustors.

3.7 Wall Modelling in Large Eddy Simulations

To manage the lack of resolution in the boundary layers adjacent to walls [57], a separate subgrid wall model is often implemented based on Spalding's Law of the Wall [58]. This is necessary because the near-wall turbulent kinetic energy

often exists in scales too small for the bulk LES mesh to resolve. The model defines an effective viscosity, $\nu_{k|w}$, at the first grid point off the wall based on the friction velocity u_τ:

$$\nu_{k|w} \approx \frac{u_\tau^2 y_P}{v_P} \tag{3.19}$$

When integrated with the ILES framework, this wall-modelled viscosity complements the built-in subgrid viscosity tensor in the cells immediately adjacent to solid boundaries.

3.8 Combustion and Turbulence-Chemistry Interaction Modelling

While the fluid dynamic and subgrid turbulent structures are governed by the transport closures detailed above, the reactive nature of the RDC requires an auxiliary combustion model to close the chemical source terms. In high-speed reactive flows, turbulence and combustion are coupled through a two-way interaction. Turbulent eddies wrinkle the flame front, increasing surface area, while turbulent diffusion broadens the layers. Conversely, heat release causes volumetric expansion, which acts to reduce vorticity.

3.8.1 Chemical Kinetics and Source Terms

To mathematically describe the combustion process, the chemical production rate $\dot{\omega}_i$ for each species is evaluated by summing the contributions of all relevant elementary reactions. For a system governed by Arrhenius kinetics, the rate constants k_r for these individual reactions are strongly dependent on temperature and are expressed as:

$$k_r = A_r T^{n_r} \exp\left(-\frac{E_r}{RT}\right) \tag{3.20}$$

where:

- A_r is the pre-exponential frequency factor for reaction r.
- n_r is the temperature exponent.

- E_r is the activation energy for the reaction.
- R is the universal gas constant.

Evaluating these highly non-linear exponential terms using only the filtered temperature ($\tilde{T}$) and mass fractions ($\tilde{Y}_i$) leads to significant modelling challenges in LES. The extreme non-linearity of reaction rates means that the reaction rate evaluated at an averaged temperature is distinctly not equal to the average of the true reaction rates, necessitating either explicit subgrid closure or carefully justified assumptions.

3.8.2 Finite-Rate Chemistry and Turbulence-Chemistry Interactions

To capture these complex reaction dynamics within the LES, a Finite-Rate Chemistry (FRC) framework is often employed, solving the species transport equations explicitly. This approach couples the simulation directly to a chemical reaction mechanism, tracking each species separately as they react at finite rates. Here, each computational cell is effectively treated as a reactor. Because chemical time scales are often orders of magnitude shorter than convective flow time scales, an operator-splitting technique is frequently used, allowing the stiff chemical state to be integrated separately from the fluid dynamics.

However, in LES, the computational mesh is usually too coarse to resolve the internal structure of a flame front, let alone that of a detonation. For instance, a laminar deflagrative flame width might only span one to three cells, whereas the scenario for a detonation wavefront would be even less ideal. This lack of resolution can lead to artificially high flame propagation rates due to numerical diffusion. To address this, Turbulence-Chemistry Interaction (TCI) models could be introduced to close the filtered reaction rate $\overline{\dot{\omega}}_i$ (cf. Section 3.3.1). The fundamental objective of a TCI model is to approximate the effects of unresolved subgrid scales on the chemical source term. While a detailed investigation into all TCI formulations falls outside the scope of this work, it is instructive to outline the conceptual approaches of several common models to illustrate how this subgrid closure is achieved:

- **Partially Stirred Reactor (PaSR):** This model approaches closure by conceptually partitioning the computational cell into two distinct zones: a reacting fraction where species are perfectly-mixed, and a non-reacting bulk fluid fraction. The size of this reacting zone is not static, but instead is determined dynamically by a continuous competition between the

local turbulent mixing time scale and the chemical reaction time scale. This allows the model to inherently account for local extinction or intense burning based on the turbulence levels.

- **Artificially Thickened Flame Model:** This approach modifies the governing equations directly. It artificially thickens the flame front by a thickening factor, F, so that it can be resolved on the coarse LES grid. To prevent the flame from burning too quickly, the chemical source term is simultaneously divided by F to preserve the correct laminar flame speed. To compensate for the subgrid wrinkling that is lost due to this artificial thickening, a subgrid efficiency function is applied to recover the correct turbulent consumption rate.

- **Eulerian Stochastic Fields:** Rooted in probability density function methods, ESF takes a statistical approach. Instead of calculating a single averaged chemical state for a computational cell, it tracks the probability of various chemical states and temperatures co-existing simultaneously due to turbulent fluctuations. It achieves this by simulating multiple parallel, randomised "fields" within the domain, allowing the highly non-linear chemical source terms to be treated exactly without requiring explicit subgrid closure for the chemistry itself.

- **Flamelet Models:** Distinct from the aforementioned models that compute chemistry on-the-fly, flamelet approaches (such as Flamelet Generated Manifolds) assume that a turbulent flame is essentially an ensemble of thin, locally one-dimensional laminar flames. The complex chemistry is pre-calculated beforehand and stored in a look-up table based on a few tracking variables (e.g. mixture fraction and a progress variable). During the simulation, the solver simply looks up the chemical state from the table, drastically reducing computational cost at the expense of assuming the combustion strictly adheres to the pre-calculated flamelet structures.

While these models are traditionally developed and validated for conventional, subsonic deflagrative flames, their direct applicability to the highly compressible and shock-driven environment of a detonation wave remains an area of ongoing research. Consequently, selecting an appropriate closure for RDCs requires careful consideration. The specific strategies adopted in this work are detailed in Chapter 4.

Chapter 4

Research Methodology and Computational Set-Up

This chapter synthesises the computational strategies and numerical frameworks employed across the studies included in this thesis. It details how the theoretical formulations established in Chapter 3 are discretised and solved, placing a primary focus on the selection of an appropriate chemical reaction mechanism and the initialisation strategies adopted here for high-speed detonative simulations.

4.1 CFD Environment and Numerical Schemes

For this research, the governing equations were solved via the FVM within the OpenFOAM environment [59]. A density-based compressible solver was utilised to maintain stability across the shocks and detonation waves prevalent in high-speed reactive flows. As introduced in Chapter 3, this study adopts an ILES approach, relying on the leading-order truncation error of the discretisation scheme, as modulated by the flux-limiter, to act as the primary subgrid dissipation mechanism. Furthermore, the dynamic viscosity has been approximated using Sutherland's law [60]. While mass and thermal diffusions naturally vary with temperature in highly compressible reactive flows, the properties $\tilde{D}_i$ and $\tilde{\kappa}$ were derived from this viscosity using constant Sc_i and Pr in all simulations. This is a common theoretical simplification [61] used to keep computational costs practical during the calculation of diffusive fluxes for highly expensive RDC simulations.

4.1.1 Spatial and Temporal Discretisation

Following the theoretical formulation of the filtered governing equations (cf. Chapter 3), the continuous spatial and temporal derivatives must be discretised for the Finite Volume solver. The extreme thermodynamic conditions within an RDC, specifically the interaction between highly compressible shock waves and turbulent mixing, dictate the rigorous selection of these numerical schemes.

4.1.1.1 Spatial Discretisation

In the highly compressible, shock-driven environment of a detonation wave, the treatment of the convective fluxes ($\mathbf{F}_c$, cf. Equation 3.2) is critical. Traditional central differencing schemes are prone to severe, unphysical oscillations when calculating fluxes across steep discontinuities. To maintain numerical stability while accurately capturing the detonation wavefront, a high-resolution, central-upwind flux reconstruction scheme based on the Kurganov-Tadmor formulation [62, 63] is employed for the convective terms. This scheme evaluates fluxes at the cell faces based on the local maximum propagation speeds of the characteristic waves. By doing so, it applies the necessary numerical dissipation precisely at the shock front to prevent unphysical wiggles, without excessively dampening the resolved turbulent structures in the smoother flow regions.

Conversely, the diffusive fluxes ($\mathbf{F}_v$, cf. Equation 3.2) are driven by relatively smooth gradients. These terms are spatially discretised using a standard second-order linear interpolation scheme (central differencing). This ensures high spatial accuracy in resolving the dissipative scales of turbulence and molecular mixing without introducing unwarranted artificial viscosity.

4.1.1.2 Temporal Integration

To advance the spatially discretised equations in time, the transient fluid dynamic transport ($\partial\mathbf{U}/\partial t$, cf. Equation 3.2) is integrated using a first-order Euler scheme. While higher-order temporal schemes exist, the Euler formulation provides the necessary robustness and stability required to navigate the severe pressure and density gradients characteristic of RDCs, while remaining computationally efficient.

4.1.2 Chemistry Integration and TCI Modelling

To handle the extreme disparity between the fluid dynamic time scales and the highly stiff chemical reaction rates, an operator-splitting technique is utilised. Specifically, a Strang-splitting scheme [64] is employed to numerically decouple the fluid transport from the chemical kinetics over each global time step. In this fractional-step approach, the fluid transport is advanced using the aforementioned Euler scheme, while the stiff chemical source terms are isolated and integrated using a robust semi-implicit Rosenbrock ODE solver [65]. This decoupling allows the chemistry solver to take extremely small internal micro-steps to resolve the Arrhenius rates without forcing the global fluid solver to operate at that same restrictively small time step.

4.1.2.1 The Quasi-Laminar Assumption

Regarding TCI within this FRC framework, as touched on in Section 3.8.2, there is a current lack of knowledge regarding how conventional LES combustion models behave under detonation-like conditions. While the evaluation of various TCI models represents a critical component of reactive LES, a detailed investigation of their formulations and suitability for RDC simulations falls outside the scope of this thesis. Consequently, for the primary simulation campaigns in this work, via what is often termed as the "Quasi-Laminar" (QL) approach, it is assumed that the filtered source term is approximately equal to the source term evaluated using the resolved variables:

$$\overline{\dot{\omega}_i(\rho, T, Y_i)} \approx \dot{\omega}_i(\bar{\rho}, \tilde{T}, \tilde{Y}_i) \tag{4.1}$$

Nonetheless, a brief introduction to the PaSR model is provided in the following sub-section, as it has been selectively utilised in a specific phase of this research to assess the impact of TCI on the flow fields. To reiterate: while the theoretical foundations of PaSR, as well as other TCI models in general, are traditionally developed for conventional deflagrative flames, they may offer valuable insights into the behaviour of detonations; the influence of TCI on this combustion regime remains significantly under-studied in current literature.

4.1.2.2 The Partially Stirred Reactor (PaSR) Model

One approach used in this research to assess the impact of TCI is the PaSR model. The model partitions the computational cell into a reactive fine structure and a non-reacting surrounding region. This separation is mathematically

represented by a bi-modal probability density function. Under this framework, the filtered species formation rate, $\overline{\dot{\omega}}_i$, is effectively simplified to the product of the reactive volume fraction, γ^*, and the reaction rate within the fine structures, $\dot{\omega}_i^*$. This formulation assumes that the chemical activity is predominantly concentrated within the high-intensity mixing zones and is negligible in the surrounding fluid.

The reacting volume fraction, γ^*, is determined by the continuous competition between a global chemical time scale, τ_c, and a turbulent mixing time scale, τ^*, associated with the dissipative structures. It is expressed as:

$$\gamma^* \approx \frac{\tau_c}{\tau^* + \tau_c} \tag{4.2}$$

In this expression, τ_c represents a global chemical time scale related to the laminar flame speed and thickness, whereas τ^* is the mixing time scale associated with the fine structures. This mixing scale is derived from the Kolmogorov time scale and the shear time scale ($\tau_\Delta = \Delta/u'$), the latter of which characterises turbulent dissipation and small-scale mixing within the filter width. By adjusting γ^*, the PaSR model accounts for the degree to which a cell is "perfectly stirred," effectively capturing the damping of reaction rates when subgrid turbulent mixing is slower than chemical kinetics.

4.2 Summary of Numerical Schemes and Models

The following table summarises the specific numerical configurations and subgrid models selected for this RDC investigation.

Table 4.1: Summary of numerical methods and model selection.

Component	Model / Scheme Selection	Justification
Discretisation Method	Finite Volume Method	Inherently conservative; essential for mass/momentum/energy balance across shocks
LES Approach	Implicit LES	Subgrid stresses/fluxes modelled by the leading-order truncation error of the scheme
Convective Fluxes	Tadmor Scheme with limiter	High-resolution central-upwind scheme capable of resolving discontinuities without oscillations
Diffusive Fluxes	Second-order Linear Interpolation	Standard approach for maintaining overall second-order accuracy
Chemistry Integration	Strang Splitting (stiff solver)	Decouples chemistry and transport to manage disparity in time scales
Wall Modelling	Spalding's Law of the Wall	Manages lack of resolution in the boundary layer by specifying effective viscosity at the wall.
TCI Model	$\overline{\dot{\omega}}_i \approx \dot{\omega}_i$ (Quasi-Laminar) / PaSR (selective runs)	Used for sensitivity testing; otherwise omitted due to lack of detonation-specific formulations

4.3 Chemical Kinetics Framework

To determine the most suitable chemical kinetics model, a comprehensive evaluation of eight different mechanisms was performed, ranging from global, skeletal models to highly detailed elementary reaction sets. These included the single-step M1 mechanism, seven-step skeletal models ES7, BG7 and D7, and more complex mechanisms J20, Z22, K30 and USCII, with the last group consisting of twenty or more reaction steps. The Z22 mechanism is of particular interest because it has been specifically tailored for low-temperature H_2-air ignition and

incorporates a specialised H_2-O_2 pathway structure.

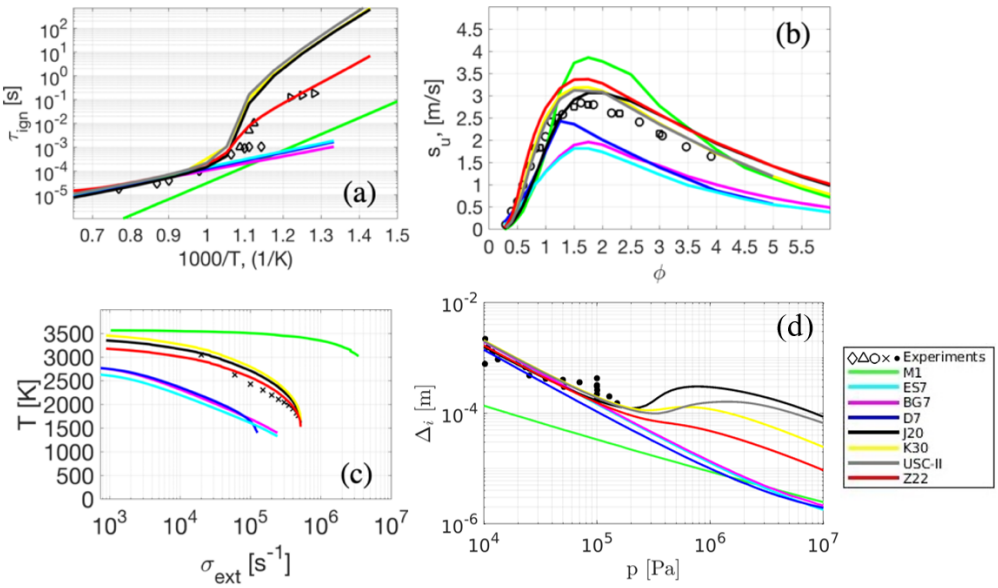

Figure 4.1: Graphs of (a) τ_{ign} vs $1000/T$; (b) s_u vs ϕ; (c) T vs σ_{ext}; (d) Δ_i vs initial p. Legend: (—) M1 [66], (—) ES7 [67], (—) BG7 [68], (—) D7 [69], (—) J20 [70], (—) K30 [71], (—) USCII [72], (—) Z22 [73], and experimental data points [74–80].

The performance of these mechanisms was assessed by comparing calculated laminar flame speeds (s_u), ignition delay times (τ_{ign}), and extinction strain rates (σ_{ext}) against experimental data as shown in Figure 4.1(a) to (c). The analysis of ignition delay revealed that while most mechanisms are comparable above 1000 K, significant discrepancies arise in the 850 K to 1000 K range. Simpler models failed to capture the non-linear 'kink' in the experimental data due to the omission of H_2O_2 and HO_2 chemistry. Conversely, while many detailed mechanisms over-predicted ignition durations in this range, the Z22 mechanism accurately reproduced experimental trends, fulfilling its primary design criteria. Similar trends were observed for s_u and σ_{ext}, where the detailed mechanisms, specifically J20, Z22, K30 and USCII, showed superior alignment with experimental measurements compared to the smaller models.

For the specific study of detonations, the induction length (Δ_i) was also evaluated through one-dimensional steady-state calculations, as displayed in Figure 4.1(d). By relating this length to detonation cell size data using a scaling parameter of $k = 50$, it was found that the Z22 and J20 mechanisms provided the closest agreement with experimental observations.

In view of these, Z22 has been selected as the foundational reaction mechanism for all simulations presented in this thesis due to its consistent performance across all critical combustion parameters.

4.4 Computational Domain, Mesh, and Boundary Conditions

To translate the mathematical framework into a discrete simulation, the physical geometry of the combustion chamber must be defined and meshed. The boundary conditions for the simulation were designed to mirror the experimental environment as realistically as possible, while incorporating necessary simplifications for computational pragmatism.

As introduced theoretically in Section 3.7, a subgrid wall model is utilised to manage near-wall resolution requirements without necessitating a prohibitively fine mesh at the boundaries. The combustion chamber walls were modelled using a no-slip adiabatic boundary condition. This adiabatic assumption is justified by the extremely short experimental durations, which minimise the influence of thermal conduction through the solid walls. At the combustor outlet, a wave-transmissive boundary condition was applied to the pressure field to prevent artificial wave reflections from contaminating the domain, while all other flow variables were extrapolated using a zero-gradient condition.

4.4.1 Mesh Resolution Strategy

The simulation campaign commenced with the development of the computational model and the execution of Case Study A (elaborated in Section 5.1). To ensure both numerical accuracy and computational efficiency, a series of four structured hexahedral meshes was generated with progressively increasing spatial resolutions. These meshes featured respective base cell dimensions of 0.95 mm (Mesh A(i)), 0.47 mm (Mesh A(ii)), 0.26 mm (Mesh A(iii)), and 0.19 mm (Mesh A(iv)).

This multi-grid approach served a dual purpose: first, to facilitate a rigorous mesh sensitivity analysis; second, to enable a stepped, computationally efficient initiation strategy for the detonation waves. The mesh refinement study demonstrated that statistical mesh independence was achieved beginning with Mesh A(iii). Consequently, the 0.26 mm base-sized Mesh A(iii) was adopted as the primary baseline for the majority of the subsequent simulations within

this thesis. A detailed elaboration on the sensitivity study and the criteria for selecting this baseline resolution is provided in Section 6.1.1.

4.5 Simulation Workflow: Initiation and Data Acquisition

The initiation of the detonation wave was designed to feature a more 'organic development' than standard numerical approaches (e.g., [81]). After a brief pre-filling period of the chamber with reactants for 60 μs, detonation was triggered numerically by a spherical ignition kernel centred 15 mm downstream from the injection plane. This kernel possessed a temperature of 1500 K and a pressure of 20 bar, combined with a tangential velocity of 2000 m/s. In certain respects, this methodology resembles the tangential detonation tubes used in experimental rigs. It should, however, be noted that this numerical initiation approach is not meant to identically mimic the ignition sequence in the experiments, but rather to start the ILES computation, whereafter the flow field is allowed to develop freely.

Regarding the overall simulation workflow, each investigated case was systematically initiated using the intermediate resolution of Mesh A(ii). A time series of instantaneous temperature contour plots for a sample case (Case Study A1) is shown in Figure 4.2 to illustrate the highly transient behaviour during the simulation start-up on this mesh and the subsequent transition to steady wave propagation. The time spacing between snapshots is not constant, as the selected instants have been chosen specifically to showcase the most significant events inside the combustor.

The first image depicts a time shortly after "ignition", where a strong detonation wave has been triggered in a tangential (clockwise) direction. In the second instant, it can be seen that a second, weaker pressure wave also spawns and propagates in the opposite direction. The next two pictures respectively show the moments before and after the two waves collide, resulting in the detonation wave's engulfment of the weaker pressure wave. The following three images depict the aftermath of the wave interactions: a stable single-wave mode forming in the combustor, with the distinct high-temperature remnants of the collision flowing towards the outlet as the rest of the chamber begins filling up with hot products from the wave's first cycle.

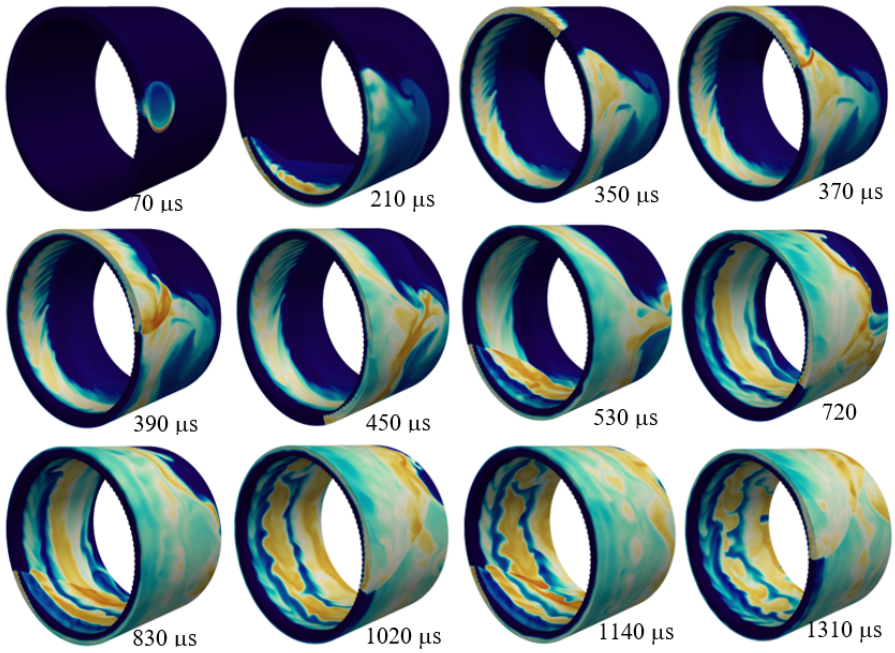

Figure 4.2: Time-series of T (isometric front view) for Case A1 on Mesh A(ii), illustrating highly unsteady start-up phase. From wave initiation, chaotic developments, and eventually stable single-wave mode.

From the snapshot taken at 720 μs, a visible trail of aftereffects from the wave sweep, e.g., slip-line formation (elaborated in Section 6.4.1), can be seen on both the inner and outer wall surfaces. In the subsequent three pictures, the increasing "columns" of temperature stratification arising from the individual wave cycles can be observed, especially on the inner annulus wall. The final image portrays the wave after three full revolutions, with the hot products having filled the entire axial length of the combustor. Interestingly, the wave has also become more developed, with the oblique shock fully extending from the detonation wave to the outlet.

To quantitatively determine when the detonation structure had achieved a steady cycle, temporal parameter traces were monitored, allowing for the simulation to be mapped from Mesh A(ii) to Mesh A(iii) suitably. The appropriate state for the mesh switch was identified using variables such as the instantaneous static pressure. As an example, the graphs in Figure 4.3 show the time variation of the static pressure, p, and temperature, T, on the outer annular wall at 25.4 mm downstream of the fuel injection surface, retrieved respectively from the initialisation phase of Case A1 on Mesh A(ii) and the subsequent finer Mesh A(iii) runs. This plotting mimics the measurement of high-frequency static pressure in the experimental combustor channel [82].

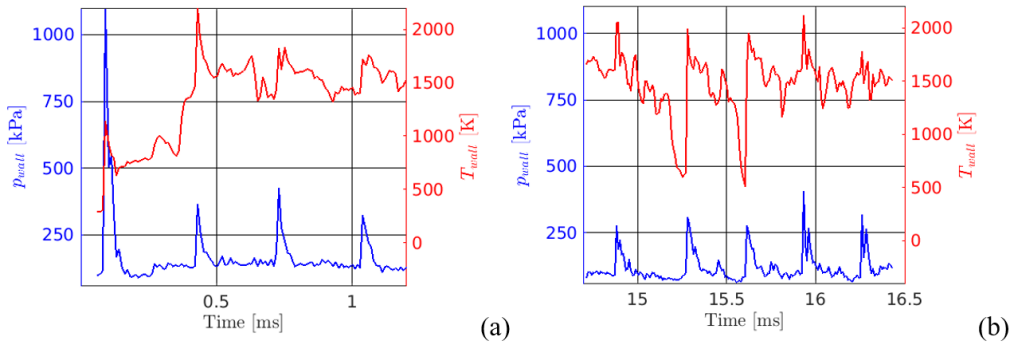

Figure 4.3: (a) p (blue) and T (red) against time for Case A1 initialisation on Mesh A(ii). After 'ignition' spike, p settled into steady cycles. (b) Corresponding graphs after data mapping and run continued on Mesh A(iii).

From the truncated plot (sufficient for the purpose of trend illustration) shown in Figure 4.3(a), it is apparent that the initial pressure spike from the initialisation transitions into a stable cycle from around 0.4 ms onwards. The temperature curve portrays a similar situation; the parameter at the measured location records a small spike due to the initial ignition, and then climbs to and stabilises at a range largely between 1300 K and 2100 K. With the onset of the stable circling wave configuration verified, the switch to the refined mesh was performed. Figure 4.3(b) shows the instantaneous static chamber p and T plots against time for the statistically-steady Case A1 simulated using Mesh A(iii). From this baseline, the data was also subsequently further mapped to Mesh A(iv) to complete the mesh sensitivity analysis.

Chapter 5

Case Studies

This chapter introduces the investigated case studies, respectively based on the AFRL and University of Cincinnati RDC geometries.

5.1 Case Study A – AFRL RDC Design

The first case study focuses on a non-premixed hydrogen-air RDC. This specific design, developed by the US AFRL, was selected due to its practical configuration and the availability of extensive experimental benchmark data. The experimental campaign, led by Rankin *et al.* [82], applied OH^* chemiluminescence imaging and high-frequency pressure measurements to visualise detonation structures and quantify wave speeds in an optically accessible engine combustor. A variety of other pressure sensors, e.g., CTAP sensors, were also used to make key measurements for various forms of evaluation.

5.1.1 Combustor Geometry and Simulation Model Set-Up

The physical hardware features an annular detonation channel with inner and outer diameters of 138.7 mm and 153.9 mm, respectively, and an axial length of 101.6 mm. Air is injected from a plenum through a circumferential slot on the inner wall, while hydrogen is supplied through 120 individual injectors (0.89 mm diameter) evenly spaced near the inner edge of the channel. This design utilises a "jet-in-crossflow" injection scheme, where the fuel and oxidiser are introduced at different angles to promote rapid mixing within the extremely short timescales

required for detonative combustion. Figure 5.1(a) shows a cross-section of the AFRL RDC.

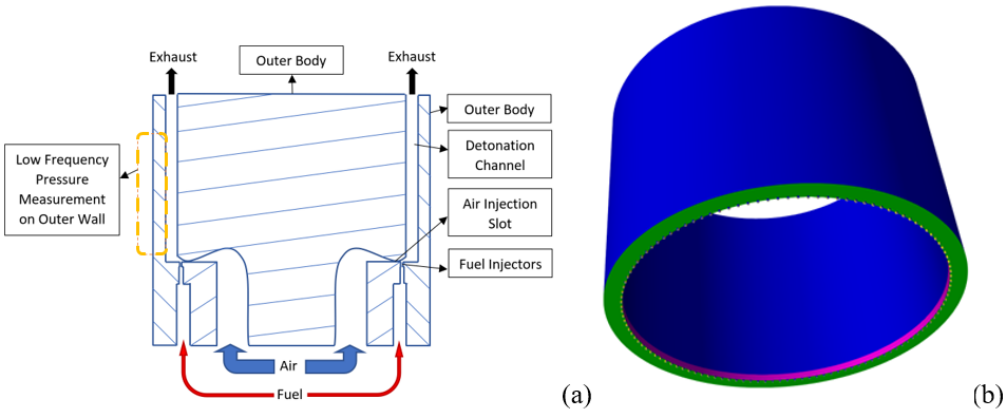

Figure 5.1: (a) Simplified cross-sectional schematic of the AFRL hardware design, displaying flow paths and transducer positions, [83]. (b) Simulation model for Case Study A; inlets, combustor base and walls shown in different colours.

The computational domain was designed to replicate the non-premixed experimental hardware as closely as practically possible. The model represents an annular chamber with identical axial length, outer and inner diameters, and a constant channel width. The injection system, consisting of a 3.56 mm air slot and 120 cuboid fuel injectors, was modelled using equivalent areas to ensure a rational comparison with the experimental setup. Figure 5.1(b) shows the computer-aided design (CAD) model of the computational setup, with the annular walls in blue, chamber base coloured green, small H_2 tubes in yellow, and air inlet slot displayed in magenta.

To ensure the results were reliable and independent of the grid resolution, a mesh sensitivity study was conducted using four structured hexahedral meshes ranging from 0.77 million to nearly 50 million cells. Statistical independence was established at a base cell size of 0.26 mm with Mesh A(iii) (consisting of 20.9 million cells in total), which was then adopted as the baseline for the main body of research. The application of a subgrid wall model allowed for the use of relatively uniform meshes without sacrificing accuracy in the boundary layers, as explained in Section 3.7. This resolution was determined to be sufficient for capturing intricate wave features, such as diagonal slip-lines and turbulent vortical patterns, while maintaining computational efficiency; the mesh insensitivity will be elaborated in Section 6.1.1.

5.1.2 Operating and Inlet Boundary Conditions

In addition to the boundary conditions explained in Section 4.4, fixed inlet mass flow rates were prescribed. The reactants were introduced at fixed temperatures (295 K for the air inlet and 243 K for the hydrogen inlet) with specified species mass fractions ($Y_{O_2} = 0.233$ and $Y_{N_2} = 0.767$ for air inlet; $Y_{H_2} = 1$ for the fuel inlet). The primary control parameters across the study were the inlet mass flow rates for fuel ($\dot{m}_{H_2}$) and air ($\dot{m}_{air}$). Two specific cases were investigated, both maintaining a global stoichiometric equivalence ratio ($\phi = 1.0$):

- **Case A1:** A total air mass flow rate of 0.14 kg/s and hydrogen flow of 0.0041 kg/s.
- **Case A2:** A doubled flow rate with 0.32 kg/s of air and 0.0092 kg/s of H_2.

5.1.3 Summary of Conditions and Key Results

Table 5.1 summarises the main results from the two ILES runs performed on Case Study A.

Table 5.1: Key ILES Results for Cases A1 and A2

Test Data	**Case A1**		**Case A2**	
	EXP	LES	EXP	LES
ϕ	1.0			
$\dot{m}_{air}$ [kg/s]	0.14		0.32	
$\dot{m}_{H_2}$ [kg/s]	0.0041		0.0092	
Wave number, N	1	1	1	2
Wave frequency [kHz]	2.99	3.06	3.69	2.99
Oblique shock angle [°]	—	60	74	60
Combustion efficiency, E_{comb} [%]	—	89.2	—	86.6

In the simulated dual-wave configuration of Case A2, the specified frequency refers to the parameters of each individual wave. The observed rise in mass flow between Cases A1 and A2 appears correlated with the increase in wave number. Although Rankin *et al.* [82] did not record multiple waves for Case A2 experimentally, similar transitions to higher wave counts at other increased air

flow rates have been documented both in, [82], and other studies such as Feleo *et al.*'s [84].

The computed wave rotation frequencies in this case study exceed experimental measurements by 6% to 13%. Notably, the simulated frequencies decreased slightly as mass flow increased, whereas the experimental data for Case A2 showed a marginal increase (from Case A1). This discrepancy may stem from differences in predicted wave numbers; it is hypothesised that detonation wave bifurcation reduces individual wave intensity and propagation speed compared to if a hypothetical single-wave state was to occur in Case A2.

Although no standard RDC performance metric has been adopted currently, a preliminary indicator is combustion efficiency, defined as $E_{\text{comb}} = 1 - \dot{m}_{\text{fuel}}^{\text{out}} / \dot{m}_{\text{fuel}}^{\text{in}}$, where $\dot{m}_{\text{fuel}}^{\text{out}}$ and $\dot{m}_{\text{fuel}}^{\text{in}}$ refer to the H_2 mass flow rates leaving the outlet and injecting through the fuel inlets respectively [81]. While efficiency varied only slightly between cases, Case A2 consumed substantially more hydrogen due to its near-doubled injection rate. The minor fluctuations in combustion efficiency may also be influenced by the wave count, potentially in turn affected by variations in mixing duration and reactant quality ahead of the wave fronts.

5.2 Case Study B – University of Cincinnati RDC Design – On-Going Research

The second case study involves a numerical investigation of a different RDC design, aimed at assessing the robustness and versatility of the ILES model across varying geometries and injector configurations. Having the same annular combustor form and a similar injection concept, this configuration is modelled after an experimental campaign conducted at the University of Cincinnati, which explored the existence and multiplicity of waves in a radial-inward injection environment.

5.2.1 Geometric and Numerical Configurations

As evident in Figure 5.2(a), which displays the cross-sectioned combustor flow paths for half the geometry, this design is highly similar to the AFRL design [82] in terms of the operating concept. The geometry of Case Study B shares several identical dimensions with the previous case, including the inner and outer diameters. The key difference is that the reactant injectors are here situated around the outer wall, instead of the inner one. The detailed structural differences are:

- **Chamber Length:** The axial length of the channel is around 140 mm, making it roughly 40% longer than the hardware in Case Study A.
- **Air Injection Scheme:** Unlike the axial setup, the air inlet slot (∼1.0 mm width) is situated on the outer wall to provide radial-inward flow.
- **Fuel Injection:** The hydrogen injectors are also aligned to the outer wall, positioned near the oxidiser slot to facilitate high-velocity crossflow mixing.

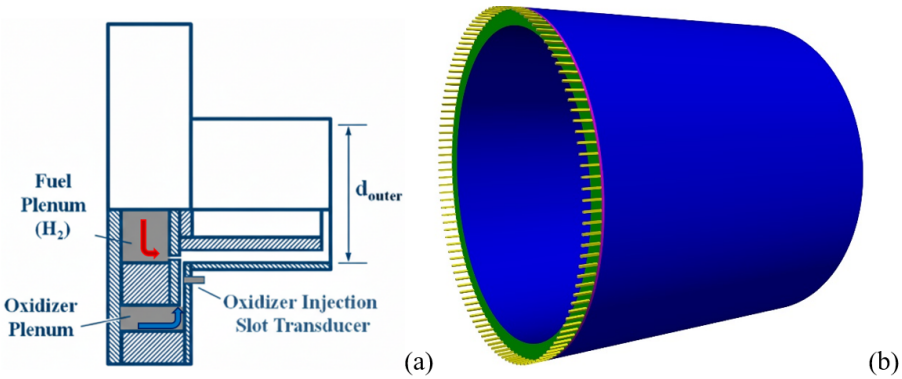

Figure 5.2: (a) Simplified partial cross-sectional schematic of the University of Cincinnati hardware design, displaying flow paths and plenums [85]. (b) Simulation model for Case Study B; inlets, combustor base and walls shown in different colours.

Correspondingly, Figure 5.2(b) shows the annular walls, combustor base surface, fuel injectors and air inlet, in the same colour scheme as the AFRL CAD model of Figure 5.1(b).

Notably, the H_2 injection tubes here are significantly longer, as modelled as accurately as possible since the specific detail could be derived from the experimental publication [85], whereas the corresponding information was omitted in Rankin *et al.*'s [82] article.

Building upon the mesh sensitivity findings from Case Study A, the simulations for this geometry followed the similar progressive resolution strategy. High-fidelity results were obtained by first establishing stable detonation wave propagation on a starting grid (Mesh B(ii)) before mapping the flow fields onto a refined baseline Mesh B(iii) for final data extraction and analysis.

To maintain consistency in spatial resolution across the two study cases, the mesh base cell sizes were kept similar to those used in Case Study A. Specifically, Mesh B(ii) utilised a base cell size of 0.47 mm, while the more refined Mesh B(iii)

featured a 0.26 mm base cell size. Due to the longer chamber length compared to the first case study, this resolution resulted in significantly higher total cell counts of approximately 7 million for Mesh B(ii) and 27 million for Mesh B(iii).

5.2.2 Experimental Case Selections and Operating Conditions

Two specific operating points were selected from the experimental map to evaluate the model's ability to predict wave multiplicity. Both cases maintain a global stoichiometric equivalence ratio ($\phi = 1.0$) but differ in their oxidiser composition:

- **Case B1** (H_2-air): This case utilises standard air as the oxidiser with a mass flow rate of 0.3 kg/s. It was intentionally selected from experimental runs that observed a single dominant detonation wave ($N = 1$).
- **Case B2** (H_2 with oxygen-enriched air): To investigate the effects of increased detonability, this case uses "oxygen-enriched air" with a nitrogen dilution ratio of $\beta = 2.45$ (where $\beta = N_2 : O_2$). The total oxidiser flow rate is maintained while the fuel flow is adjusted to maintain stoichiometry.

The prime objectives of these simulations are to determine if the LES model can accurately capture the experimentally measured global metrics and also the different wave numbers, which are often associated with changes in the normalised perimeter (p/λ), as the mixture sensitivity is increased through oxygen enrichment.

5.2.3 Summary of Conditions and Key Results

Table 5.2 summarises the global operating conditions and the macroscopic results obtained from the experimental campaign and the corresponding ILES runs for Case Study B. Because this case study represents an on-going, developing phase of the research, the intermediate-resolution Mesh B(ii) formed the backbone of these investigations. Utilising this mesh allowed for fast, computationally economic test simulations to efficiently investigate overarching physical trends. Given the large number of simulation runs required, including testing two distinct initiation paths for Case B2 and also separate trials incorporating the PaSR model, it was more sensibly practical to rely on Mesh B(ii) to maintain a manageable computational cost.

To examine the stability of the wave multiplicity observed in the oxygen-enriched Case B2, the simulation was evaluated using two distinct initiation strategies. The first approach mapped the stabilised single-wave solution from Case B1 onto the Case B2 conditions (labelled "LES from Case 1"). The second approach initiated the detonation entirely from a resting state using the identical numerical spark ignition strategy as before (labelled "LES from scratch").

Table 5.2: Key Experimental [86, 87] and ILES Results for Cases B1 and B2

Test Data	**Case B1**		**Case B2**		
	EXP	LES	EXP	LES (fr Case 1)	LES (fr scratch)
ϕ				1.0	
$\dot{m}_{\text{air}}$ [kg/s]				0.3	
$\dot{m}_{\text{H}_2}$ [kg/s]	0.0088			0.0119	
Wave number, N	1	1	2	1	3
Wave frequency [kHz]	3.2	3.77	4.0	4.62	3.6
Average Chamber Pressure [kPa]	123	140	—	153	144
Combustion efficiency, E_{comb} [%]	—	79.7	—	81.7	82.7

In Case B1, the numerical framework successfully captures the experimentally observed single-wave mode ($N = 1$).

However, for the oxygen-enriched conditions of Case B2, the predicted wave multiplicity appears to exhibit a dependence on the numerical initiation strategy and deviates from the experimental two-wave observation ($N = 2$). When the flow fields were mapped from the stabilised Case B1 solution, followed by relevant flow condition changes corresponding to Case B2, the run sustained a single-wave state. Conversely, initiating the domain entirely from scratch yields a three-wave configuration ($N = 3$). The computed wave rotation frequency for Case B1 overpredicts the experimental measurement by roughly 18%. In Case B2, the simulated frequencies clearly reflect the impact of wave multiplicity: the single-wave configuration propagates at 4.62 kHz, whereas the individual waves in the three-wave configuration travel significantly slower at 3.6 kHz. This observation further reinforces the hypothesis presented in Case Study A, suggesting that an increased wave count distributes the available reactants across more fronts, thereby reducing individual wave intensity and propagation speed.

Average chamber pressures within the simulations moderately exceed the available experimental data for Case B1 (140 kPa computed versus 123 kPa measured). For Case B2, the higher hydrogen injection rate naturally drives an increase in the simulated chamber pressure; however, the $N = 3$ state yields a

slightly lower average pressure (144 kPa) compared to its $N = 1$ counterpart (153 kPa), with experimental data unavailable.

Combustion efficiency across the cases follows a similar trend to Case Study A, remaining relatively stable but showing a slight improvement in the higher-reactivity Case B2 environment. Notably, within Case B2, the three-wave configuration demonstrates a marginally higher combustion efficiency (82.7%) than the single-wave configuration (81.7%).

These two distinct runs of Case B2 present a basis for comparing different wave modes operating under exactly the same global flow conditions. The minor variation in performance appears to imply that the more frequent passage of detonation fronts in higher wave-count modes alters both the refill and mixing dynamics, alongside the frequency of the 'combustive wave sweeps'. Consequently, this may enhance the overall reactant conversion rate, even as the mixing duration (before the next wavefront arrival) tends to be shorter and the intensity of the individual waves is weakened. Nevertheless, it must be stressed that this observation is not yet a universal conclusion, and establishing a definitive physical trend will require further dedicated investigation.

Chapter 6

Results and Analyses

This chapter contains a series of carefully-selected results and findings, seeking to present a representative overview of the research scope and significance.

6.1 Framework Validation and Sensitivity

This sub-section showcases the systematic approach that derived the ILES framework undertaken in this research.

6.1.1 Mesh Sensitivity and Resolution Requirements

In LES, the mesh resolution is intrinsically linked to the governing equations themselves, as the LES filter width is typically derived from cell volumes. As a result, the mesh does not merely dictate the discretisation error but also determines the boundary between resolved and unresolved scales within the turbulent energy cascade [88]. It is therefore essential to evaluate the impact of mesh resolution on simulation results before they are subjected to further analysis.

To evaluate these sensitivities, a systematic refinement study was conducted using four structured hexahedral meshes for the primary case study (A). Qualitative comparisons of instantaneous temperature (T) contours in Figure 6.1, reveal a progressive increase in captured physical detail as the mesh is refined. While the coarsest Mesh A(i) only permits the identification of generic wave structures, Mesh A(ii) begins to resolve distinguishable flow field patterns. Sig-

nificant improvements are observed with Mesh A(iii), which successfully resolves intricate features such as contact burning zones and the slip-line separating products from subsequent cycles. The finest Mesh A(iv) provides the most granular detail, capturing vortex-like structures behind the oblique shock and a more distinct geometrical profile of the detonation wavefront.

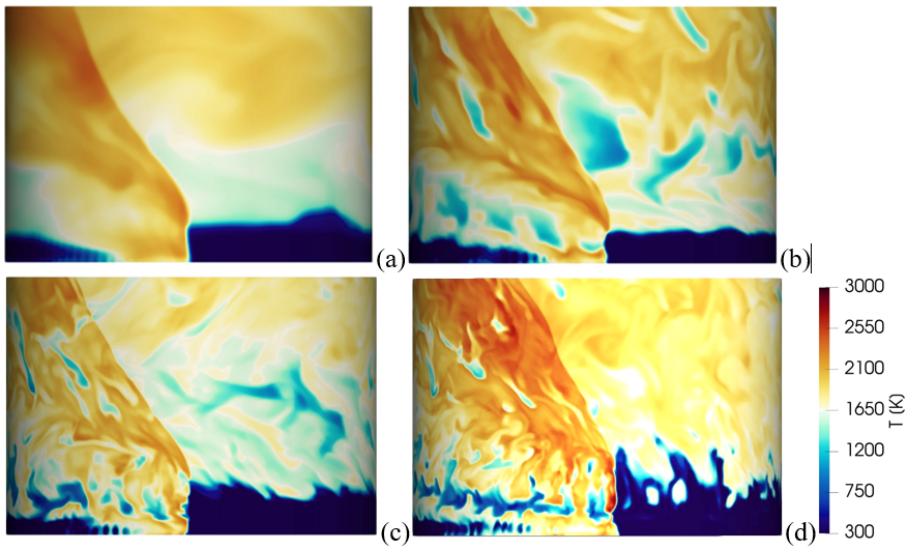

Figure 6.1: Instantaneous T plots on the mid-channel cylindrical section of (a) Mesh A(i), (b) Mesh A(ii), (c) Mesh A(iii) and (d) Mesh A(iv), presented in a side-on view.

A quantitative assessment was further performed by acquiring time-averaged pressure ($\langle p_{\text{wall}} \rangle$) and temperature ($\langle T_{\text{wall}} \rangle$) data along the combustor's outer wall, as shown in Figure 6.2. Comparisons with experimental data show that Mesh A(i) significantly under-predicted mean pressure. However, the profiles for Meshes A(ii), A(iii), and A(iv) show high degrees of similarity, with curves generally remaining within 8% of one another.

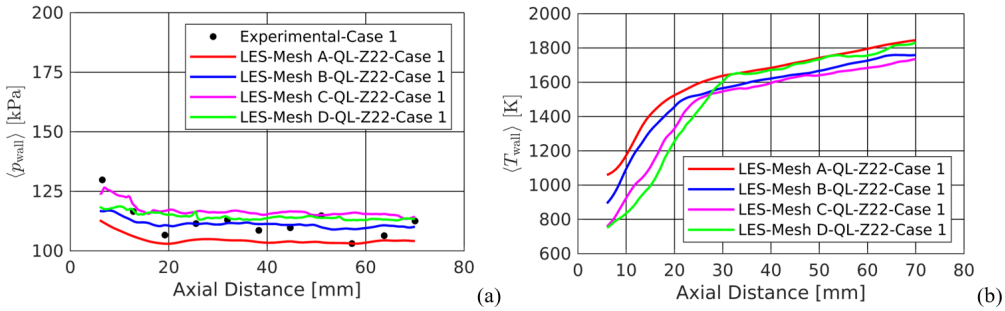

Figure 6.2: (a) Plot of time-averaged $\langle \boldsymbol{p}_{\text{wall}} \rangle$ and (b) temperature $\langle \boldsymbol{T}_{\text{wall}} \rangle$ against axial distance for Case A1 using four meshes (here, labelled as Meshes A, B, C and D), with experimental $\langle \boldsymbol{p}_{\text{ch}} \rangle$ data points [82].

Most importantly, the results for the two finest meshes (A(iii) and A(iv)) exhibit noticeable overlapping in both pressure and temperature distributions. This convergence indicates a clear trend toward statistical mesh independence. Given these overlapping trends and Mesh A(iii)'s proven capability to resolve the critical fine structures mentioned above, the 20.9 million-cell mesh was adopted as the baseline for the majority of the subsequent simulations.

6.1.2 Chemical Reaction Mechanism Sensitivity

The choice of chemical kinetics is an integral factor in simulating detonation waves, where the stability of the wave depends on the coupling between the lead shock and the heat release (reaction) zone. To evaluate this sensitivity, a comparative study was performed using five hydrogen-air mechanisms: the global single-step M1, the skeletal BG7, the 22-step Z22 used throughout this work, and the detailed J20 and S23 mechanisms.

A distinct divergence in simulated wave stability was observed among these models. While the M1, BG7, and Z22 mechanisms sustained robust detonation waves, the detailed J20 and S23 mechanisms failed to maintain shock-reaction coupling, leading to gradual wave extinction. This counter-intuitive failure of the detailed mechanisms is attributed to chemical stiffness, which is revealed as an issue in the presence of widely varying reaction time scales. J20 and S23 predict physically realistic but highly sensitive induction lengths, Δ_i, and typically require extremely fine spatial resolution. On the current ILES grid (Mesh A(iii)), the numerical dissipation of the shock front causes a slight drop in post-shock temperature. For the stiff J20 and S23 mechanisms, this small temperature deficit causes the induction time to increase, effectively decoupling the flame from the shock, and sufficient enough to lead to "flame-off".

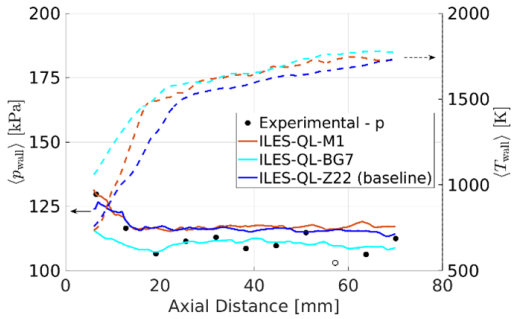

Figure 6.3: Comparison of time-averaged wall pressure profiles for different reaction mechanisms against experimental data points [82], performed on Mesh A(iii).

Among the surviving mechanisms, a quantitative assessment was performed against experimental data [82] in Figure 6.3. The time-averaged wall pressure profiles ($\langle p_{\text{wall}} \rangle$) reveal that the M1 and Z22 mechanisms predict similar magnitudes, whereas the BG7 mechanism yields notably lower values. Due to the scatter in the experimental data points, both the Z22 and BG7 curves intersect with approximately the same number of validation points, making pressure magnitude alone an insufficient discriminator. However, the wave frequency (f) in Table 6.1 serves as a decisive tie-breaker. The Z22 mechanism predicted a wave frequency that falls within 6% of the experimental value. In contrast, the simpler M1 and BG7 mechanisms over-predicted the frequency by 19% and 11%, respectively.

Table 6.1: Wave frequencies and combustion efficiencies for reaction mechanisms, performed on Case A1

	EXP	**LES**		
		Mesh A(iii) QL M1	Mesh A(iii) QL BG7	Mesh A(iii) QL Z22
f, kHz	2.99	3.56	3.33	3.06
E_{comb} [%]	—	85.7	85.9	89.2

This over-prediction by the skeletal and global mechanisms is consistent with their formulation. M1 and BG7 lack the comprehensive set of reaction pathways present in Z22. Resultantly, they behave hyper-reactively in the 850–1000 K range, releasing heat almost instantaneously and driving the wave faster than physically observed. Furthermore, the Z22 mechanism largely predicts lower mean wall temperatures than its simpler counterparts. By resolving more intermediate reaction steps, Z22 distributes the heat release over a finite induction zone, likely leading to the lower temperatures.

In conclusion, the Z22 mechanism occupies a "balanced state" in modelling fidelity. It avoids the unphysical hyper-reactivity of small reaction schemes, and yet possesses enough numerical robustness to survive the numerical dissipation (with respect to the concerned mesh) that extinguishes the detonation in the stiffer and more detailed mechanisms. This balance validates its selection as the baseline for this thesis. Additionally, the baseline LES framework is deemed capable of capturing the primary pressure-gain characteristics and operating frequencies of Rankin *et al.*'s experimental RDC.

6.2 Wave Multiplicity and Effects of Numerical Models

While the baseline framework accurately resolves the global operating frequency, a distinct discrepancy arises regarding wave multiplicity. In both the primary (AFRL) and secondary (University of Cincinnati) geometries, the LES framework accurately predicted the single-wave mode ($N = 1$) at lower mass flow rates and with air as the oxidiser (Cases A1 and B1), matching experimental observations.

However, a distinct discrepancy emerged at a higher mass flow rate (for Case Study A) or when there are oxygen-enriched reactants (for Case Study B). For the high mass flow condition (Case A2) and higher-proportioned oxygen scenario (Case B2), the simulations consistently predicted a transition to a stable co-rotating wave mode with one more wave than the corresponding experimental campaigns.

An important consequence of this over-predicted wave number is its direct effect on the individual wave characteristics, most notably the wave frequency. As presented previously in Table 5.1, the experimental wave frequency for Case A2 was measured as 3.69 kHz for a single-wave mode, whereas ILES predicted a lower individual frequency of 2.99 kHz for each of its two waves. This reduction in frequency strongly aligns with physical understanding. Because the simulation operates at the same global mass injection rate as the experiment, the presence of two waves effectively halves the available reactants per cycle. Furthermore, the doubled wave number reduces the injector recovery window, leaving significantly less time for adequate reactant mixing ahead of each wavefront. Therefore, this leads to the simulation developing two weaker waves relative to the single experimental wave; this is a phenomenon physically evident in the lower wave height and the reduced individual wave propagation frequency.

To ensure this multiplicity is not an artifact of the computational setup, a targeted investigation into the effects of specific numerical models (such as wall heat transfer, thermal radiation, and TCI) was conducted. The detailed sensitivity analyses were performed on Case A2 (AFRL) in an attempt to isolate the cause. The two-wave mode remained the dominant attractor across variations in:

1. **Chemical Kinetics:** Comparing the Z22 mechanism against the global M1 mechanism.
2. **Heat Transfer Physics:** Including Conjugate Heat Transfer (CHT) and P1 thermal radiation models to account for wall losses.
3. **Numerical Resolution:** Refining the grid (Mesh A(iv), but labelled as "Mesh D" in figure) to resolve finer turbulence scales.

The time-averaged wall pressure and temperature across the datasets are shown in Figure 6.4. In the legend labels: "QL" refers to 'quasi-laminar' with no TCI model applied, also sometimes known as the "perfectly stirred reactor"; "CHT" stands for the application of one-dimensional conjugate heat transfer; "P1" represents the use of the P1 radiation model [89]; "PaSR" denotes having applied the Partially Stirred Reactor TCI model [90]. In addition, Table 6.2 lists the wave frequencies and combustion efficiencies across the investigated runs. All datasets fell within 5% of one another.

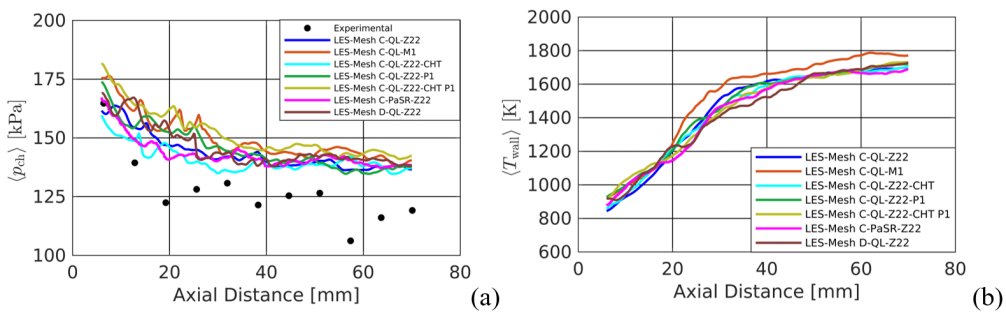

Figure 6.4: For Case A2, (a) $\langle p_{\text{wall}} \rangle$ and (b) $\langle T_{\text{wall}} \rangle$ generated with Z22 mechanism; M1 mechanism; Z22 with CHT (conjugate heat transfer), P1 (radiation), CHT and P1, PaSR model, all on Mesh A(iii) ("Mesh C" in graph); Z22 on Mesh A(iv) ("Mesh D" in graph); with experimental results [82].

None of these physical or numerical enhancements triggered a fall back to the single-wave mode. The persistence of the $N = 2$ solution suggests that the discrepancy is not merely a transient numerical artefact or a grid-dependence issue, nor driven by thermal losses or reaction chemistry which were previously

Table 6.2: Wave frequency and combustion efficiency from model sensitivity for Case A2

	EXP	**LES**						
		Mesh A(iii) QL Z22	Mesh A(iii) QL M1	Mesh A(iii) QL Z22 CHT	Mesh A(iii) QL Z22 P1	Mesh A(iii) QL Z22 CHT P1	Mesh A(iii) PaSR Z22	Mesh A(iv) QL Z22
f, kHz	2.81	2.99	3.41	2.92	2.92	2.96	2.90	2.75
E_{comb} [%]	—	88.7	89.5	90	89.9	90.5	89.8	89.5

hypothesised as potential causes. Instead, a deduction based on observations is that at these higher flow conditions, the increased axial refill height provides sufficient spatial 'room' for a second detonation front to anchor and remain stable within the fresh reactant wedge. While this confirms the LES framework's ability to resolve multi-wave solutions, the continued discrepancy with experimental $N = 1$ observations highlights a selection mechanism issue.

This specific inconsistency, of LES predicting higher wave counts than experiments, is not unique to this work. Similar over-predictions of wave multiplicity have been reported across various high-fidelity studies in the community (e.g., [20, 41, 91, 92]).

This convergence of "result discrepancies" across the field suggests a common modelling deficiency. Two hypotheses emerge:

1. **Possible physical reality and bi-stability:** At these flow conditions, the RDC system may physically support both $N = 1$ and $N = 2$ modes. The simulation, initiated from an artificial multi-wave perturbation, settles into the $N = 2$ local minimum, whereas the particular experimental runs' conditions (e.g., ignition sequence) led to the $N = 1$ branch.

2. **Modelling of reactant injections:** The current model utilises a fixed-mass-flow inlet boundary condition. In reality, the injector is coupled to a physical plenum volume that acts as a pneumatic spring-damper system. By omitting the full plenum geometry, the simulation may be artificially "stiff", allowing the second wave to survive pressure fluctuations that would otherwise be dampened by the plenum dynamics in the physical experiment. While the LES accurately resolves the capacity for multiplicity via refill height, this inconsistency potentially highlights the critical need for coupled plenum-chamber simulations in our future RDC research.

Additionally, another potential factor that remains un-tested, would be the effects of smaller geometrical simplifications such as wall roughness. Ultimately, while the current framework successfully captures the structure of the wave (as

shown in Section 6.4.1), the computational model's 'selection mechanism' for the global wave number remains a frontier challenge for the broader RDC modelling community.

6.3 Reactant Injection and Mixing

6.3.1 Injector-Wave Coupling and Fuel Suppression

In a non-premixed RDC, the fuel and oxidiser injection processes are not steady; they are intrinsically coupled to the acoustic and compressibility dynamics of the detonation wave. The LES results demonstrate that the detonation wave acts not merely as a consumer of reactants, but also like a dominant flow-regulating valve that periodically disrupts the injection boundary condition.

The interaction between the detonation wave and the reactant injector is governed by the instantaneous pressure difference across the injector face. As the detonation wave sweeps past the injection ports, the local combustor pressure (p_{comb}) spikes significantly, momentarily exceeding the injector feed pressure (p_{injector}). This adverse pressure gradient triggers a fuel suppression mechanism, causing the mass flow rate of hydrogen to drop temporarily to zero (as will be witnessed in Section 6.4.4), and in some instances, resulting in momentary back-flow into the feed lines.

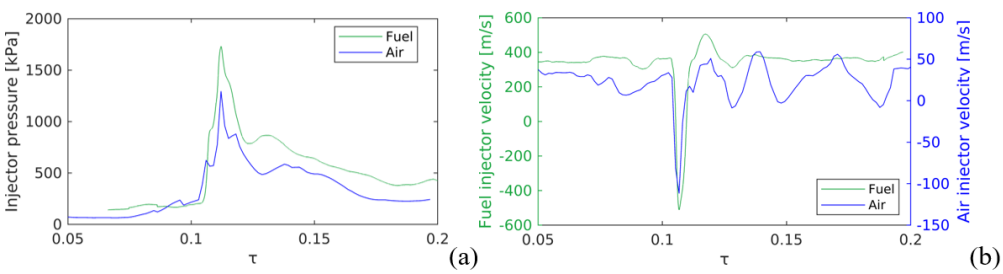

Figure 6.5: Time variation of the response of injector (a) pressure, and (b) velocity.

Figure 6.5 presents the average temporal evolution of injection pressure and velocity for both fuel and air, as triggered by detonation wave passage. The time parameter has been normalised: $\tau = (t - t_0)f/n$, where t_0 is an arbitrary reference time, f denotes the wave propagation frequency, and n is the number of azimuthal waves present in the chamber [48]. The temporal evolution of the injection velocities (Figure 6.5) reveals that this suppression is not merely

a pause, but a violent flow reversal; transient negative velocities are observed, indicating momentary backflow of combustion products into the injector feed lines. The recovery of the injection process is not instantaneous, continuing to be affected by the rapid expansion zone behind the wave. Crucially, the recovery characteristics of the two reactant streams differ significantly. The air injection, which utilises a continuous slot geometry, appears "stiffer" and recovers to its quasi-steady state rapidly following the wave passage. In contrast, the H_2 fuel flow, having relatively lower momentum flux and injected via geometrically isolated tubes, exhibits a notable phase lag, taking longer to re-establish nominal flow. This temporal mismatch between the rapid return of air and the delayed return of fuel is a primary driver of the mixture inhomogeneities that will be showcased in several instances throughout this section. Even if the global equivalence ratio is unity, this dynamic lag creates localised pockets of lean mixture immediately behind the wavefront, further stratifying the refill zone before the reactants have time to mix via shear/turbulence.

6.3.2 Refill Zone Dynamics and Mixing Quality

The periodic suppression and subsequent recovery of the injection create a characteristic "triangular" refill zone of fresh reactants immediately behind the detonation wave. Figure 2.1 (extracted from Case A1) in Section 2.1.2 visualises this structure through the instantaneous temperature field on an unwrapped cylindrical surface. The region of low temperature (blue) identifies the fresh mixture entering the annulus, bounded by the leading detonation front and the trailing contact surface of hot products.

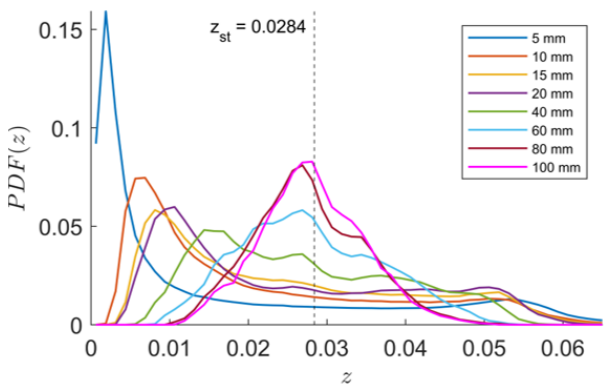

Figure 6.6: At various axial distances, graphs of probability density function for mixture fraction, z.

While the global injection targets stoichiometry ($z_{\mathrm{st}} = 0.0284$), the local mixture

state is highly dependent on the axial distance from the injectors. Figure 6.6 presents the Probability Density Function (PDF) of the mixture fraction (z) at increasing axial heights. Crucially, the PDF reveals that mixing is sharply skewed near the inlet plane. Since the detonation wave anchors in this upstream region (as will be elaborated in Section 6.4.3), it is forced to propagate through a reactant layer that is statistically far from the ideal stoichiometric condition. Although the PDF distributions become more symmetric and peaked near z_{st} further downstream, reflecting the progressive mixing of the streams, this improved homogeneity occurs too late to benefit the primary detonation front. This axial disparity confirms that the RDC operates in a regime where the wave stability is continuously challenged by local stratification.

6.4 Three-Dimensional Wave Dynamics

6.4.1 Replication of Key Detonation Wave Features

A primary objective of this research was to determine if the FRC-ILES framework could reliably replicate the complex 3D topological features inherent to a non-premixed rotating detonation. The simulations successfully captured the multi-faceted structure of the detonation front, which deviates significantly from idealised 1D models by resolving the characteristic cellular morphology governed by the interaction of the Mach stem, the incident shock, and the transverse waves at the triple point [93].

A visual comparison of these topological features for Case A1 is provided in Figure 6.7. The experimental OH^* chemiluminescence shown in Figure 6.7(a) establishes a comparison baseline for the overall wave shape. The corresponding ILES results demonstrate the framework's capability to resolve these structures in high detail, as seen in the volumetric rendering of $\dot{Q}$ in Figure 6.7(b) and the isometric temperature (T) rendering in Figure 6.7(c). These renderings clearly portray the main detonation wave (DW), the oblique shock wave (OSW), and the trailing slip line (SL). Furthermore, the side view in Figure 6.7(d) superimposes multiple flow variables, including $\nabla \cdot \boldsymbol{v}$, p iso-surfaces, λ_2, and H_2 concentration, in order to illustrate the complex 3D spatial distribution of the incoming reactants (R) relative to the primary shock structures.

The most prominent feature identified across the investigated cases is the triple point—a singular junction where the lead shock structures intersect. The LES results clearly resolve the Mach stem, a near-normal shock wave coupled with the primary heat release zone, also commonly referred to simply as the "main

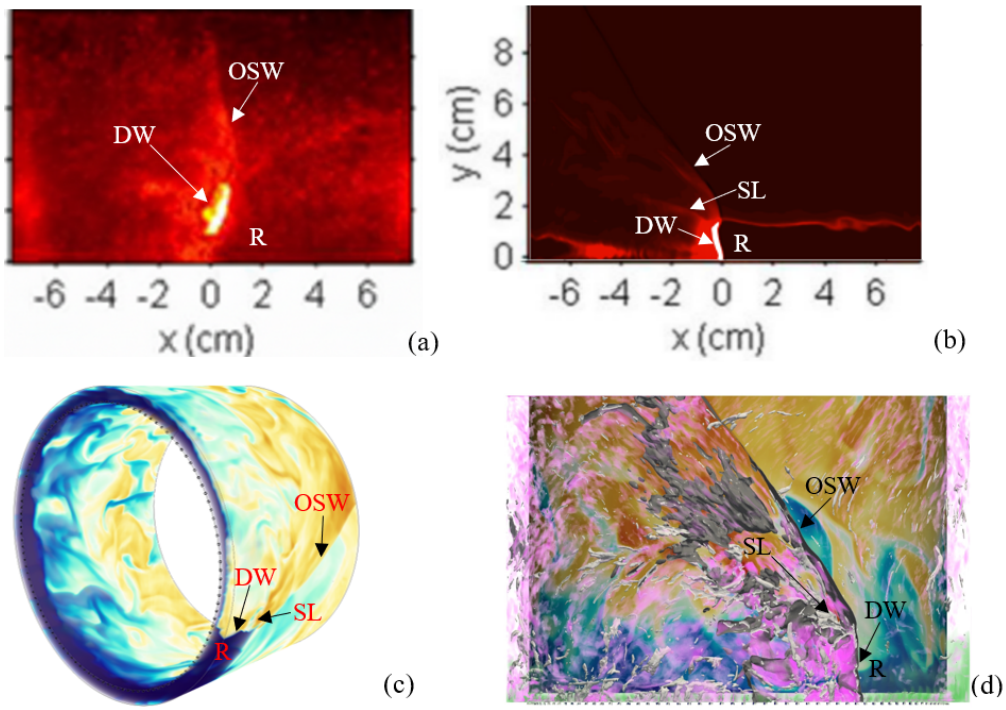

Figure 6.7: Showing key wave features, (a) experimental OH* chemiluminescence image [83]; from ILES: (b) volumetric rendering of $\dot{Q}$, (c) isometric view showing T rendering, and (d) side view of T (warm colours) on inner wall superimposed with renderings of $\nabla \cdot \boldsymbol{v}$ (pink), p iso-surfaces (grey), λ_2 (white), and H_2 concentration (green). All images are for Case A1.

detonation wavefront". Unlike the weaker incident shock, the main wavefront achieves the extreme pressure and temperature rise necessary to trigger near-instantaneous auto-ignition of the H_2-air mixture. Extending from the triple point is a strong oblique shock, which serves to pre-compress the unburnt reactants before they enter the detonation front. This structure is followed by a slip line (contact surface), which separates the high-speed products of the current cycle from the partially processed gases of the previous cycle.

Beyond the primary front, the framework captures the propagation of transverse waves moving perpendicular to the main wave direction. These waves reflect between the inner and outer walls of the annulus, creating localised high-pressure nodes that sweep across the main wavefront. These structures are essential for wave stability, as they provide a mechanism for reigniting pockets of unburnt fuel that might otherwise bypass the main front. The resolution of these transverse instabilities confirms that the numerical framework is consistent with the experimental observations of RDC non-idealities described by Anand and Gutmark [8].

Post-detonation, the flow undergoes a rapid volumetric expansion, resulting in a sharp drop in pressure and a corresponding increase in axial velocity. The LES results highlight a significant flow deflection behind the wave front; the products are expanded both axially toward the nozzle and radially against the combustor walls. This expansion creates a characteristic "triangular" footprint of high-pressure products (the "detonation tail"), which dictates the available area for the subsequent refill of fresh reactants. As noted in previous high-fidelity studies [39], these 3D features are critical for predicting the real-world performance of non-premixed RDCs, where radial stratification is prevalent. Thus, the baseline LES framework is affirmed to successfully replicate the macroscopic propagation features of the rotating detonation wave.

6.4.2 Spatial Radical Distribution

Building upon the overarching macroscopic wave features, it is necessary to examine the internal chemical architecture of the wavefront itself. While pressure and temperature fields portray a picture of the gas dynamics, the spatial distribution of intermediate radicals provides a direct visual illustration of the underlying combustion mechanisms.

Figure 6.8 provides a detailed volumetric rendering of the detonation front's structure, illustrating the spatial distribution of fuel (green), HO_2 (blue) and OH (orange) species, alongside pressure iso-surfaces (dark grey). In contrast to standard deflagration flames, and as detailed in the theories explained in Section 2.1.1, the initial high-pressure shock compression of a detonation creates a distinct induction zone.

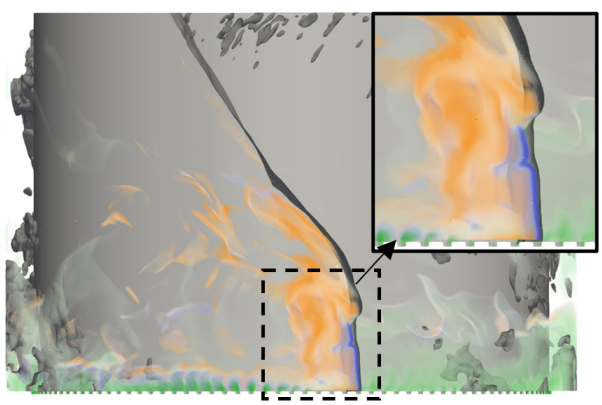

Figure 6.8: Volumetric renderings of HO_2 (blue), OH (orange) and H_2 (green) species concentrations, superimposed with p (grey) iso-surfaces.

The rendered figure clearly captures this phenomenon, showing the main detonation pressure front immediately followed by a distinct HO_2 induction layer. This layer, along with the oblique shock, is tightly trailed by the OH radical bulk that make up the primary reaction zone where the majority of combustion and temperature elevation occurs. Outside this main activity zone, scattered traces of HO_2 and OH indicate the presence of parasitic deflagration ahead of the main wave at the interfaces between cold fuel and hot products from the previous cycle, as well as commensal deflagration where residual fuel burns downstream.

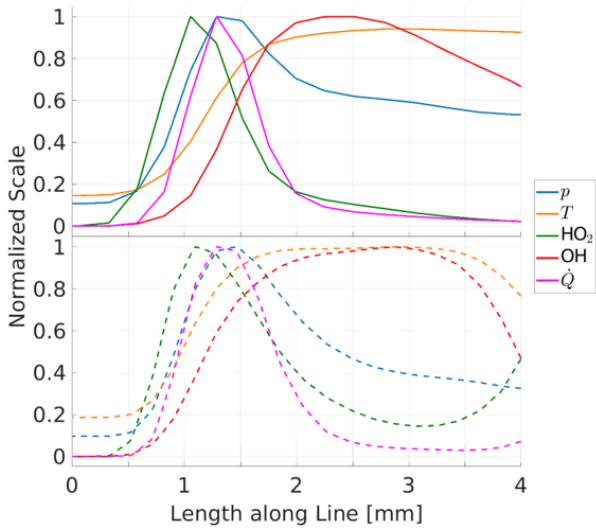

Figure 6.9: Variations of p, T, HO_2, OH and $\dot{Q}$ along a line cutting through the detonation wave, for baseline Mesh C (top; solid) and finer Mesh D (bottom; dashed).

The spatial separation of these features is quantitatively affirmed in Figure 6.9, which plots normalised thermochemical parameters along a straight line cutting through the detonation wavefront. The profile depicts a ZND-like sequence: pressure climbs first at the shock front, triggering a sharp rise and peaking of HO_2. This is spatially offset from, but immediately followed by, a spike in the heat release rate, $\dot{Q}$. Furthermore, Figure 6.9 shows data from both the baseline Mesh A(iii) and the finer Mesh A(iv). The close alignment of the parameter distributions reflects that grid size is not the primary limiting factor in resolving these broader structures, reinforcing the mesh independence findings established earlier in Section 6.1.1.

It should be noted that while this data provides a robust qualitative illustration of the relative species distributions and overall thermochemical trends, caution should be exercised when interpreting the absolute spatial measurements. The

exact spatial dimensions and thicknesses of these zones are inherently influenced by both numerical and turbulent diffusive factors, as respectively outlined in Sections 2.5 and 3.8. While quantifying the precise impact of these factors on RDC simulations is an important area for future study, a detailed investigation falls outside the scope of this thesis.

The clear spatial offset between the shock-induced HO_2 accumulation and the subsequent OH-dominated heat release region confirms a ZND-like structure at the primary detonation wave. On the other hand, the scattered radical traces outside the main activity zone point towards secondary combustion modes that will be statistically evaluated in Section 6.5.3.

6.4.3 Radial Variation and Mixture Stratification

While the volumetric distributions discussed above characterise the global structure of the detonation wave, the annular geometry of the RDC inherently induces strong gradients across the channel width, as mentioned in Section 6.4.1. 2D simulations assume a uniform flow field across the channel, whereas the current 3D LES reveals significant radial dependencies that govern detonation stability. Slicing the domain to examine the radial cross-sections attests that neither the reactant mixing (Section 6.3.2) nor the post-reaction effect is perfectly uniform from the inner to the outer wall.

As the detonation wave propagates through the curved annular channel, the centrifugal effects, varying circumferential distance between the inner and outer walls, and injection dynamics create highly uneven fields in the radial direction. This non-uniformity, shown below, is a dominant factor in determining both the wave structure and the thermal loads on the combustor walls.

Figure 6.10 (a) to (c) respectively display the mean radial flow field distributions of mixture fraction, $z = m_\mathrm{f}/(m_\mathrm{f} + m_\mathrm{a})$, where m_f and m_a represent the masses that originate from the fuel and air streams correspondingly; heat release rate, $\dot{Q}$, and T across the channel thickness. In the figures, the inner annular wall is to the right and the outer wall to the left; the reactants are injected from the bottom-right corner of the cross-sectional images. Analysis of the time-averaged flow fields reveals a consistent 'diagonal' stratification pattern.

As shown in the mixture fraction contours, the high-momentum air stream, injected from the bottom slot, tends to adhere to the inner annular wall. This aerodynamic sealing effect displaces the injected hydrogen towards the outer wall, resulting in a fuel-rich zone in the lower-outer quadrant of the annulus. As

such, the stoichiometric line (z_{st} in Fig. 6.10 (a)) effectively bisects the channel diagonally rather than lying flat or vertical.

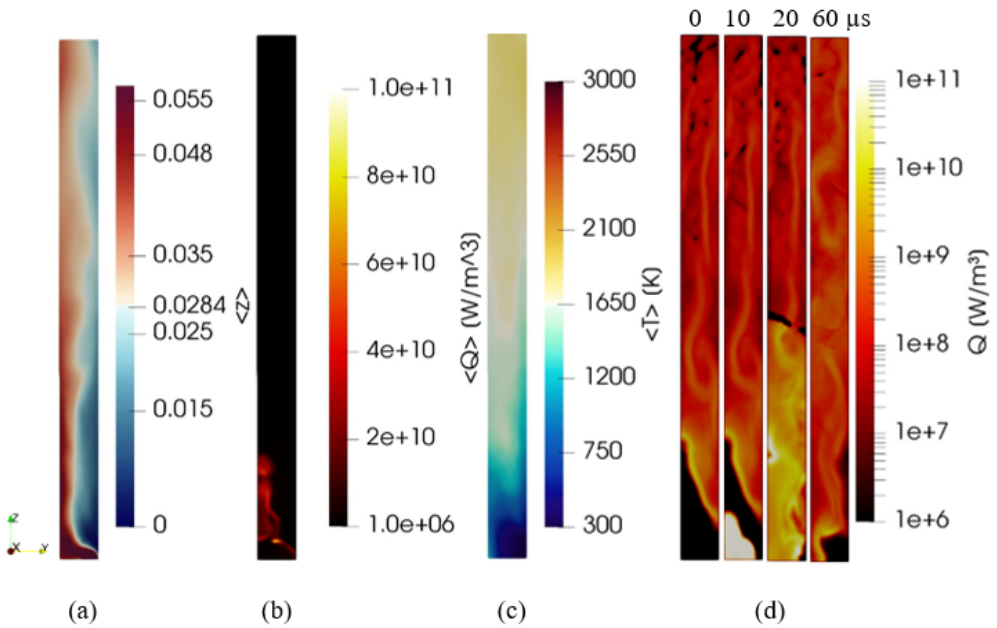

Figure 6.10: Time-averaged radial cross-sections showing (a) mixture fraction (z), (b) heat release rate (Q), and (c) temperature (T). (d) Instantaneous radial cross-sections of heat release rate during a wave passage (t_1 to t_4).

This stratification dictates the behaviour of the detonation wave. As evidenced by Figure 6.10(b), the leading point of the detonation wave does not propagate uniformly across the entire base surface of the cross section; instead, it anchors at the fuel-rich injection corner (bottom-right relative to the image's frame). This confirms literature findings that stronger detonation fronts preferentially align with regions of richer mixture. The wave front then curves outwards, burning through the stratified mixture as it propagates radially toward the outer wall.

The impact of this radial variation is most evident in the temperature field. The time-averaged temperature plot (Figure 6.10(c)) displays a distinct asymmetry in the lower half of the combustor, with significantly higher temperatures concentrated along the outer wall. This is driven by three mechanisms: the accumulation of fuel on the outer wall due to the displacement described above, and the outward volumetric expansion of the reaction products behind the main wavefront and oblique shock, as well as the outward flow of reactants from the inner wall. In the downstream half of the chamber, however, turbulent mixing

homogenises the flow, leading to a more uniform thermal distribution before the exit nozzle.

Figure 6.10(d) presents a sequence of instantaneous, time-varying heat release rate ($\dot{Q}$) fields, plotted on a logarithmic scale. The chronological sequence begins at 0 μs, capturing the state immediately prior to the arrival of the detonation wave, which subsequently sweeps through the domain between 0 μs and 10 μs. The final two snapshots capture the post-wave flow dynamics, with the fourth frame intentionally extracted 40 μs after the third to illustrate the prolonged combustion effects well after the primary wave's passage. In the first snapshot, prior to the wavefront's arrival, the upper region of the cross-section already exhibits significant $\dot{Q}$. This indicates substantial commensal deflagrative combustion of residual fuel from the preceding detonation cycle. Furthermore, fresh reactants undergo "parasitic" deflagration along the contact surface where they are exposed to the high-temperature products of the previous wave. In the second snapshot, the passing of the leading wavefront is marked by an intense $\dot{Q}$ spike in the bottom-left corner. By the subsequent time-step, this high heat-release region expands to encompass half of the cross-section, with distinct reactions observable behind the oblique shock. Finally, the last snapshot demonstrates that these deflagrative reactions persist long after the primary detonation wave has swept past the region.

6.4.4 Time Evolution of Detonation Wave

To understand the unsteady nature of the RDC, it is necessary to examine the flow field's response to the periodic passage of the detonation wave, on a more macroscopic scale. Figure 6.11 presents the temporal evolution of the instantaneous temperature, pressure, and H_2 mass fraction, Y_{H_2}, which were extracted from a cylindrical section plane on the inner annular wall, across three instances, each separated by approximately 20 μs. These visualizations are flattened 3D projections from the inner wall, providing a comprehensive view of how the parameter fields fluctuate as a result of the wave's influence.

The centre row of Fig. 6.11 identifies the location of the main propagating wave. The nearly discontinuous pressure rise across the front confirms the detonation's strength. As the wave sweeps circumferentially, it acts as a transient high-pressure gate. This pressure spike correlates directly with the bottom row (Y_{H_2} mass fraction), illustrating the fuel suppression effect. The local pressure at the injector face momentarily exceeds the manifold injection pressure, resulting in a temporary pause in fuel delivery. This creates a stratified "refill zone" that is critical for determining the stability and velocity of the subsequent wave pass.

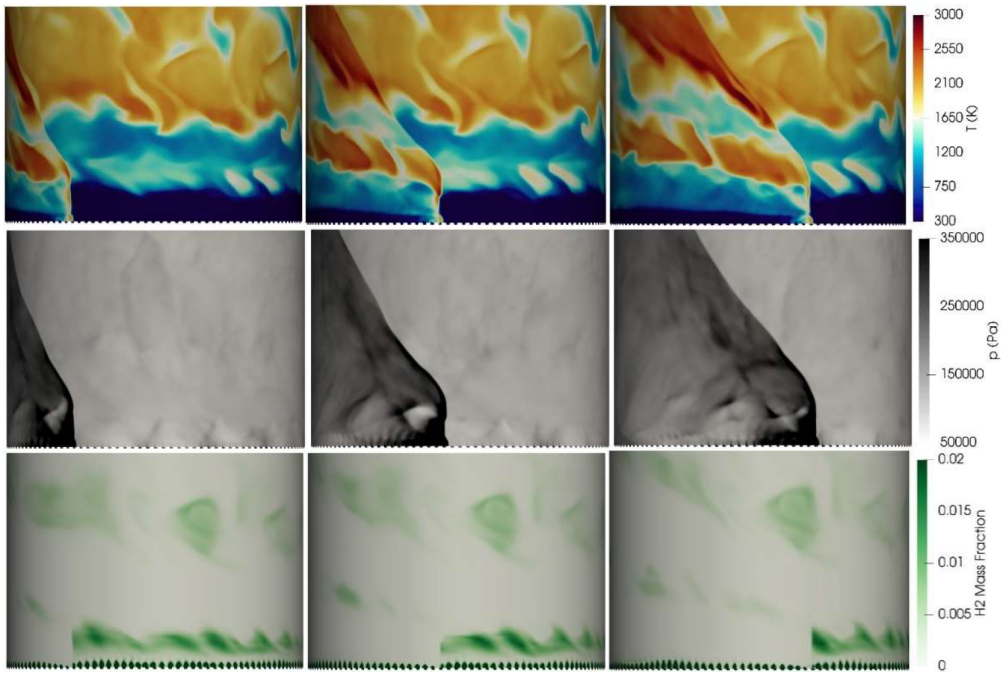

Figure 6.11: Time evolution plots, across three instances each separated by ~20 μs, of instantaneous temperature (top row), pressure (centre row), and H_2 mass fraction (bottom row), from Case 1's inner wall.

The temperature field (top row) reveals insights into the flow dynamics beyond the shock front. A distinct observation in this work is the presence of axially downstream "cold and hot strips". These striations are the result of contact surfaces formed between the fresh reactants and the combustion products from both the current and previous cycles.

As a consequence of this interaction, the local gas temperature fluctuates rapidly, often spanning a range of over 2000 K. The LES data indicates that these fluctuations are more pronounced on the inner wall than the outer wall. The peak thermal loads occur at the intersection where newly formed combustion products merge with a "hot strip" (residual products) from a previous cycle. This cyclic thermal pulsing underscores the extreme environment of the RDC and provides a quantitative basis for future thermal-structural analyses of the combustor liner.

6.5 Combustion Characterisation

A central challenge in evaluating RDC performance is distinguishing between the primary detonation reactions and deflagrative combustion, with the latter giving heat release that does not contribute to pressure gain. Furthermore, the stability of the detonative mode itself is strictly governed by the operating conditions and system scale. This section analyses the dominant combustion characteristics within the combustor.

6.5.1 Flame Index and Detonation Structure

In the context of non-premixed combustion, including within RDCs, combustion modes can vary significantly across the domain. To distinguish the local combustion characteristics, a modified Takeno Flame Index (TFI) [94] could be applied to segregate the reaction zones based on the alignment of fuel and oxidiser gradients. This theoretical diagnostic distinguishes between the various types of combustion taking place. The modified TFI is expressed as:

$$\xi_{\mathrm{M}} = \left(\frac{z - z_{\mathrm{st}}}{|z - z_{\mathrm{st}}|}\right) \cdot \frac{1}{2}\left(1 + \frac{\nabla Y_{\mathrm{F}} \cdot \nabla Y_{\mathrm{O}}}{|\nabla Y_{\mathrm{F}} \cdot \nabla Y_{\mathrm{O}}|}\right) \tag{6.1}$$

where Y_{F} and Y_{O} denote the mass fractions of fuel and oxidiser, respectively. Parallel gradients indicate premixed combustion, whereas anti-parallel gradients characterise non-premixed regions.

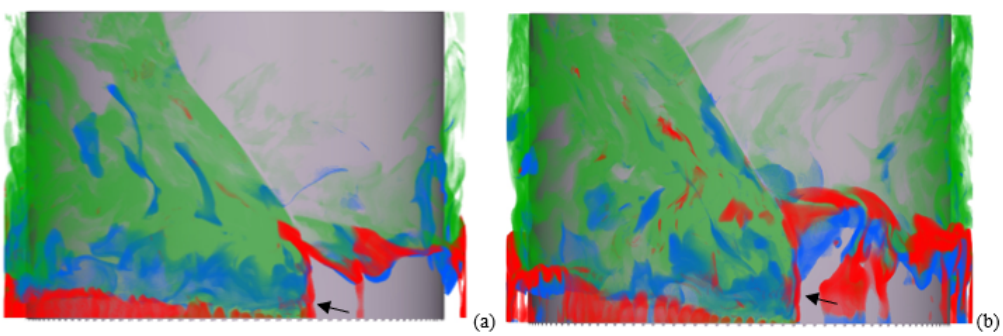

Figure 6.12: Presented in isometric view, volumetric renderings of the modified Takeno Flame Index for (a) Case A and (b) Case B. Red portions signify rich premixed, blue areas represent lean premixed, and green sections indicate non-premixed zones. Arrows mark out the positions of the detonation wave.

Figure 6.12 presents the instantaneous distribution of reaction regimes, for Cases

A1 and A2. The index distinguishes between rich premixed (red), lean premixed (blue), and non-premixed (green) burning modes.

This structural analysis affirms that the detonation front does not propagate through a homogeneous medium. Instead, the wavefront passes through two distinct premixed zones: it consumes a rich premixed layer (red) near the outer wall and a lean premixed layer (blue) near the inner wall. This confirms that the radial stratification identified in Section 6.4.3 forces the detonation to sustain itself across varying local equivalence ratios, persisting past the wavefront and into the reaction zone.

The main wave consumed most of the H_2 (or O_2) in a lean (or rich) premixed mixture, with the residual oxidiser (or fuel) reacting downstream in a non-premixed way when it mixes with the other leftover reactant. Crucially, these green zones are observed primarily in the wake of the detonation and along the contact surfaces between the fresh reactants and products. By logical deduction, these non-premixed regions likely represent deflagration, which involves diffusion flames where fuel and oxidiser burn slowly as they mix. The prevalence of these green zones in the TFI contours indicates that a significant portion of the chemical energy is released in a subsonic, non-pressure-gain mode, limiting the overall thermodynamic efficiency of the combustor.

Furthermore, the TFI visually confirms again the coexistence of two distinct combustion modes: the primary detonation wave and the parasitic deflagration occurring at the contact surfaces between fresh fuel and hot products.

6.5.2 Thermochemical Bifurcation

Having visually identified the various combustion regimes, it is necessary to examine the differing underlying chemical kinetics that drive their distinction. While the TFI provides a spatial macroscopic indicator, the fundamental difference between detonation and parasitic deflagration lies in the chemistry, specifically governed by the accumulation and consumption of intermediate radicals.

As established in the spatial radical mappings of Section 6.4.2, HO_2 acts as a critical precursor in the high-pressure ZND induction zone. While volumetric renderings (Figure 6.8) illustrate the physical geometry of these radical layers, mapping the mass fractions in a thermodynamic state-space directly correlates the species' presence with the bimodal thermodynamic behaviour of the combustor. Figure 6.13 plots the HO_2 mass fraction against local temperature, with the data points coloured by local static pressure, providing a direct chemical-kinetic

identification of the combustion modes. The resulting distribution reveals a clear bifurcation in the thermochemical state, perfectly mirroring the dual-peak phenomena seen in the heat release PDFs. The data is distinctly split into two branches.

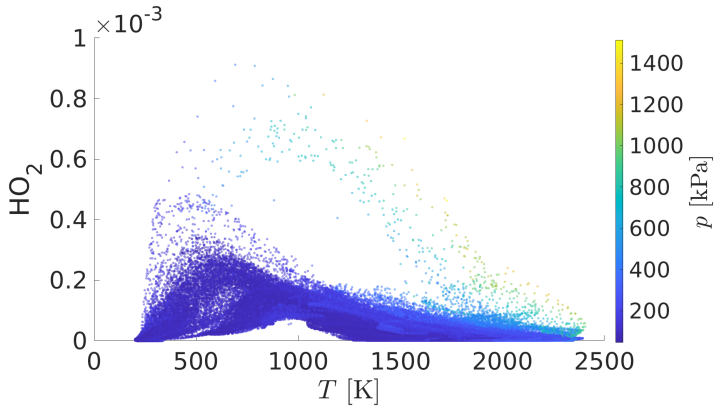

Figure 6.13: Scatter plot of HO_2 against T, coloured by p.

The upper branch corresponds to the high-pressure ZND shock compression (corresponding to the secondary peaks in Fig. 6.14(b) discussed in Section 6.5.3). Here, a sizeable accumulation of HO_2 (peaking near 0.8×10^{-3}) occurs at intermediate temperatures of roughly 1000 K to 1400 K. As established in Section 2.1.1, this non-equilibrium abundance is the direct kinetic consequence of the detonation wavefront's shock-compression accelerating third-body recombination reactions. Following this radical build-up, thermal runaway drives the temperatures towards 2500 K, causing the accumulated HO_2 to rapidly decompose into OH, visually evident as the scatter points dip sharply downwards at high temperatures.

In contrast, the lower, denser regions of the plot represent the "deflagration branch". This corresponds directly to the widespread, lower-pressure ($p \approx$ 0.5–2 bar) deflagrative burning which will be highlighted again in the next sub-section. In this diffusion-limited combustion mode, the extreme shock-compression is absent, and consequently, the mid-temperature radical accumulation of HO_2 is heavily suppressed.

The scatter plot is evidence of the LES framework's ability to properly capture the compressible finite-rate chemistry and the shock-chemistry coupling essential for detonation propagation. More importantly, it effectively closes the loop between the physical wave structure (Section 6.4.2) and the statistical heat release data (Section 6.5.3).

Furthermore, this thermochemical bifurcation serves as a highly reliable, standalone diagnostic metric. It could be used to gauge whether detonative combustion has successfully occurred within an H_2-fuelled system, distinguishing detonative combustion from instances of rapid, parasitic deflagration in complex, multi-modal environments.

The distinct separation of these thermochemical branches confirms that the flow fundamentally splits into two reaction pathways. This distinct bifurcation dictates the overarching thermodynamic performance of the combustor, the macroscopic consequences of which must be evaluated statistically.

6.5.3 Statistical Distribution of Heat Release

The clear thermochemical bifurcation of the reaction pathways explained in the previous sub-section, logically dictates that the macroscopic energy release within the combustor should also exhibit a dual nature. To quantify the thermodynamic impact of these distinct branches, conditional statistics of the heat release rate ($\dot{Q}$) were computed. Figures 6.14(a) and 6.14(b) illustrate the statistical distribution of heat release, conditioned on mixture fraction ($\langle \dot{Q} \mid z \rangle \wp(z)$) and pressure ($\langle \dot{Q} \mid p \rangle \wp(p)$), respectively, for both the low-flow single-wave (Case A1) and high-flow dual-wave (Case A2) operating cases. By scaling the conditional means by their local PDFs, $\wp$, these plots quantify the specific contribution of specific mixture states and pressure regimes to the total energy output. Physically, this implies that the area under the curve represents the global heat release rate, allowing for a direct comparison of the energy released in different regimes.

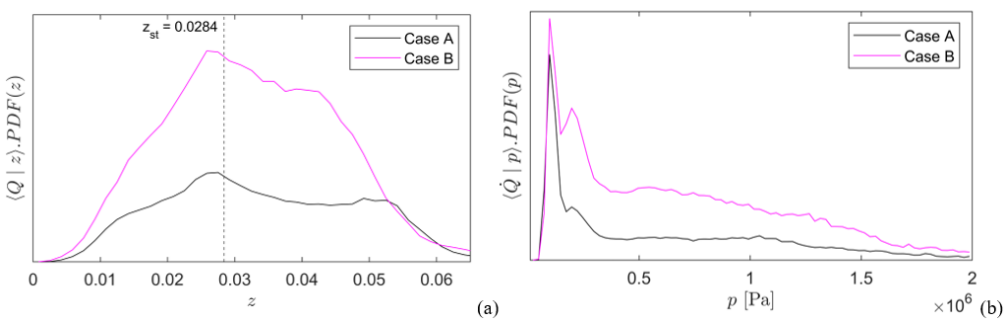

Figure 6.14: For Cases A1 and A2 (respectively labelled as "Case A" and "Case B" in plot), graph of heat release rate conditioned respectively on (a) mixture fraction, z, and scaled by probability density function, yielding $\langle \dot{Q} \mid z \rangle \wp(z)$; (b) pressure, p, and scaled by probability density function, giving $\langle \dot{Q} \mid p \rangle \wp(p)$.

As illustrated in Figure 6.14(a), the profiles for both cases exhibit similar qual-

itative trends, with maximum values occurring near the stoichiometric mixture fraction (z_{st}). Magnitudes for Case A2 (labelled as "Case B" in figure) are consistently higher than those of Case A1 (labelled as "Case A" in figure); specifically, the peak value in Case A2 is approximately two-fold that of Case A1, a result directly attributable to the doubled reactant mass flow rate.

Of more significance would be the findings of Figure 6.14(b). The PDFs reveal a distinct bimodal distribution of heat release. The first peak, located at lower pressures ($p \approx 0.5$–2 bar), corresponds directly to the lower "deflagration branch" mapped previously (Section 6.5.2), representing the widespread burning in the refill zones and contact surfaces. The second peak, occurring at high pressures ($p > 10$ bar), corresponds to the upper "detonation branch" coupled with the shock front.

Crucially, the integration of these curves indicates that a substantial fraction of the total chemical energy is released in the low-pressure (deflagrative) mode. In the dual-wave case (Case A2), although the total heat release is higher due to increased mass flow, the relative contribution of the deflagrative mode remains significant. This statistical evidence aligns with the TFI findings (Section 6.5.1), confirming that deflagrative combustion is not a minor edge effect but a dominant thermodynamic feature of the non-premixed RDC cycle.

6.6 Mass Flow Sensitivity and Wave Bi-stability

As noted in Section 6.2, a discrepancy exists at the 0.329 kg/s (total mass flow rate) operating condition between the experimental observations (one wave) and the initial LES prediction (Case A2, two co-rotating waves). To investigate this divergence and the influence of initialisation, a supplementary mass flow sensitivity study was conducted by systematically increasing the reactant flow rates.

Starting from the stable single-wave baseline at 0.144 kg/s (Case A1), the mass flow rate was sequentially increased through a series of intermediate steps. Specifically, the stabilised flow field from Case A1 was used as the initial condition for a new simulation at 0.283 kg/s (designated as Case C1). Once Case C1 reached a stable state, its flow field was subsequently mapped to initialise Case C2 at 0.306 kg/s. This sequential initialisation process was repeated for Case C3 (0.318 kg/s) and finally Case C4 (0.329 kg/s). Consequently, Case C4 operates at the exact same boundary conditions as the original Case A2, but its flow field evolved from a continuous progression rather than an abrupt numerical ignition.

For brevity, two of these mapped cases (Cases C2 and C4) have been selected for detailed analysis and comparison in the following sub-sections.

Table 6.3: Summary of key results for selected mass flow sensitivity cases, including comparisons with empirical predictions.

Case	Wave Number (N)	Wave Frequency [Hz]	Wave Height [m]	Predicted Critical Wave Height [m] [85]
Case A1	1	3060	0.0199	0.0149
Case C2	1	3239	0.0365	0.0298
Case C4	1	3119	0.0270	0.0157
Case A2	2	2990	0.0230	0.0170

Table 6.3 summarizes the LES-computed wave frequencies and heights, alongside wave number and critical height predictions derived from theoretical models. As demonstrated in the table, one theoretical model fails to correctly predict the critical heights observed in the present computational cases. On the other hand, the other more recent analytical model, which maps the kinematic boundaries of RDCs, predicts that all the studied cases fall squarely within the "all N allowed" regime. This discrepancy arises because such kinematic models likely assume idealized CJ conditions and do not account for non-ideal recovery physics, parasitic deflagration, or hysteresis. Besides the reversal of wave frequency and height trends for Case C4, another key observation is the two possible modes for the same mass flow rate as reflected by Cases C4 and B, which have the same operating conditions.

6.6.1 Influence of Ignition Dynamics and Non-Linear Bi-stability

The mathematical basis for multiple wave solutions in an RDC can be understood through the lens of non-linear dynamical systems [95]. Because the intense pressure of the detonation wave directly affects the upstream injectors (cf. Section 6.3.1), a complex feedback loop is created between the combustion chamber and the fuel supply [96, 97]. This non-linear interaction means the RDC operates in continuous periodic cycles rather than a single steady state [98], allowing multiple stable wave modes to co-exist under the exact same operating conditions [99].

Consequently, the final observed wave mode is highly path-dependent and governed by the engine's ignition history. Gradually increasing the mass flow, as seen in the sequential mapping to Case C4, allows the combustor to smoothly adapt and remain within the established stability envelope of the single-wave

mode. In contrast, an abrupt high-energy ignition at high mass flow (Case A2) creates massive transient pressure spikes and fuel disruptions. This produces a drastic shift in the system that can force the trajectory into a completely different operational state, settling into the two-wave attractor.

This mathematical bi-stability is visually confirmed in Figure 6.15, which tracks the angular positions of the detonation surfaces over time. The sequential progression from Case A1 through C2 to C4 clearly maintains a steady, single-wave trajectory, whereas the abrupt ignition of Case A2 permanently diverges into two co-rotating waves. Ultimately, while the rapid combustion provides the energy, the slower dynamics of fuel refill and exhaust shape the recovery physics and dictate this final wave pattern. Conventional empirical kinematic models often fail to predict this multiplicity because they assume idealised conditions and do not account for these non-linear feedback loops or steady-state hysteresis.

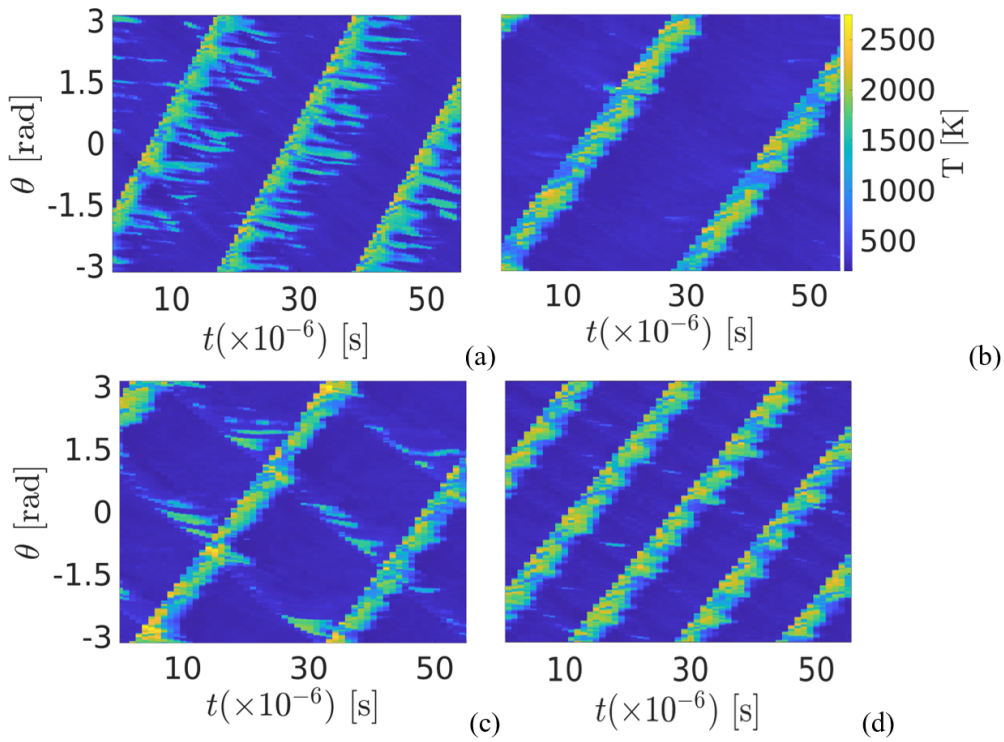

Figure 6.15: Angular positions of detonation surface(s) marked by T with time, for (a) Cases A1, (b) C2, (c) C4 and (d) A2, illustrating wave numbers, spacings and frequencies.

Further, the presence of a weaker secondary counter-rotating wave observed in the plot for Case C4 is characteristic of a single wave operating near its volu-

metric stability limit. Potentially, as the single wave becomes saturated by the elevated mass flow, it generates persistent backward-travelling acoustic reflections that lack the chemical coupling required to transition into full detonations.

6.6.2 Thermodynamic Effects: Single-Wave vs. Two-Wave Modes

Comparing the two co-existing modes at the 0.329 kg/s condition reveals distinct differences in localised heat release and efficiency, which can be evaluated using the $\langle \dot{Q} \mid p \rangle \wp(p)$ distributions introduced in Section 6.5.3. Operating in the single-wave mode (Case C4) effectively halves the contact slip-line surface area per revolution compared to the two-wave mode (Case A2). As shown in Figure 6.16(a), this significantly reduces the amount of low-pressure parasitic deflagration (portrayed as the first peak ~1 atm), occurring between fresh reactants and the hot products of the previous cycle.

However, to process the entire 0.329 kg/s mass flow with only a single wave, Case C4 requires a much larger reactant fill height. This increased height introduces curvature and outward expansion losses at the top of the wave [39], shifting a portion of the heat release from ideal high-pressure detonations to intermediate-pressure oblique shocks.

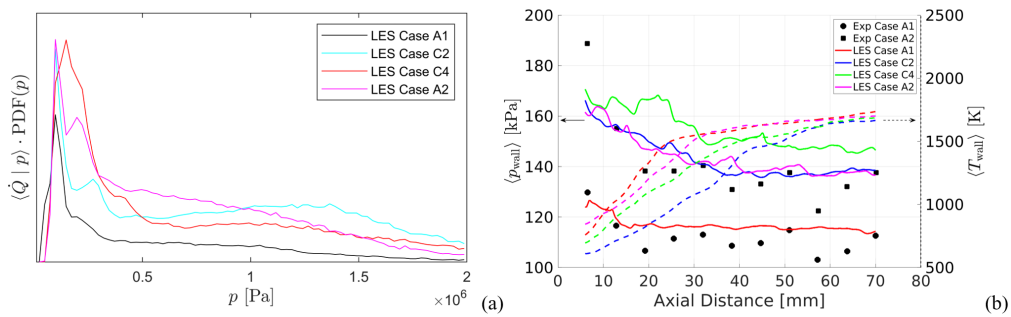

Figure 6.16: For Cases A1, C2, C4 and A2, graphs of (a) heat release rate conditioned on pressure, p, and scaled by PDF, giving $\langle \dot{Q} \mid p \rangle \wp(p)$; (b) outer wall $\langle p_{\mathrm{wall}} \rangle$ and $\langle T_{\mathrm{wall}} \rangle$ with experimental data [83].

Macroscopically, Figure 6.16(b) demonstrates that the single large-scale compression event of Case C4 yields a higher time-averaged outer-wall pressure than the split compression events of the two-wave Case A2. Interestingly, the lower time-averaged pressure of the "idealised" two-wave state more closely mirrors the experimental single-wave data. This suggests that while the idealised, adiabatic LES mathematically supports the high-efficiency two-wave state, physical experiments involve acoustic damping from plenums, wall friction, and heat

losses that naturally decrease the pressure of the single-wave mode, aligning it with the lower pressure profile captured by the LES two-wave mode.

6.7 Research in Development - Advanced Data Analysis

The immense volume and complexity of data generated by high-fidelity LES of RDCs often obscure the underlying thermodynamic phenomena when viewed through traditional Eulerian or Lagrangian lenses. To address this, a novel data-driven analytics approach is currently under development. As a highly promising proof-of-concept, an automated data-analytical technique, specifically, k-means clustering, has been applied to the simulation data. Rather than relying on arbitrary spatial boundaries or single-variable thresholds, this algorithm autonomously anatomises the highly transient flow field into distinct, multidimensional functional zones (e.g., unburnt reactants, shear mixing layers, induction zones, and the primary detonation wave) based purely on their local thermochemical states. A representative spatial mapping of these autonomously identified zones is illustrated in Figure 6.17(a).

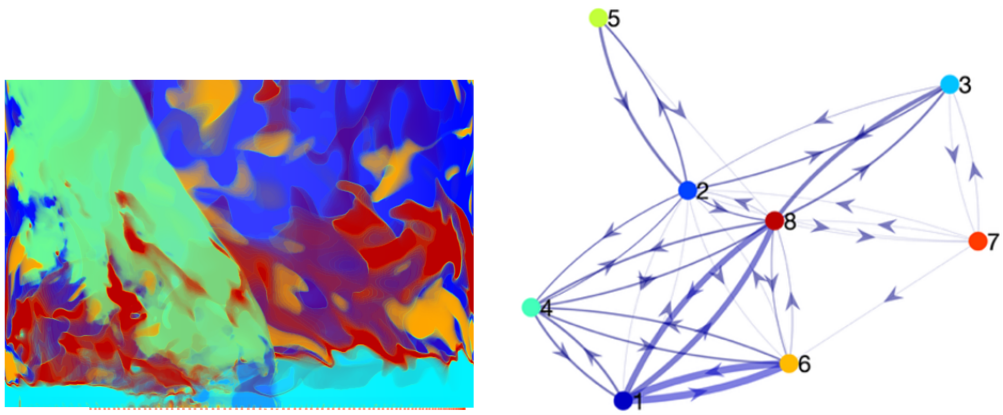

(a) (b)

Figure 6.17: Advanced data analysis sample plots. (a) Cluster distribution in the RDC physical space. (b) Sample network based on the flux of entropy between the individual clusters, with the cluster colour-coding matched to (a).

Building upon this spatial clustering, the framework further employs directed network analysis to map the thermodynamic interactions between these zones. As visualised in the network graph in Figure 6.17(b), tracking the fluxes (mass,

momentum, and entropy generation) across cluster boundaries allows for a macroscopic statistical evaluation of the combustor's operating cycle. Crucially, this topological approach lays the groundwork for defining an objective "Detonation Quality" metric. Potentially, through the quantification of the exact proportion of reactants traversing the high-efficiency detonation pathway versus lower-efficiency deflagrative or parasitic combustion routes, combustor performance could be rigorously evaluated across varying geometries and operating regimes.

While these initial demonstrations yield highly promising and physically sound insights, this advanced data analysis framework is currently being further developed into a fully robust tool. On-going effort is dedicated to fine-tuning the clustering algorithms, defining optimal state-space variables, and refining the network interaction metrics. Ultimately, the objective of maturing this analytical suite is to transition from merely observing the macroscopic flow field to systematically uncovering the crucial hidden relations that dictate wave stability, thereby deciphering the underlying physical mechanisms governing rotating detonation engines.

6.8 On-Going Work - Case Study B

The preliminary analysis of the University of Cincinnati combustor demonstrates that the baseline ILES framework successfully captures the fundamental flow dynamics of a radial-inward-air-injection RDC. As illustrated in Figure 6.18 for Case B1, the overarching wave topology (including the main detonation front, oblique shock, and contact surfaces) behaves similarly to the radial-outward-air-injection AFRL design (Case Study A).

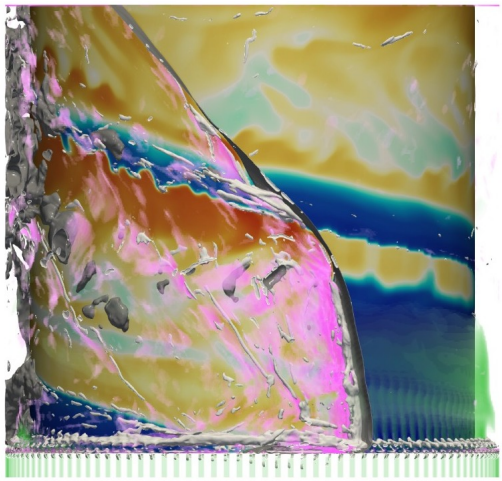

Figure 6.18: For Case B1, side view of T (warm colours) on inner wall superimposed with renderings of $\nabla \cdot \boldsymbol{v}$ (pink), p iso-surfaces (grey), λ_2 (white), and H_2 concentration (green).

However, the altered geometry and injection scheme introduce distinct hydrodynamic differences. The radial-inward air injection from the outer wall, combined with the longer axial chamber length (∼140 mm), results in a noticeably higher fuel refill height prior to detonation. Consequently, the interaction between the high-velocity crossflow jets and the expanding detonation products generates significantly more pronounced vortical structures within the reactant mixing zones compared to Case Study A.

A primary objective of simulating Case Study B was to evaluate the robustness of the LES framework's ability to predict wave phenomena, including multiplicity, across different hardware designs. To this end, an extensive simulation campaign was executed, encompassing varying mesh resolutions, initialisation strategies, and TCI model. The overarching outcomes of these runs are mapped in Figure 6.19.

The findings reveal a highly consistent agreement at lower reactivity, but a complex, branching discrepancy at higher reactivity:

1. **Low-Reactivity Agreement:** Under standard air-breathing conditions (Case B1), the numerical framework accurately and robustly predicts a stable single-wave mode ($N = 1$), matching experimental observations.

2. **High-Reactivity Discrepancy & Hysteresis:** As initially quantified in Section 5.2.3, when mixture sensitivity is increased via oxygen enrichment (Case B2), the experimental combustor reportedly transitions to a two-

wave mode ($N = 2$). The LES framework, however, exhibits a pronounced diversion dependent on the initial conditions. When ignited from scratch, the system converges to a three-wave mode ($N = 3$). Conversely, when forced to evolve from the pre-existing stable single-wave solution of Case B1, it settles into a stable single-wave mode ($N = 1$).

This branching trend in Case B2 suggests the presence of hysteresis effects within the combustor flow field for this case study's series of simulations. However, pinpointing the exact cause of the divergence from the experimental $N = 2$ state is obstructed by the inherent limitations of both numerical and experimental data sets.

A primary consideration is the stark difference in observation timescales. Practical limits to computational resources restrict the current simulation runtimes to up to roughly 4 ms of physical time (capturing between 2 to 8 wave revolutions). In contrast, the experimental hot-fire tests operate for approximately 1 second. It is highly plausible that the simulated $N = 1$ and $N = 3$ configurations are still-developing transient states. While the referenced experimental literature might lack the sub-millisecond temporal resolution required to comprehensively track these initial ignition transients, one of their related cases did record an initial two-wave transition that eventually settled into a steady one-wave mode. This experimental precedent lends significant weight to the hypothesis that the LES may be accurately capturing prolonged, quasi-stable transient modes that precede a final unrecorded mode shift.

Alternatively, similar to the findings discussed for the AFRL geometry in Case Study A, the predicted $N = 1$ and $N = 3$ modes might represent physically valid states for the Case B2 operating conditions. Given the challenging and costly nature of experimental RDC test campaigns, it is possible that these alternative states simply were not triggered or captured within the handful of available experimental runs.

To ascertain whether this multiplicity mismatch was merely a numerical artefact of the quasi-laminar assumption, further simulations incorporating the PaSR model were conducted (as detailed in Figure 6.19). Rather than simply correcting the wave count, the inclusion of the PaSR model frequently resulted in detonation extinction, denoted as 'Flame-off' here. This is an important physical lead, as this specific University of Cincinnati combustor geometry is known from experimental literature to be highly susceptible to "pop-out" (detonation failure transitioning to deflagration or extinguishment). The PaSR model's tendency to capture this flame-off behaviour suggests that, if numerically tuned appropriately, the computational model may provide critical insights into the operability

limits and transient failure modes of this specific RDC design.

Ultimately, these combined observations across two fundamentally different combustor geometries reinforce the hypothesis presented in Section 6.2. The persistent discrepancies in predicting exact wave multiplicities at higher flow and reactivity conditions suggest that the constant-mass-flow boundary conditions utilised in the current computational model omit the necessary acoustic dampening provided by the physical plenums. Investigating this coupled plenum-chamber acoustic interaction, whilst further refining the PaSR model to capture transient "pop-out" limits, forms the primary basis for the on-going and future work potentially to be pursued on Case Study B.

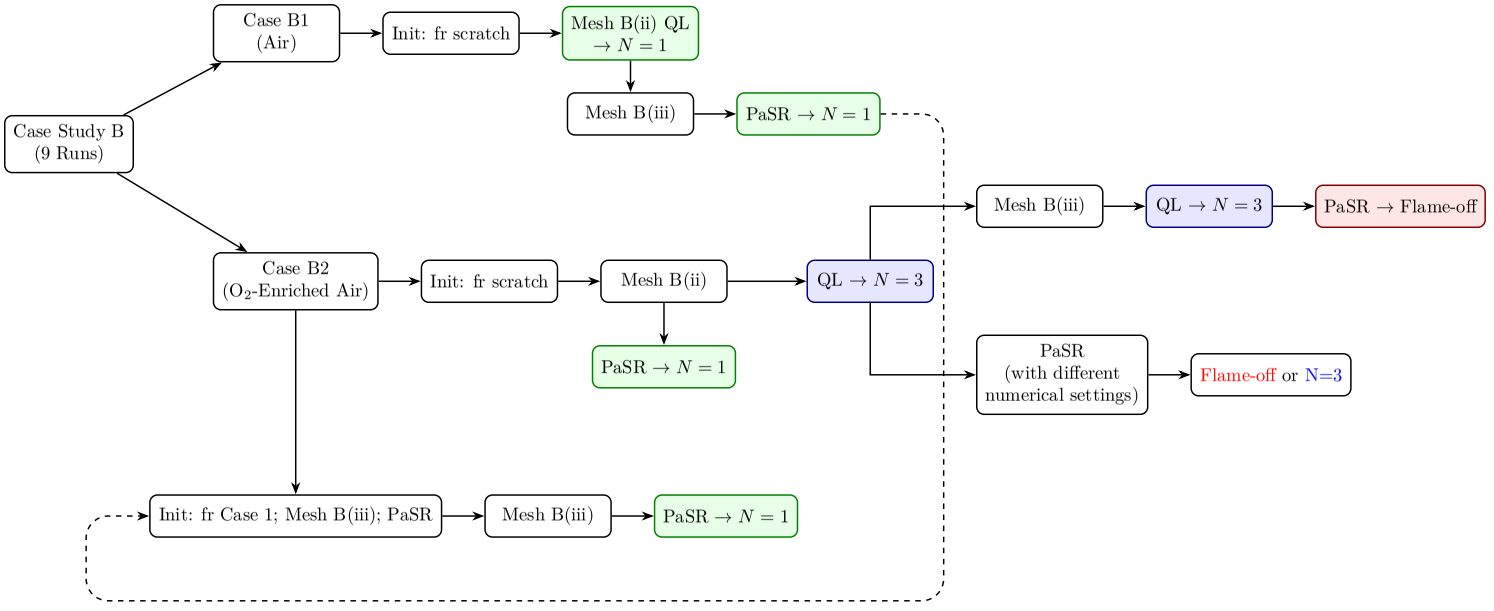

Figure 6.19: Summary map of the Case Study B simulation campaign, illustrating the outcomes across various mesh resolutions, initialisation strategies, and TCI model application.

Chapter 7

Concluding Remarks

This piece of work made use of LES to investigate rotating detonation wave characteristics. The following is a summary of key findings, as well as ideas for further research.

7.1 Summary and Conclusions

This thesis concerns the development and application of high-fidelity simulation frameworks for investigating the transient phenomena, operability limits and wave dynamics within RDCs. By simulating fundamentally different combustor geometries, the research successfully captured the complex, multi-dimensional flow topologies inherent to continuous detonation. The main conclusions drawn from the work are summarised below:

- The baseline density-based ILES framework demonstrated a robust capability to resolve the fundamental macroscopic features of RDC flow fields across distinct hardware configurations. Key flow structures, including the primary detonation front, trailing oblique shocks, slip lines and the turbulent shear mixing layers, were successfully captured.
- RDC wave multiplicity in LES was shown to be highly sensitive to operating parameters such as mass flow rate and oxygen enrichment. The numerical models predicted mode transitions and captured complex bifurcation.

- A persistent discrepancy initially observed was the over-prediction of wave multiplicity (i.e. an additional wave) under high-mass-flow or oxygen-enriched conditions when initiated via abrupt numerical ignition. However, systematic sequential mass flow mapping revealed that the RDC exhibits mathematical bi-stability. The LES framework demonstrated that multiple stable wave modes (e.g. $N = 1$ and $N = 2$) can co-exist under identical operating boundary conditions. The final operating mode is highly path-dependent and dictated by the ignition sequence and transient pressure history. While the idealised LES supports both modes, it is hypothesised that physical experiments inherently favour the lower-pressure single-wave mode due to unmodelled acoustic dampening from physical feed plenums and heat losses.

- The idealised ZND detonation pathway is significantly degraded in practical RDCs due to reactant stratification. Substantial portions of the fresh fuel-air mixture undergo parasitic deflagration rather than participating in the primary detonation wave, which drastically impacts the global thermodynamic efficiency and stability of the combustor.

- To move beyond traditional, subjective interpretations of massive RDC datasets, an automated data analytics framework was successfully implemented. The application of k-means clustering and directed network analysis autonomously anatomised the highly transient flow field into functional thermodynamic zones, laying the groundwork for an objective "Detonation Quality" metric.

7.2 Future Work

There are several interesting directions for future research based on the work presented in this thesis. Some potential areas are:

- The computational domain could be extended to incorporate physical feed plenums. Investigating the coupled interactions between the feed plenums and the main combustion chamber is anticipated to aid in resolving the multiplicity discrepancies observed at high reactivities.

- Subject to the availability of computational resources, the influence of micro-geometrical features (such as wall material properties and surface roughness) could be investigated. Given the extreme sensitivity of operational RDCs, particularly within a highly resolved LES environment,

resolving these minute physical details might prove to be a decisive factor in further enhancing simulation accuracy and correctly predicting exact wave multiplicities.

- A suitable approach for applying TCI modelling to the LES of RDCs could be further developed. The PaSR model has proven to be a promising candidate for enhancing simulation integrity. Its initial application demonstrated an accuracy improvement (in Case Study A) and valuable sensitivity to "pop-out" (detonation extinguishment) phenomena (in Case Study B), suggesting that appropriate TCI models could be utilised to accurately predict the lower operability limits and transient failure modes of specific geometries.

- A comprehensive and systematic study concerning the incorporation of detailed heat transfer effects could be performed. Preliminary results from the current research indicate that the inclusion of radiation models, for instance, might yield marginally higher predictive accuracy within the LES framework.

- The data-driven clustering and network analysis framework could be further matured. By defining optimal state-space variables and refining network interaction metrics, this analytical suite can be used to systematically uncover the hidden thermodynamic relations that govern wave stability and overall combustor efficiency.

References

[1] H. Ritchie. What share of global co2 emissions come from aviation? 2024.

[2] M. Klöwer, M. Allen, D. Lee, S. Proud, L. Gallagher, and A. Skowron. Quantifying aviation's contribution to global warming. *Environmental Research Letters*, 16:104027, 10 2021. doi: 10.1088/1748-9326/ac286e.

[3] W. H. Heiser and D. T. Pratt. Thermodynamic cycle analysis of pulse detonation engines. *Journal of Propulsion and Power*, 18(1):68–76, 2002. doi: https://doi.org/10.2514/2.5906.

[4] P. Wolański. Detonative propulsion. *Proceedings of the combustion Institute*, 34(1):125–158, 2013.

[5] K. Kailasanath and G. Patnaik. Performance estimates of pulsed detonation engines. *Proceedings of the combustion institute*, 28(1):595–601, 2000.

[6] RTX. More power, no moving parts: the quest to fly a rotating detonation engine, 2025. URL https://www.rtx.com/news/news-center/2025/03/04/rtxs-pratt-whitney-completes-series-of-rotating-detonation-engine-testing.

[7] Nagoya University. World's first successful flight of deep-space rotating detonation engine, 2021. URL https://en.nagoya-u.ac.jp/news/articles/research_information_029/.

[8] V. Anand and E. Gutmark. Rotating detonation combustors and their similarities to rocket instabilities. *Progress in Energy and Combustion Science*, 73:182–234, 2019. doi: 10.1016/j.pecs.2019.04.001.

[9] B. V. Voitsekhovskii. Stationary detonation. *Doklady Akademii Nauk SSSR*, 129(6):1254, 1959.

[10] J. Von Neuman. Theory of detonation waves. Technical report, 1942.

[11] Y. B. Zeldovich. On the theory of the propagation of detonation in gaseous systems. Technical report, 1950.

[12] W. Döring. Über den detonationsvorgang in gasen. *Annalen der Physik*, 435(6-7):421–436, 1943.

[13] Z. Liang, S. Browne, R. Deiterding, and J. Shepherd. Detonation wave propagation in unconfined regions. *Proceedings of the Combustion Institute*, 31(2):2445–2453, 2007. doi: 10.1016/j.proci.2006.08.106.

[14] C. K. Law. *Combustion Physics*. Cambridge University Press, 2006. doi: 10.1017/CBO9780511754517.

[15] A. L. Sánchez and F. A. Williams. Recent advances in understanding of flammability characteristics of hydrogen. *Progress in Energy and Combustion Science*, 41:1–55, 2014. doi: https://doi.org/10.1016/j.pecs.2013.10.002.

[16] V. G. Anand. *Rotating Detonation Combustor Mechanics*. Doctoral dissertation, University of Cincinnati, 2018. URL http://rave.ohiolink.edu/etdc/view?acc_num=ucin1530798871271548. OhioLINK Electronic Theses and Dissertations Center.

[17] W. Lin, J. Zhou, S. Liu, and Z. Lin. An experimental study on ch4/o2 continuously rotating detonation wave in a hollow combustion chamber. *Experimental Thermal and Fluid Science*, 62:122–130, 2015.

[18] H. Zhang, W. Liu, and S. Liu. Experimental investigations on h2/air rotating detonation wave in the hollow chamber with laval nozzle. *International Journal of Hydrogen Energy*, 42(5):3363–3370, 2017.

[19] X.-M. Tang, J.-P. Wang, and Y.-T. Shao. Three-dimensional numerical investigations of the rotating detonation engine with a hollow combustor. *Combustion and Flame*, 162(4):997–1008, 2015.

[20] S. Yao, X. Han, Y. Liu, and J. Wang. Numerical study of rotating detonation engine with an array of injection holes. *Shock Waves*, 27:467–476, 2017. doi: https://doi.org/10.1007/s00193-016-0690-5.

[21] J. Wilhite, R. B. Driscoll, A. C. St. George, V. Anand, and E. J. Gutmark. Investigation of a rotating detonation engine using ethylene-air mixtures. In *54th AIAA Aerospace sciences meeting*, page 1650, 2016.

[22] I. Q. Andrus, P. I. King, M. D. Polanka, F. R. Schauer, and J. L. Hoke. Design of a premixed fuel–oxidizer system to arrest flashback in a rotating detonation engine. *Journal of Propulsion and Power*, 33(5):1063–1073, 2017.

[23] D. E. Paxson. Preliminary computational assessment of disk rotating detonation engine configurations. Technical Report NASA/TM-2020-220455, NASA Glenn Research Center, 2020. URL https://ntrs.nasa.gov/citations/20200000231.

[24] Z. Xia, H. Ma, Y. He, G. Ge, and C. Zhou. Visual experimental research on the propagation instabilities in a plane-radial rotating detonation engine. *Aerospace Science and Technology*, 122:107335, 2022.

[25] V. Raman, S. Prakash, and M. Gamba. Nonidealities in rotating detonation engines. *Annual Review of Fluid Mechanics*, 55, 2023. doi: https://doi.org/10.1146/annurev-fluid-030222-014523.

[26] P. Strempfl, O. Dounia, D. Laera, and T. Poinsot. Effects of mixing assumptions and models for les of hydrogen-fueled rotating detonation engines. *International Journal of Hydrogen Energy*, 62:1–16, 2024. doi: https://doi.org/10.1016/j.ijhydene.2024.03.024.

[27] S. Frolov, V. Zvegintsev, V. Ivanov, V. Aksenov, I. Shamshin, D. Vnuchkov, D. Nalivaichenko, A. Berlin, and V. Fomin. Demonstrator of continuous-detonation air-breathing ramjet: Wind tunnel data. *Doklady Physical Chemistry*, pages 75–79, 2017. doi: https://doi.org/10.1134/S0012501617050001X.

[28] D. Stechmann, D. Lim, and S. Heister. Experimental study of a high pressure rotating detonation wave combustor for rocket applications. In *European Conference for Aerospace Sciences*, 2015.

[29] S. Jin, L. Qi, N. Zhao, H. Zheng, Q. Meng, and J. Yang. Experimental and numerical research on rotating detonation combustor under non-premixed conditions. *International Journal of Hydrogen Energy*, 45(16):10176–10188, 2020. doi: https://doi.org/10.1016/j.ijhydene.2020.01.214.

[30] J. Kindracki, P. Wolański, and Z. Gut. Experimental research on the rotating detonation in gaseous fuels–oxygen mixtures. *Shock Waves*, 21:75–84, 2011. doi: https://doi.org/10.1007/s00193-011-0306-z.

[31] S.-J. Liu, Z.-Y. Lin, W.-D. Liu, W. Lin, and M.-B. Sun. Experimental and three-dimensional numerical investigations on h2/air continuous rotating

detonation wave. *Proceedings of the Institution of Mechanical Engineers, Part G: Journal of Aerospace Engineering*, 227(2):326–341, 2013. doi: ht tps://doi.org/10.1177/0954410011431618.

[32] T. Kayser, H. Wei, E. Bach, C. O. Paschereit, and M. Bohon. Experimental comparison of different pressure gain measurement techniques for rdcs. In *AIAA Scitech 2023 Forum*, page 0929, 2023.

[33] M. L. Fotia, F. Schauer, T. Kaemming, and J. Hoke. Experimental study of the performance of a rotating detonation engine with nozzle. *Journal of Propulsion and Power*, 32(3):674–681, 2016.

[34] D. E. Paxson and J. L. Hoke. Time averaged pressure measurement in fundamentally unsteady pressure gain combustion systems. In *45th Combustion/33rd Airbreathing Propulsion/33rd Exhaust Plume and Signatures/27th Propulsion Hazards Joint Subcommittee Meeting*, number E-20044, 2013.

[35] K. Y. Cho, J. R. Codoni, B. A. Rankin, J. Hoke, and F. Schauer. High-repetition-rate chemiluminescence imaging of a rotating detonation engine. In *54th AIAA aerospace sciences meeting*, page 1648, 2016.

[36] J. Tobias, A. K. Agrawal, and D. E. Paxson. Experimental and computational analysis of a rotating detonation combustor. In *AIAA SCITECH 2022 Forum*, number AIAA 2022-1879, San Diego, CA, January 2022. American Institute of Aeronautics and Astronautics. doi: 10.2514/6.20 22-1879. URL https://arc.aiaa.org/doi/10.2514/6.2022-1879.

[37] V. Anand, A. S. George, R. Driscoll, and E. Gutmark. Longitudinal pulsed detonation instability in a rotating detonation combustor. *Experimental Thermal and Fluid Science*, 77:212–225, 2016.

[38] S. Subramanian. Novel approach for computational modeling of a non-premixed rotating detonation engine. Master's thesis, Virginia Tech, 2019. URL http://hdl.handle.net/10919/101777. SciSpace PDF: https://scispa ce.com/pdf/novel-approach-for-computational-modeling-of-a-non-premi xed-40cq5smsve.pdf.

[39] D. Schwer and K. Kailasanath. Numerical investigation of the physics of rotating-detonation-engines. *Proceedings of the Combustion Institute*, 33 (2):2195–2202, 2011. doi: https://doi.org/10.1016/j.proci.2010.07.050.

[40] S. Ye-Tao and W. Jian-Ping. Three dimensional simulation of rotating detonation engine without inner wall. In *23rd ICDERS*, pages 24–29, 2011.

[41] H. Peng and R. Deiterding. High-resolution numerical simulation of rotating detonation waves with parallel adaptive mesh refinement. *Applications in Energy and Combustion Science*, 21:100316, 2025. doi: https://doi.org/10.1016/j.jaecs.2025.100316.

[42] D. E. Paxson. Numerical analysis of a rotating detonation engine in the relative reference frame. In *52nd Aerospace Sciences Meeting*, page 0284, 2014. doi: https://doi.org/10.2514/6.2014-0284.

[43] S. Frolov, A. Dubrovskii, and V. Ivanov. Three-dimensional numerical simulation of operation process in rotating detonation engine. *Progress in Propulsion Physics*, 4:467–488, 2013. doi: https://doi.org/10.1051/eucass/201304467.

[44] S. Prakash, V. Raman, C. F. Lietz, W. A. Hargus Jr, and S. A. Schumaker. Numerical simulation of a methane-oxygen rotating detonation rocket engine. *Proceedings of the Combustion Institute*, 38(3):3777–3786, 2021.

[45] S. Yellapantula, V. Tangirala, K. Singh, and J. Haynes. A numerical study of h2-air rotating detonation combustor. In *26th Int. Colloquium on the Dynamics of Explosion and Reactive Systems*, 2017.

[46] J. Smagorinsky. General circulation experiments with the primitive equations: I. the basic experiment. *Monthly weather review*, 91(3):99–164, 1963.

[47] F. Nicoud and F. Ducros. Subgrid-scale stress modelling based on the square of the velocity gradient tensor. *Flow, turbulence and Combustion*, 62(3):183–200, 1999.

[48] M. Salvadori, P. Tudisco, D. Ranjan, and S. Menon. Numerical investigation of mass flow rate effects on multiplicity of detonation waves within a h2/air rotating detonation combustor. *International journal of hydrogen energy*, 47(6):4155–4170, 2022.

[49] Y. Lim, T. Nilsson, and C. Fureby. Large eddy simulations of rotating detonations in non-premixed h2-air annular combustor. *Combustion Science and Technology*, pages 1–24, 2025.

[50] M. Zhao and H. Zhang. Large eddy simulation of non-reacting flow and mixing fields in a rotating detonation engine. *Fuel*, 280:118534, 2020. doi: https://doi.org/10.1016/j.fuel.2020.118534.

[51] S. B. Pope. Ten questions concerning the large-eddy simulation of turbulent flows. *New journal of Physics*, 6(1):35–35, 2004.

[52] T. Gaillard, D. Davidenko, and F. Dupoirieux. Numerical analysis of a continuously rotating detonation engine operation with hydrogen-air mixture. *Acta Astronautica*, 141:64–78, 2017. doi: 10.1016/j.actaastro.2017.09.027.

[53] S. Menon and C. Fureby. Computational combustion. In *Encyclopedia of Aerospace Engineering*. Wiley, 2010. doi: https://doi.org/10.1002/9780470686652.eae058.

[54] T. Nilsson, S. Zhong, and C. Fureby. Les of h2-air jet combustion in high enthalpy supersonic crossflow. *Physics of Fluids*, 33(3):035133, 2021. doi: https://doi.org/10.1063/5.0044558.

[55] H. Versteeg and W. Malalasekera. *An Introduction to Computational Fluid Dynamics e-book*. Pearson Education, 2007. ISBN 9781405891042. URL https://books.google.se/books?id=NbYmEAAAQBAJ.

[56] W.-W. Kim and S. Menon. A new dynamic one-equation subgrid-scale model for large eddy simulations. In *33rd aerospace sciences meeting and exhibit*, page 356, 1995.

[57] C. Fureby, N. Alin, N. Wikström, S. Menon, N. Svanstedt, and L. Persson. Large-eddy simulation of flow and heat transfer in a square duct. *AIAA Journal*, 42(3):457–468, 2004. doi: 10.2514/1.1706.

[58] D. B. Spalding. A single formula for the "law of the wall". *Journal of Applied Mechanics*, 28(3):455–458, 1961. doi: 10.1115/1.3641728.

[59] H. G. Weller, G. Tabor, H. Jasak, and C. Fureby. A tensorial approach to computational continuum mechanics using object-oriented techniques. *Computers in Physics*, 12(6):620–631, 1998. doi: https://doi.org/10.1063/1.168744.

[60] E. Giacomazzi, F. Picchia, and N. Arcidiacono. On the distribution of lewis and schmidt numbers in turbulent flames. In *30th Italian Meeting on Combustion, Ischia, Italy*, 2007.

[61] E. Giacomazzi, F. Picchia, and N. Arcidiacono. A review on the perfectly stirred reactor theory. In *30th Italian Meeting on Combustion*, Ischia, Italy, 2007. Citeseer.

[62] A. Kurganov and E. Tadmor. New high-resolution central schemes for nonlinear conservation laws and convection–diffusion equations. *Journal of Computational Physics*, 160(1):241–282, 2000. doi: 10.1006/jcph.2000.6459.

[63] A. Kurganov, S. Noelle, and G. Petrova. Semidiscrete central-upwind schemes for hyperbolic conservation laws and hamilton–jacobi equations. *SIAM Journal on Scientific Computing*, 23(3):707–740, 2001. doi: 10.1137/S1064827500373 41X.

[64] G. Strang. On the construction and comparison of difference schemes. *SIAM Journal on Numerical Analysis*, 5(3):506–517, 1968. doi: 10.1137/0705041.

[65] E. Hairer and G. Wanner. *Solving Ordinary Differential Equations II: Stiff and Differential-Algebraic Problems*. Springer, 1991. doi: 10.1007/978-3-642-05221-7.

[66] N. Marinov, C. Westbrook, and W. Pitz. Detailed and global chemical kinetics model for hydrogen. In *Transport Phenomena in Combustion*, volume 1, page 118. Taylor & Francis, 1996.

[67] D. Eklund and S. Stouffer. A numerical and experimental study of a supersonic combustor employing swept ramp fuel injectors. In *30th Joint Propulsion Conference and Exhibit*, page 2819, 1994. doi: 10.2514/6.1994-2819.

[68] R. Baurle and S. Girimaji. Assumed pdf turbulence-chemistry closure with temperature-composition correlations. *Combustion and Flame*, 134(1-2): 131–148, 2003. doi: https://doi.org/10.1016/S0010-2180(03)00088-3.

[69] D. Davidenko, I. Gökalp, E. Dufour, and P. Magre. Numerical simulation of hydrogen supersonic combustion and validation of computational approach. In *12th AIAA International Space Planes and Hypersonic Systems and Technologies Conference*, page 7033, 2003. doi: 10.2514/6.2003-7033.

[70] C. J. Jachimowski. An analytical study of the hydrogen-air reaction mechanism with application to scramjet combustion. Technical Report NASA-TP-2791, NASA Langley Research Center, 1988.

[71] V. A. Alekseev, M. Christensen, and A. A. Konnov. The effect of temperature on the adiabatic burning velocities of diluted hydrogen flames: A kinetic study and literature review. *Combustion and Flame*, 162(5):1884–1898, 2015. doi: 10.1016/j.combustflame.2014.12.009.

[72] H. Wang, X. You, A. V. Joshi, S. G. Davis, A. Laskin, F. Egolfopoulos, and C. K. Law. Usc mech version ii. high-temperature combustion reaction model of h2/co/c1-c4 compounds. http://ignis.usc.edu/USC_Mech_II.htm, 2007.

[73] N. Zettervall and C. Fureby. A computational study of ramjet, scramjet and dual-mode ramjet combustion in combustor with a cavity flameholder. In *2018 AIAA Aerospace Sciences Meeting*, page 1146, 2018. doi: https://doi.org/10.2514/6.2018-1146.

[74] W. Breitung, C. Chan, S. Dorofeev, A. Eder, B. Gelfand, M. Heitsch, R. Klein, A. Malliakos, E. Shepherd, and E. Studer. Flame acceleration and deflagration-to-detonation transition in nuclear safety. Technical report, NEA/CSNI, 2000.

[75] D. R. Dowdy, D. B. Smith, S. C. Taylor, and A. Williams. The use of expanding spherical flames to determine burning velocities and stretch effects in hydrogen/air mixtures. *Symposium (International) on Combustion*, 23 (1):325–332, 1991. doi: https://doi.org/10.1016/S0082-0784(06)80276-8.

[76] M. Juniper, N. Darabiha, and S. Candel. The extinction limits of a hydrogen counterflow diffusion flame above liquid oxygen. *Combustion and Flame*, 135(1-2):87–96, 2003. doi: https://doi.org/10.1016/S0010-2180(03)00155-4.

[77] O. Kwon and G. Faeth. Flame/stretch interactions of premixed hydrogen-fueled flames: Measurements and predictions. *Combustion and Flame*, 124 (4):590–610, 2001. doi: https://doi.org/10.1016/S0010-2180(00)00227-8.

[78] S. Samuelsen, V. McDonell, M. Greene, and D. Beerer. Correlation of ignition delay with natural gas and igcc type fuels. Technical report, Univ. of California, Irvine, 2006.

[79] M. Slack and A. Grillo. Investigation of hydrogen-air ignition sensitized by nitric oxide and by nitrogen dioxide. final report. Technical report, Grumman Aerospace Corp., Bethpage, NY (USA), 1977.

[80] A. Snyder, G. Skinner, J. Robertson, and D. Zanders. Shock tube studies of fuel-air ignition characteristics. Technical report, Monsanto Research Corp Dayton OH, 1965.

[81] P. Strempfl, O. Dounia, D. Laera, and T. Poinsot. Effects of mixing assumptions and models for les of hydrogen-fueled rotating detonation engines. *International Journal of Hydrogen Energy*, 62:1–16, 2024. doi: 10.1016/j.ijhydene.2024.03.033.

[82] B. A. Rankin, D. R. Richardson, A. W. Caswell, A. G. Naples, J. L. Hoke, and F. R. Schauer. Operating characteristics of a continuous rotating detonation engine continuous exhaust flowfield. *Combustion and Flame*, 176: 12–22, 2017. doi: 10.1016/j.combustflame.2016.09.022.

[83] B. A. Rankin, D. R. Richardson, A. W. Caswell, A. G. Naples, J. L. Hoke, and F. R. Schauer. Chemiluminescence imaging of an optically accessible non-premixed rotating detonation engine. *Combustion and Flame*, 176: 12–22, 2017. doi: https://doi.org/10.1016/j.combustflame.2016.09.027.

[84] A. Feleo, J. Shepard, and M. Gamba. Experimental study of the invariance of pressure gain with respect to the dynamics of multiple competing waves in a rotating detonation combustor. In *AIAA SCITECH 2023 Forum*, page 1296, 2023. doi: https://doi.org/10.2514/6.2023-1296.

[85] A. S. George, R. Driscoll, V. Anand, and E. Gutmark. On the existence and multiplicity of rotating detonations. *Proceedings of the Combustion Institute*, 36(2):2691–2698, 2017.

[86] V. Anand, A. S. George, R. Driscoll, and E. Gutmark. Characterization of instabilities in a rotating detonation combustor. *International Journal of Hydrogen Energy*, 40(46):16649–16659, 2015.

[87] V. Anand, A. S. George, and E. Gutmark. Amplitude modulated instability in reactants plenum of a rotating detonation combustor. *International Journal of Hydrogen Energy*, 42(17):12629–12644, 2017.

[88] A. Åkerblom. *Large Eddy Simulations of Alternative Jet Fuel Combustion.* Doctoral dissertation, University of Cincinnati, 2018.

[89] C. Fureby, D. M. Peterson, T. Ombrello, and D. Eklund. Les of supersonic combustion in a mach 2 cavity-based model scramjet combustor with conjugate heat transfer and radiative heat transfer. In *AIAA SCITECH 2025 Forum*, page 0391, 2025. doi: https://doi.org/10.2514/6.2025-0391.

[90] V. Sabelnikov and C. Fureby. On the flame surface density and the presumed pdf modeling of premixed turbulent flames. *Combustion and Flame*, 160(1):83–96, 2013. doi: 10.1016/j.combustflame.2012.09.006.

[91] V. Raman, S. Prakash, and M. Gamba. Modeling and simulation of rotating detonation engines. *Annual Review of Fluid Mechanics*, 55:55–82, 2023. doi: 10.1146/annurev-fluid-120720-013143.

[92] G. Vignat, D. Brouzet, M. Bonanni, and M. Ihme. Analysis of weak secondary waves in a rotating detonation engine using large-eddy simulation and wavenumber-domain filtering. *Combustion and Flame*, 263:113387, 2024. doi: https://doi.org/10.1016/j.combustflame.2024.113387.

[93] J. E. Shepherd. Detonation waves and propulsion. In *Combustion in high-speed flows*, pages 373–420. Springer, 1994.

[94] A. J. Lock, A. M. Briones, X. Qin, S. K. Aggarwal, I. K. Puri, and U. Hegde. Liftoff characteristics of partially premixed flames produced by realistic burner configurations. *Combustion and Flame*, 143(1-2):159–173, 2005. doi: 10.1016/j.combustflame.2005.05.011.

[95] S. Snijders, X. Mi, C. Renshaw-Whitman, A. J. Higgins, and C. B. Kiyanda. A model for multi-wave dynamics in a rotating detonation engine. In *Proceedings of the 30th International Colloquium on Dynamics of Explosions and Reactive Systems (ICDERS)*, number 197, 2025. URL https://icders.com/res/ICDERS2025-197.pdf.

[96] J. Koch, M. Kurosaka, C. Knowlen, and J. N. Kutz. Multiscale physics of rotating detonation waves: Autosolitons and modulational instabilities. *Physical Review E*, 104(2):024210, 2021.

[97] D. E. Paxson. Examination of wave speed in rotating detonation engines using simplified computational fluid dynamics. In *2018 AIAA Aerospace Sciences Meeting*, page 1883, 2018.

[98] F. A. Bykovskii, S. A. Zhdan, and E. F. Vedernikov. Continuous spin detonations. *Journal of propulsion and power*, 22(6):1204–1216, 2006.

[99] E. W. Plaehn, I. V. Walters, R. M. Gejji, and C. D. Slabaugh. Bifurcation in rotating detonation engine operation with continuously variable fuel injection location. *Journal of Propulsion and Power*, 39(2):202–216, 2023.

Scientific publications

Author contributions

Co-authors are abbreviated as follows:
Yuxiang Lim (YL), Thommie Nilsson (TN), Christer Fureby (CF).

Paper I: Three-Dimensional Large-Eddy Simulation of Non-Premixed H2-Air Annular Rotating Detonation Combustor

Y. Lim, T. Nilsson, C. Fureby

This research utilises three-dimensional Large Eddy Simulations (LES) to investigate a non-premixed hydrogen-air annular rotating detonation combustor (RDC). Marking the first application of a specialised in-house solver, the study establishes a systematic methodology for executing high-fidelity RDC simulations. Following rigorous validation against experimental data, the time evolution of detonation waves is analysed to explore their coupling with instantaneous flow fields. The findings align well with established experimental observations whilst contributing novel insights into wave number bifurcation and flow stratification.

The candidate (YL) set up and carried out the simulations, conducted the data post-processing, generated the figures, analysed the results, and wrote the manuscript. CF did a portion of the writing for on the numerics. TN and CF provided supervision and technical guidance throughout the simulation runs, manuscript preparation, and revision.

Paper ii: Investigation of Detonation Wave Phenomena in Non-Premixed H2-Air Annular Rotating Detonation Combustor using Large-Eddy Simulation

Y. Lim, T. Nilsson, C. Fureby

Building upon the computational model established previously, this study fo-

cuses on more in-depth and statistical analyses of the flow dynamics within a non-premixed hydrogen-air RDC. While the previous work focused on model validation, this project utilises high-fidelity LES to investigate the complex coupling between reactant mixing, detonation wave structure, and parasitic combustion modes.

The candidate (YL) set up and carried out the simulations, conducted the data post-processing, generated the figures, analysed the results, and wrote the manuscript. TN provided technical advice on part of the statistical data-processing. TN and CF provided supervision and technical guidance throughout the simulation runs, manuscript preparation, and revision.

Paper iii: Large Eddy Simulations of Rotating Detonations in Non-Premixed H2-Air Annular Combustor

Y. Lim, T. Nilsson, C. Fureby

Building on Paper I, this paper documents our complete, high-fidelity LES methodology for RDCs, newly enhanced with a wall model for near-wall flows. The study fundamentally compares flow patterns and wave behaviors between two different mass flow rates. To address experimental discrepancies at the higher flow rate, we also include a numerical sensitivity study analysing how key parameters influence predicted wave counts, combustion stability, and overall RDC performance.

The candidate (YL) set up and carried out the simulations, conducted the data post-processing, generated the figures, analysed the results, and wrote the manuscript. CF did a portion of the writing for model sensitivity discussion. TN and CF provided supervision and technical guidance throughout the simulation runs, manuscript preparation, and revision.

Paper iv: Investigating Detonation Wave Characteristics in Non-Premixed Hydrogen-Air Annular Rotating Detonation Combustor using Large-Eddy Simulations

Y. Lim, T. Nilsson, C. Fureby

This study expands the analysis of RDC flow physics using a high-fidelity LES solver with detailed chemistry and subgrid wall-modelling. It evaluates instantaneous and time-averaged radial flow variations, alongside a detailed examination of injector dynamics and axial statistical parameters across two operating cases. A primary focus is assessing how varying mass flow rates impact wave number and dynamics, combustion characteristics, and heat release rates. Ultimately, this comparison elucidates the critical competition between detonation and parasitic deflagration, providing key insights to optimise RDC performance

for space propulsion.

The candidate (YL) set up and carried out the simulations, conducted the data post-processing, generated the figures, analysed the results, and wrote the manuscript. CF provided technical suggestions on part of the data evaluation. CF provided conceptualisation and technical facilitation of some of the studies, as well as part of the writing. TN and CF provided supervision and technical guidance throughout the simulation runs, manuscript preparation, and revision.

Paper v: Large Eddy Simulations and Data Analytics of Rotating Detonation Combustion

Y. Lim, T. Nilsson, C. Fureby

This project conducts a systematic sensitivity study to quantify how key modelling components—namely wall heat transfer, thermal radiation, and turbulence-chemistry interactions—impact established RDC simulations. A significant novel contribution is the application of data-driven methodologies, such as clustering and network analysis, to deconstruct high-dimensional LES datasets. Moving beyond conventional time-averaging, this approach partitions the flow field into distinct functional zones. By mapping the entropy flux between these clusters, the study facilitates a clearer visualisation of mass, momentum, and energy transfer pathways.

The candidate (YL) set up and carried out the simulations, conceptualised and conducted the bulk of the data post-processing, generated the main figures, analysed the results, and wrote the manuscript. CF contributed to the idea conceptualisation and data-processing. TN and CF provided supervision and technical guidance throughout the simulation runs, manuscript writing, and revision.

Printed by Media-Tryck, Lund 2026 NORDIC SWAN ECOLABEL 3041 0903

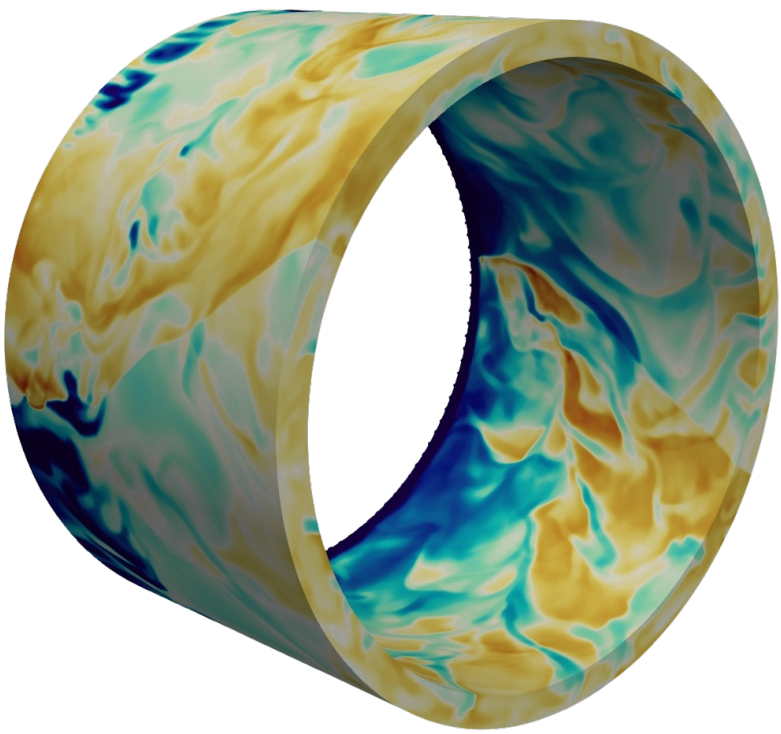

Division of Heat Transfer
Department of Energy Sciences
Faculty of Engineering

ISBN 978-91-8104-997-8
ISSN 0282-1990
ISRN LUTMDN/TMHP-26/1186-SE

LUND UNIVERSITY